https://doi.org/10.15407/ufm.23.02.147

A.G. SOLOMENKO [1,*], R.M. BALABAI [2,], T.M. RADCHENKO [1,***], and V.A. TATARENKO [1,****]**

[1] G.V. Kurdyumov Institute for Metal Physics of the N.A.S. of Ukraine, 36 Acad. Vernadsky Blvd., UA-03142 Kyiv, Ukraine

[2] Kryvyi Rih State Pedagogical University, 54 Gagarina Ave., UA-50086 Kryvyi Rih, Ukraine

*sola@imp.kiev.ua, ** balabai@i.ua, *** tarad@imp.kiev.ua, **** tatar@imp.kiev.ua

FUNCTIONALIZATION OF QUASI-TWO-DIMENSIONAL MATERIALS: CHEMICAL AND STRAIN-INDUCED MODIFICATIONS

Among the family of currently known promising quasi-two-dimensional (2*D*) materials, the authors of this survey concentrate on the problem of functionalization of the graphene- and phosphorene-based structures. In most cases, the modification of their properties occurs through the covalent or noncovalent surface functionalization and mechanical affects. The atomic structures and some physicochemical features of 2*D* materials possessing novel properties as compared to their bulk counterparts are analysed. Their main advantages are the thickness of one or more atoms, the absence of surface-broken bonds, high mobility of charge carriers, the flexibility, the ability to be combined artificially into coplanar (lateral) or lamellar heterostructures, as well as the possibility to manipulate widely the band-gap changing from the semi-conducting state even into the semi-metallic one (or *vice versa*) when needed. In order to reveal new factors affecting the electronic properties of 2*D* materials by means of the computational experiment using the author's (self-constructed) software code, a series of studies are carried out. They are the calculations of the spatial distribution of valence electrons' density, the electron densities of states, the band-gap widths, Coulomb potentials along selected directions, the charge values in regions of different-size material, the dielectric matrices, the macroscopic relative permittivities, and absorption spectra. A series of recent studies, which the authors carried out modelling the electronic and transport properties of single- or multilayer graphene films subjected to deformation or/and magnetic fields and containing different-type (point- or/and linear-acting) defects is reviewed. Analysing the obtained results and revealed effects, it is claimed that the uniaxial tensile defor-

Citation: A.G. Solomenko, R.M. Balabai, T.M. Radchenko, and V.A. Tatarenko, Functionalization of Quasi-Two-Dimensional Materials: Chemical and Strain-Induced Modifications, *Progress in Physics of Metals*, **23**, No. 2: 147–238 (2022)

mations or shear deformations along with their combinations as well as the structural imperfections (mainly, the mutually configured defects) can be useful for achieving the new level of functionalization of graphene. So, for modification of its electrotransport properties through tuning the band-gap value as much as it is enough to achieve the graphene transformation from the zero-band-gap semi-metallic state into the semi-conducting state and even reach the gap values, which are substantially higher than that for some materials (including silicon) currently used widely in the nanoelectronic devices. The strain- and defect-induced electron–hole asymmetry and anisotropy of conductivity and its nonmonotony as a function of deformation suggest a confidence in manipulating the electrotransport properties of graphene-like and beyond quasi-2*D* materials through a variety of both strains and defects. The use of reviewed and analysed results serves as a significant step in improving the properties of the considered materials in order to implement the multifunctional applications of them in the immediate prospect.

Keywords: two-dimensional materials, point and linear defects, graphene, phosphorene, electronic structure, electronic transport, density functional theory, pseudo-potential from the first principles, straintronics, band gap.

1. Introduction

As known [1, 2], one of the classifications of (nano)materials relates to the number of dimensions of a material, which are outside the nanoscale ($\lesssim$100 nm) range.

For zero-dimensional (0*D*) nanomaterials, all the dimensions are measured within the nanoscale, *i.e.*, no dimension is larger than 100 nm. Most commonly, this class consists of nanoparticles, quantum dots, polymer dots, and fullerenes [3].

For one-dimensional (1*D*) nanomaterials, one dimension is outside the nanoscale range. This class includes nanotubes, nanorods, and quantum and nanowires [3].

For two-dimensional (2*D*) nanomaterials, two dimensions are outside the nanoscale range, and along one dimension, there are stacked only a single-atom-thick or a few-atoms-thick layers. This class exhibits quantum wells, graphenelike and other monolayer materials such as MXenes, phosphorene, silicene, germanene, arsenene, hexagonal boron nitride and others [3]. Besides, there are quasi-two-dimensional nanomaterials such as graphene films, nanosheets and other related systems.

Finally, three-dimensional (3*D*) (nano)materials (as well as (nano) systems or (nano)structures) as a whole are not confined to the nanoscale range in any dimension. Nevertheless, this class can contain: nanocrystalline materials; bulk nanopowders; nanoporous materials; dispersions (colloids) of nanoparticles; intercalation compounds; bundles of nanowires and nanotubes as well as multinanolayers; nanoscale contacts; (nano)composites (nanosystems embedded in a larger structure),

e.g., diamond/nanocarbon composites; complex nanostructures, including patterned or assembled structures, nanoaggregates, nanodroplets, nanomicelles [3].

The object of research in this article are (quasi-)2*D* materials, which in turn can be classified according to their composition or/and structure as homo- and heteroelemental, single- and a-few-layers systems with overall layer(s) thickness of just a few nanometres [4, 5]. The subject of research focuses on the analysis of several factors appropriate for affecting the electronic and electrotransport properties of some representatives of family of the (quasi-)2*D* materials. Such materials have been a central topic of research since graphene discovery at the beginning of this century [6] due to their ultrathin thickness and tuneable physicochemical properties; so, they are well suited to applications, where the bulk materials would be unsuitable. As distinct from their bulk counterparts, they have a specifically organized surface that allows the structure of their energy bands to respond effectively and immediately to external perturbations and alloying substances. Such a special surface nature makes these materials competitive in application for devices. It is currently known about emerging application of elemental 2*D* materials in many fields such as (opto)electronics, sensing, spintronics, plasmonics, photodetectors, ultrafast lasers, batteries, supercapacitors, thermoelectrics, and biomedicine [7].

In the present article, we review relevant data available in the literature and compare them with our recent results [8–16] based on the computational (numerical) experiments along with the own-constructed software (program) codes. The paper is organized as follows. After the Introduction (current section 1), section 2 reviews the formalism of electron density functional and pseudo-potential from the first principles, algorithm for calculation of the effective electrical charges, electronic spectrum, total energy, mechanical forces, and valuation reliability verification of electronic characteristics. Section 3 includes results and discussions on the modifying electronic characteristics by the local chemical functionalization, particularly, the chemical adsorption on graphene, doping of black phosphorene, effects of the bending strain, static pressure and fluorination. Section 4 deals with the straintronics and defect engineering for graphene and related systems. This section contains methodological grounds for consideration of electronic diffusivity and conductivity, modelling approach for consideration of deformations and structural defects, and effects of some types of strains and point defects on the electron states and electronic transport. The case of graphene with point and linear defects inside the external magnetic field is considered in section 5. Finally, section 6 summarizes the conclusions, which follow from the findings in the previous sections.

2. Properties of the Ground State from the Electron Density

2.1. Formalism of Electron Density Functional and Pseudo-Potential from the First Principles

The density functional theory (DFT) is part of a group of methods from the first principles, otherwise *ab initio*, which allow, based on the characteristics of the crystal structure, to calculate the physical and chemical properties of objects without the use of empirical data.

At the initial stage of the analysis of the crystal structure, the Born–Oppenheimer approximation is used. Based on the ratio of the masses of nuclei and electrons, it is believed that nuclei remain stationary and electrons move in some stationary effective potential created by stationary nuclei and other electrons.

Next, the interactions, which will be accountable in the calculations, are selected as follow. In most cases, the consideration is within the nonrelativistic quantum mechanics, and relativistic effects related to the motion of the electron, such as the dependence of the mass of the electron on its velocity, spin–orbit and spin–spin interactions, are taken into account as corrections. The type of Hamiltonian and the number of electrons contain all the necessary information about the system.

The initial problem is to solve the Schrödinger equation for a many-electron system, but the exact solution of this equation is possible only for some model many-electron systems, such as Fermi particles with short-range interaction and interacting spin chains. Therefore, a number of additional approximating methods are used.

Thus, according to the Hartree–Fock theory, the Schrödinger equation for the system is as follows [17]:

$$\hat{H}\psi' = E\psi', \tag{1}$$

where E is the total energy of the system; H is the complete Hamiltonian containing the kinetic energy of electrons and nuclei of the system, electron–electron, nuclear–nuclear and electron–nuclear interactions; ψ' is the wave function of the system, which depends on the spin and spatial coordinates of all nuclei and electrons. For the possibility of further calculations, it is necessary to use the Born–Oppenheimer approximation. Since the mass of the nucleus is much larger than the mass of the electrons, the motion of the electrons is considered independent, and the full wave function of the system is

$$\psi'(q, Q) \approx \chi(Q)\psi(q, Q), \tag{2}$$

where $\chi(Q)$ is the wave function of the nuclei subsystem, $\psi(q, Q)$ is the wave function of the electrons' subsystem, which is the solution of the Schrödinger equation for electrons at the fixed positions of the nuclei:

$$\hat{H}_e\psi(q, Q) = E(Q)\psi(q, Q). \tag{3}$$

The Hamiltonian of the electrons' subsystem is derived from the complete Hamiltonian, from which the term associated with the kinetic energy of nuclei is subtracted. The energy of the electrons' subsystem will depend on the selected configuration of the cores.

The next step is to specify the form of the wave function of the electrons' subsystem in the one-electron Hartree approximation, where each electron moves independently of the other electrons in some effective potential field generated by nuclei and other electrons. Thus, the wave function of the electrons' subsystem can be represented as the product of one-electron functions (orbitals):

$$\psi = C\prod_{i=1}^{n}\psi_i \,. \tag{4}$$

However, there are a number of shortcomings in the Hartree approximation. Thus, the many-electron wave function does not satisfy Pauli's principle: electrons move as uncorrelated completely, *i.e.*, are independent. These shortcomings are partially eliminated within the Hartree–Fock approximation. In particular, the many-electron wave function is presented as a Slater determinant, *i.e.*, it becomes antisymmetric with respect to the exchange of any pair of the electrons, which satisfies the Pauli principle,

$$\psi = C\begin{vmatrix} \psi_1(1)\alpha(1) & \psi_1(1)\beta(1) & \dots & \psi_n(1)\alpha(1) & \psi_n(1)\beta(1) \\ \psi_1(2)\alpha(2) & \psi_1(2)\beta(2) & \dots & \psi_n(2)\alpha(2) & \psi_n(2)\beta(2) \\ \vdots & \vdots & \ddots & \vdots & \vdots \\ \psi_1(N)\alpha(N) & \psi_1(N)\beta(N) & \dots & \psi_n(N)\alpha(N) & \psi_n(N)\beta(N) \end{vmatrix}. \tag{5}$$

Here, N is the number of electrons, and $n = N/2$ is the number of orbitals. For orthonormal one-electron wave functions, the normalizing factor $C = 1/\sqrt{N!}$. In the general case, the wave function contains a linear combination of Slater determinants corresponding to different variants of orbital filling, *i.e.*, electrons' configurations. For closed shells, the orbitals $\psi_i(\mathbf{r})$ are the solution of the Hartree–Fock equation:

$$\hat{f}_i\psi_i(\mathbf{r}) = \varepsilon_i\psi_i(\mathbf{r}). \tag{6}$$

This equation is nonlinear with respect to the one-electron wave function that significantly complicates the solution. An alternative approach is needed. This approach is the electron DFT. The main advantage of this method is that the correlation effects can be taken into account immediately; it can significantly reduce the calculation time. The DFT is based on the two Hohenberg–Kohn theorems.

According to the 1st theorem, in the ground state, the density of the subsystem of interacting electrons, which are in some external potential, determines this potential to the nearest some additive constant. Meaning of this theorem is that all the properties of the subsystem of

electrons are uniquely determined by their density:

$$\rho(\mathbf{r}) = \sum_i |\psi_i|^2 , \tag{7}$$

where the summation occurs according to the occupied states. Only the existence of such a reciprocal correspondence is noted, but there are no indications as to its form.

The second theorem states that all observed physical quantities could be represented in the form of an electron density functional, including the energy of the system, which has a minimum in the ground state of the system. In essence, this statement is a variational principle formulated in quantum mechanical terms [18].

We give the total energy of the system in the form of an electron density functional. The Hamiltonian of a system consisting of N electrons and n ions within the Born–Oppenheimer approximation has the form

$$\hat{H} = -\sum_{i=1}^{N} \frac{\Delta_i}{2} + \sum_{j>i=1}^{N} \frac{1}{r_{ij}} - \sum_{i=1}^{N}\sum_{k=1}^{N} \frac{Z_k}{r_{ij}} , \tag{8}$$

$$\sum_{k}^{n} \frac{Z_k}{r_{ik}} = V_{\text{ext}}(r_i) . \tag{9}$$

Here, $V_{\text{ext}}(r_i)$ is an external potential characterizing the interaction of electrons and nuclei; $\mathbf{r}_{ij} = |\mathbf{r}_i - \mathbf{r}_j|$, where $\mathbf{r}_i$ is a radius-vector of the i-th electron; and Δ_j is the Laplace operator, which differentiates by the coordinates of the i-th electron.

Expression (8) is written in the atomic system of units, in which $\hbar = 1$, $e = 1$, $m_e = 1$, $1/(4\pi\varepsilon_0) = 1$, where $\hbar$ is the reduced Planck constant (*i.e.*, Dirac constant); e is an electron charge; m_e is an electron mass; ε_0 is a dielectric constant of the vacuum.

By acting H on $\rho(\mathbf{r})$ and choosing as a complete set of observed operators, the Hamiltonian and the momentum operator, we have

$$E[\rho(\mathbf{r})] = T[\rho(\mathbf{r})] + U_{ee}[\rho(\mathbf{r})] + \int \rho(\mathbf{r}) V_{\text{ext}}(\mathbf{r}) d\mathbf{r} , \tag{10}$$

where $T[\rho(\mathbf{r})]$ is kinetic energy functional of electrons, $U_{ee}[\rho(\mathbf{r})]$ is electron interaction energy functional, $\int \rho(\mathbf{r}) V_{\text{ext}}(\mathbf{r}) d\mathbf{r} = V_{\text{ext}}[\rho(\mathbf{r})]$ is functional energy of interaction of electrons and nuclei.

In this form, it is easy to see that all the properties of the system are determined solely by the electron density.

The electron interaction energy functional $U_{ee}[\rho(\mathbf{r})]$ is divided into the Hartree energy functional $E_H[\rho(\mathbf{r})]$ and the exchange–correlation functional $E_{XC}[\rho(\mathbf{r})]$, which takes into account multiparticle effects:

$$U_{ee}[\rho(\mathbf{r})] = E_H[\rho(\mathbf{r})] + E_{XC}[\rho(\mathbf{r})], \tag{11}$$

where

$$E_H[\rho(\mathbf{r})] = \frac{1}{2} \iint \frac{\rho(\mathbf{r})\rho(\mathbf{r}')}{|\mathbf{r} - \mathbf{r}'|} d\mathbf{r} d\mathbf{r}' .$$

Thus, expression (10) has the form

$$E[\rho(\mathbf{r})] = T[\rho(\mathbf{r})] + \frac{1}{2}\iint \frac{\rho(\mathbf{r})\rho(\mathbf{r}')}{|\mathbf{r}-\mathbf{r}'|}\,d\mathbf{r}d\mathbf{r}' + \int \rho(\mathbf{r})V_{\text{ext}}(\mathbf{r})d\mathbf{r} + E_{XC}[\rho(\mathbf{r})]\,. \quad (12)$$

By varying this functional taking into account the normalization condition $\int \rho(\mathbf{r})\,d\mathbf{r} = N$, we obtain the Kohn–Sham equation [19, 20]:

$$\left(-\frac{\Delta_i}{2} + V_{\text{eff}}(\mathbf{r})\right)\psi_i(\mathbf{r}) = \varepsilon_i\psi_i(\mathbf{r})\,, \quad (13)$$

where

$$V_{\text{eff}} = \int \frac{\rho(\mathbf{r}')}{|\mathbf{r}-\mathbf{r}'|}\,d\mathbf{r}' + V_{\text{ext}}[\rho(\mathbf{r})] + V_{XC}(\mathbf{r})$$

is some self-consistent effective potential, $\psi_i(\mathbf{r})$ is a single-particle wave functions, which describe the motion of electrons in the potential V_{eff}.

One of the main problems of the theory of electron density functional is the lack of an analytical expression of general form for the exchange–correlation functional (except for systems without interaction). There are various approximations in this regard [21].

Within the approximation of the local density, the exchange–correlation functional is given by the expression

$$E_{XC}[\rho(\mathbf{r})] = \int \varepsilon[\rho(\mathbf{r})]\rho(\mathbf{r})\,d\mathbf{r}\,, \quad (14)$$

where $\varepsilon(\rho)$ is the exchange–correlation energy of a homogeneous electron gas with density ρ. Thus, the value of the exchange–correlation energy at a given point is determined exclusively by the value of the electron density at the same point.

After determining the explicit type of exchange–correlation functional, it is necessary to choose the basis set in the space of electron states by presenting the required electron wave functions in the form of a linear combination of basis functions with some functional coefficients. As basis, you can choose, *e.g.*, plane waves, linearized plane waves, attached plane waves, orthogonalized plane waves and others. It is known that the number of basis functions of the Hamiltonian affects directly the time of calculation of eigenvalues; namely, this time is proportional to the cube of the number of basis functions. This can be achieved by choosing the basis functions as close as possible to the eigenwave functions of the electrons in the structure under study. The basis for decomposition can be selected as a set of plane waves. However, the use of such a basis without any modifications is not effective, because it is necessary to use the number of plane waves of the order of 10^5–10^6.

The idea of the pseudo-potential construction is to 'smooth' the wave functions of electrons near the atomic nucleus. In this case, only valence electrons are considered, because the vast majority of physical properties of systems are determined by the behaviour of valence elec-

trons. Since the wave functions of the core electrons do not change with the change of the atom environment, *i.e.*, remain the same as in the free atom, these electrons can be ignored, and it is considered that their influence is limited by changing the effective ion charge. Therefore, the interaction potential of electrons and ions is replaced by a weaker potential, which is the primary ion potential at distances greater than some r_c, and at smaller distances, it is replaced by a smoother one [22]. This causes a significant reduction in the number of basis functions that simplifies greatly the solution at distances less than r_c. Let $V(\mathbf{r})$ is some self-consistent effective potential. The Schrödinger equation, which must be satisfied with the wave functions of valence electrons, has the form

$$-\frac{\Delta}{2}\psi^{\upsilon} + V(\mathbf{r})\psi^{\upsilon} = \varepsilon_{\upsilon}\psi^{\upsilon}(\mathbf{r}). \tag{15}$$

A similar equation must be satisfied with the wave functions of the core electrons:

$$-\frac{\Delta}{2}\phi^{c} + V(\mathbf{r})\phi^{c} = \varepsilon_{c}\phi^{c}(\mathbf{r}). \tag{16}$$

As basis functions, it is proposed to use the orthogonalized plane waves as the waves, which are previously orthogonal to the core wave functions. The equation for the orthogonalized plane waves has the form

$$\chi^{\mathrm{OPW}}(\mathbf{k}-\mathbf{K}) = (1-\hat{P})|e^{i(\mathbf{k}-\mathbf{K})\cdot\mathbf{r}}\rangle, \tag{17}$$

where $\hat{P} = \sum_{c,\mathbf{R}} |\phi^{c}_{\mathbf{R}}\rangle\langle\phi^{c}_{\mathbf{R}}|$ is a projection operator that projects any functions on core states, $\phi^{c}_{\mathbf{R}} = \phi^{c}(\mathbf{r}-\mathbf{R})$ is a core wave function with centre at the point $\mathbf{R}$, and $\mathbf{K}$ is a reciprocal lattice vector.

Then, the set for orthogonalized plane waves of type (17) has the form

$$\psi_{\mathbf{k}}(\mathbf{r}) = \sum_{\mathbf{K}} a_{\mathbf{K}}(\mathbf{k})(1-\hat{P})|e^{i(\mathbf{k}-\mathbf{K})\cdot\mathbf{r}}\rangle; \tag{18}$$

moreover, $\Sigma_{\mathbf{K}} a_{\mathbf{K}}|\exp(i(\mathbf{k}-\mathbf{K})\cdot\mathbf{r})\rangle = \varphi^{PS}(\mathbf{r})$. The pseudo-wave function φ^{PS} is smooth both in the vicinity of the core and outside (where $\hat{P} = 0$); moreover, outside this vicinity, it is exactly equal to the true wave function $\psi_{\mathbf{k}}(\mathbf{r})$ that is the main advantage of the pseudo-potential construction.

Using formula (18), the Schrödinger equation for valence electrons is as follows:

$$-\frac{\Delta}{2}\varphi^{PS} + V(\mathbf{r})\varphi^{PS} - \left(-\frac{\Delta}{2} + V(\mathbf{r})\right)\hat{P}\varphi^{PS} + \varepsilon^{\upsilon}\hat{P}\varphi^{PS} = \varepsilon^{\upsilon}\varphi^{PS}. \tag{19}$$

Let us write Eq. (19) in a form

$$-\frac{\Delta}{2}\varphi^{PS} + W(\mathbf{r})\varphi^{PS} = \varepsilon^{\upsilon}\varphi^{PS}, \tag{20}$$

where

$$W(\mathbf{r}) = V(\mathbf{r}) - \left(-\frac{\Delta}{2} + V(\mathbf{r})\right)\hat{P} + \varepsilon^{\upsilon}\hat{P}$$

is the pseudo-potential proper.

Note, since the wave functions of both valence electrons and core ones satisfy the Schrödinger equations of type (15) and (16), respectively, then, acting on the design operator $\hat{P}$ at Eq. (15), we obtain:

$$\left(-\frac{\Delta}{2}+V(\mathbf{r})\right)\hat{P}=\varepsilon^{c}|\varphi^{c}_{\mathbf{R}}\rangle\langle\varphi^{c}_{\mathbf{R}}|. \tag{21}$$

Therefore, pseudo-potential can be written in another form:

$$W(\mathbf{r})=V(\mathbf{r})+\sum_{c,\mathbf{R}}(\varepsilon^{\upsilon}-\varepsilon^{c})|\varphi^{c}_{\mathbf{R}}\rangle\langle\varphi^{c}_{\mathbf{R}}|. \tag{22}$$

It should be noted that no new approximations were used in deriving Eq. (22). Therefore, the eigenvalues of energy for Eqs. (15) and (20) coincide. In addition, the pseudo-potential is nonlocal, as it depends not only on coordinates but also on energy, while the potential $V(\mathbf{r})$ is local. Of course, this causes a significant complication of calculations, but the advantages of using pseudo-potential easily outweigh the estimated costs associated with nonlocality. Also, note that the pseudo-potential $W(\mathbf{r})$ is relatively weak in comparison with $V(\mathbf{r})$, as $V(\mathbf{r})$ is responsible for self-consistent effective-'attraction' of electrons in the system and is negative, while the second term of equation (22) is extremely positive. Thus, Bachelet, Hamann, and Schlüter proposed an analytical pseudo-potential suitable for the above conditions from the first principles used by us [23, 24].

2.2. Algorithm for the Calculation of the Effective Electric Charges in the Polyatomic System

The calculation of the integral characteristics of the electron density distribution in polyatomic systems, namely, the effective charges on atoms, is widely used in many fields of physics and chemistry. However, the exact definition of this quantity encounters a problem: how to divide the electron density in the space between nuclei between atoms. For methods, which use the muffin-tin (MT) approximation, this distribution occurs in the usual way, but the result depends on the choice of MT spheres and is not an objective characteristic of the object. An alternative procedure is the well-known Mulliken population analysis [25].

The probability of electron-density distribution in a molecule is determined by the function $\rho(\mathbf{r})$; in addition, the normalization requires that $\int\rho(\mathbf{r})\,d\mathbf{r}=n$; here, n is the total number of electrons [26]. For the one-determinant wave function, in which molecular orbitals are represented as a linear combination of N basis functions $\{\varphi_{\mu}\}$, the probability function is

$$\rho(\mathbf{r})=\sum_{\mu}^{N}\sum_{\nu}^{N}P_{\mu\nu}\varphi_{\mu}\varphi_{\nu} \tag{23}$$

with the density matrix elements $P_{\mu\nu}$. According to Mulliken, population analysis can be performed by integrating Eq. (23); then,

$$\int \rho(\mathrm{r})\, d\mathrm{r} = \sum_{\mu}^{N}\sum_{\nu}^{N} P_{\mu\nu}S_{\mu\nu} = n\,, \tag{24}$$

where $S_{\mu\nu}$ is a matrix of the overlapping integrals on the basis functions, which are normalizing, *i.e.*, $S_{\mu\mu} = 1$. Diagonal terms $P_{\mu\mu}$ characterize the full population of the orbital φ_μ. The sum $Q_{\mu\nu}$ of non-diagonal components in expression (24), $P_{\mu\nu}S_{\mu\nu}$ and $P_{\nu\mu}S_{\nu\mu}$, equal in magnitude, is called the overlap population density,

$$Q_{\mu\nu} = 2P_{\mu\nu}S_{\mu\nu}\ (\mu \neq \nu). \tag{25}$$

Note that the overlap population is associated with two basic functions φ_μ and φ_ν, which can be on the same atom and on the two different atoms. Then, the full electronic charge can be given as the sum of two parts, one of which is related to disparate basis functions and the other is related to a pair of basis functions:

$$\sum_{\mu}^{N} P_{\mu\mu} + \sum_{\mu}^{N}\sum_{\nu}^{N} Q_{\mu\mu} = n\,. \tag{26}$$

Such a presentation of the electron distribution is not always convenient. Sometimes, it is desirable to divide the full electronic charge into contributions, which relate to individual basis functions. In this case, the overlap population $Q_{\mu\nu}$ is divided equally between the functions φ_μ and φ_ν (this division scheme is arbitrary and not unique) and is added to each $P_{\mu\mu}P_{\nu\nu}$. Then, we can consider the population of the atomic orbital φ_μ:

$$q_\mu = P_{\mu\mu} + \sum_{\nu\neq\mu} P_{\mu\nu}S_{\mu\nu}\,. \tag{27}$$

Therefore, the total electron density on the A atom has the form

$$q_A = \sum_{\mu}^{A}\left(P_{\mu\mu} + \sum_{\nu\neq\mu} P_{\mu\nu}S_{\mu\nu}\right) \tag{28}$$

with summation for all functions φ_μ on the atom A [27].

Consequently, the total electronic charge on atom A is determined by the difference $Z_A - q_A$, namely,

$$q_A = Z_A - \int_{V_A} \rho(\mathrm{r})\, d\mathrm{r}\,, \tag{29}$$

where Z_A is the number of the element A in the periodic table, V_A is the spherical volume of the A atom.

2.3. Momentum Space Formalism for the Calculation of the Electronic Spectrum, Total Energy, and Mechanical Forces

For non-periodic systems, such as an imperfect crystal, thin film or cluster, the problem of lack of periodicity is bypassed by the superlattice method [28–30], which creates a supercell that is transmitted in

space. In the modelling of non-periodic systems, such as thin film or clusters, the isolation of the transmitted objects from each other is provided by a vacuum gap between them [29].

The general periodicity of the crystal (or artificial) lattice creates a periodic potential and, thus, imposes the same periodicity on the electron density (Bloch's theorem). The Kohn–Sham potential of the periodic system manifests the same periodicity as the lattice, and the Kohn–Sham orbitals can be written based on Bloch's theorem:

$$\psi(\mathbf{r}) = \psi_i(\mathbf{r}, \mathbf{k}) = \exp(i\mathbf{k}\cdot\mathbf{r})\, u_i(\mathbf{r}, \mathbf{k}), \tag{30}$$

where $\mathbf{k}$ is the vector within the first Brillouin zone (*BZ*). The index i runs through all the possible electron states. The function $u_i(\mathbf{r}, \mathbf{k})$ has the periodicity of the spatial lattice and can be expanded in a series by plane waves. This justifies the use of plane waves as the general basis we have chosen to decompose the periodic part of the orbitals. Since plane waves form a complete and orthonormal set of functions, their use for the expansion of single-particle orbitals has the form

$$\psi_j(\mathbf{k}, \mathbf{r}) = \frac{1}{\sqrt{N_0}\sqrt{\Omega}} \sum_{\mathrm{G}} b_j(\mathbf{k} + \mathrm{G}) \exp\left(i\,(\mathbf{k} + \mathrm{G})\cdot\mathbf{r}\right), \tag{31}$$

where $\mathbf{G}$ is a reciprocal lattice vector, Ω is the volume of unit cell that fill a crystal (or artificial superlattice in the case of non-periodic objects).

After the Fourier transform, Eq. (13) is in the reciprocal space as

$$\sum_{\mathrm{G}} \left[\left\{ \frac{\hbar^2}{2m} (\mathbf{k} + \mathrm{G})^2 - \varepsilon_j \right\} \delta_{\mathrm{G},\mathrm{G}'} + V_{KS}(\mathbf{k} + \mathrm{G}, \mathrm{k} + \mathrm{G}') \right] b_j(\mathbf{k} + \mathrm{G}) = 0\,. \tag{32}$$

Here, the Fourier representation of the Kohn–Sham potential is

$$V_{KS}(\mathbf{k} + \mathbf{G}, \mathbf{k} + \mathbf{G}') = V_{PS}(\mathbf{k} + \mathbf{G}, \mathbf{k} + \mathbf{G}') + V_H(\mathbf{G}' - \mathbf{G}) + V_{XC}(\mathbf{G}' - \mathbf{G}), \tag{33}$$

moreover, the exchange–correlation potential is [24]

$$V_{XC} = \varepsilon_{XC} - \frac{r_s}{3} \frac{d\varepsilon_{XC}}{dr_s}, \tag{34}$$

where $\varepsilon_{XC} = \varepsilon_X + \varepsilon_C$. As known, for unpolarised electron gas [24],

$$\varepsilon_X = -\frac{0.4582}{r_s}, \tag{35}$$

$$\varepsilon_C = \begin{cases} -\dfrac{0.1432}{1 + 1.0529\sqrt{r_s} + 0.3334 r_s} & (r_s \geq 1), \\ -0.0480 + 0.0311 \ln r_s - 0.0116 r_s + 0.0020 r_s \ln r_s & (r_s < 1); \end{cases} \tag{36}$$

here, r_s (in a.u.) is the radius of the Wigner–Seitz sphere per electron determined by formula $\rho^{-1} = 4\pi r_s^3/3$.

Using the Poisson's equation, the Fourier transform of Hartree potential can be obtained:

$$V_H(\mathbf{G}) = \frac{4\pi e^2 \rho(\mathbf{G})}{|\mathbf{G}|^2}. \quad (37)$$

In the general case, the expressions describing the potentials of interactions are complex. The use of atomic bases, which contain the inversion operation in their group of point symmetry, leads to the fact that the Fourier components in the expansions of all expressions are real.

The main value in the DFT formalism is the density of the electronic charge. It is estimated on the basis of a self-consistent solution of Eq. (32), which must be performed at the all points of the irreducible part of the first *BZ*:

$$\rho(\mathbf{G}) = \frac{2}{N_T} \sum_k \sum_j \sum_{\alpha \in T} \sum_{\mathbf{G}'} b_j^*(\mathbf{k} + \mathbf{G}' + \alpha\mathbf{G}) b_j(\mathbf{k} + \mathbf{G}'), \quad (38)$$

where index j runs through all occupied states, $\mathbf{k}$ belongs to the first *BZ*, N_T is a number of operations α in the point group T of the atomic basis, and factor '2' takes into account the spin degeneracy.

The calculated efforts can be reduced by using the special mean-value point method. There are different approaches to choosing these points. Thus, it is possible to use uniform or nonuniform grids of points, it is possible to replace the summation by a finite number of special points up to one point in the *BZ* with acceptable accuracy [31–323334]. It is possible to be limited only to the Γ-point within the first *BZ*, especially, for artificial periodic systems with a large supercell. The latter can be illustrated by the following. It is known that the volume of a Wigner–Seitz cell in reciprocal space (the volume of the first *BZ*) and the volume of a Wigner–Seitz cell in the crystal-lattice space are related by the formula

$$\Omega_{BZ} = (2\pi)^3 / \Omega_{\text{cell}}. \quad (39)$$

If the volume of the Wigner–Seitz cell for the crystal is large, that often occurs when using the superlattice method, the volume of the *BZ* is small, that is, it is contracted to a point [29, 30].

The distribution of electrons by energy is obtained by numerical calculation of the derivative $\lim_{\Delta E \to 0} \Delta N / \Delta E$, where ΔN is the number of allowed states per energy interval ΔE from the one-particle energy spectrum obtained during diagonalization of the Kohn–Sham matrix for Eqs. (32). According to the DFT methodology, the number of occupied states (at T = 0 K) was determined by half the number of electrons in the atomic basis (due to the disregard of electron-spin polarization).

The total energy per unit cell is [28]

$$\frac{E_{\text{tot}}}{\Omega} = \sum_{\mathbf{k},\mathbf{G},i} |\psi_i(\mathbf{k}+\mathbf{G})|^2 \frac{\hbar^2(\mathbf{k}+\mathbf{G})^2}{2m} + \frac{4\pi e^2}{2} \sum_{\mathbf{G}\neq\mathbf{0}} \frac{|\rho(\mathbf{G})|^2}{|\mathbf{G}|^2} + \sum_{\mathbf{G}} \varepsilon_{XC}(\mathbf{G})\rho^*(\mathbf{G}) +$$
$$+ \sum_{\mathbf{k},\mathbf{G},\mathbf{G}',i,l,s} S_s(\mathbf{G}-\mathbf{G}')\Delta V_{l,s}^{NL}(\mathbf{k}+\mathbf{G},\mathbf{k}+\mathbf{G}')\psi_i(\mathbf{k}+\mathbf{G})\psi_i^*(\mathbf{k}+\mathbf{G}') + \quad (40)$$
$$+ \sum_{\mathbf{G}\neq\mathbf{0},s} S_s(\mathbf{G})V_s^L(\mathbf{G})\rho^*(\mathbf{G}) + \left\{\sum_s \alpha_s\right\}\left\{\Omega^{-1}\sum_s Z_s\right\} + \Omega^{-1}\gamma_{\text{Ewald}},$$

where $\mathbf{k} \in 1^{\text{st}}$ *BZ*, $\mathbf{G}$ is the reciprocal lattice vector, $\psi_i(\mathbf{k}+\mathbf{G})$ is the wave function, i denotes the occupied states for a given $\mathbf{k}$, $\rho(\mathbf{G})$ is the coefficient of the valence electron density in Fourier expansion, s numbers the atoms in the unit cell, $S_s(\mathbf{G})$ is a structural factor, V_s^L is local (l-independent) spherically-symmetric pseudo-potential, l denotes a quantum orbital number, $\Delta V_{l,s}^{NL}$ is nonlocal (l-dependent) addition to V_s^L, Z_s is the ion charge, γ_{Ewald} is the Madelung energy of point ions in a homogeneous negative background.

The force acting on the atom s is a negative derivative of E_{tot} with respect to the atomic basis vector τ_s. Expressions containing an implicit derivative of the wave function are zero by the Hellman–Feynman theorem. Therefore, the calculation of forces is performed by the formula [28]

$$\mathbf{F}^s = \mathbf{F}_e^s + \mathbf{F}_c^s, \quad (41)$$

where the first and second terms at the right correspond to electron and ion interactions' components, respectively,

$$\mathbf{F}_e^s = i\Omega_c \sum_{\mathbf{G}} \rho^*(\mathbf{G})\mathbf{G}e^{-i\mathbf{G}\cdot\mathbf{t}_s}V_s^L(\mathbf{G}) -$$
$$- \sum_{i,\mathbf{G},\mathbf{G}',l} n_i\psi_i^*(\mathbf{k}_i+\mathbf{G}')\psi_i(\mathbf{k}_i+\mathbf{G})(\mathbf{G}-\mathbf{G}')e^{-i(\mathbf{G}-\mathbf{G}')\cdot\mathbf{t}_s}V_{s,l}^{NL}(\mathbf{k}_i+\mathbf{G},\mathbf{k}_i+\mathbf{G}'), \quad (42)$$

$$\mathbf{F}_c^s = 2Z_s\sum_{s'\neq s} Z_{s'}\frac{4\pi}{\Omega_c}\sum_{\mathbf{G}\neq 0}\left(\frac{\mathbf{G}}{|\mathbf{G}|^2}\sin\left(\mathbf{G}\cdot(\mathbf{t}_s-\mathbf{t}_{s'})\right)\exp\left(-\frac{|\mathbf{G}|^2}{4\eta^2}\right)\right) +$$
$$+2Z_s\sum_{s'\neq s} Z_{s'}\sum_{\mathbf{l}}\left(\frac{\mathbf{x}\,\text{erfc}\left(\eta|\mathbf{x}|\right)}{|\mathbf{x}|^3} + \frac{2\eta\mathbf{x}}{\sqrt{\pi}|\mathbf{x}|^2}\exp\left(-|\eta\mathbf{x}|^2\right)\right). \quad (43)$$

Here, $\mathbf{x} = \mathbf{l} + \tau_s - \tau_{s'}$, Ω_c is the volume of the cell per atom, τ_s is the basis vector of the atom s in the cell, $Z_{s'}$ is the charge of the core, $\mathbf{l}$ is the lattice vector; the Ewald summation over $\mathbf{l}$ excludes the term, in which, for $s = s'$, the vector $\mathbf{l} = \mathbf{0}$; η is the parameter of convergence of the sum, *e.g.*, in the complementary error function (erfc).

2.4. Valuation Reliability Verification of Electronic Characteristics: Calculation of Electric Charges within the Atom Vicinity

The accuracy of computer calculations is determined by the chosen methods and approximations used in the computational techniques. In the software package used by authors, formalisms from the first principles (DFT, Hellman–Feynman theorem, pseudo-potential construction from the first principles, Fourier transform for the periodical systems, *BZ* sampling with integration, exchange–correlation potential, *etc*.) are used, which do not leave error in estimates provided, *i.e.*, they are used correctly.

Algorithmic calculation errors inevitably arise and are associated with numerical integration, differentiation, limitation of infinite sums in calculations of exchange–correlation potentials, integration by a finite number of points in the Brillouin zone, limitation of self-satisfied iterations, Fourier-transform calculations, *etc*. For example, the integration within the Brillouin zone was replaced by the calculation at one mean-value point of the Brillouin zone, namely, the Γ-point, which is described in paragraph 2.3. Iterations of self-matching are terminated, if the results of the current and previous iterations calculated coincide with the pre-selected accuracy; their number is varied depending on the calculated object, but usually our results coincide after 4–5 iterations. The number of plane waves in the wave function packet is truncated by trial calculations and evaluation of the physicality of the results obtained from general ideas about the modelled nanostructure or in comparison with the results obtained by other authors; the number of plane waves is chosen to be about 20–25 waves per atom in the basis. Increasing the number of terms in the Fourier expansion of the wave function, electron density, *etc*., self-matching iterations, and the number of special mean-value points in the Brillouin zone rapidly increases the computer time. Therefore, the calculation parameters are chosen optimal.

The results of control calculations of effective electric charges in the vicinity of H, C, P, O, F, and Cl atoms used in the investigation are shown in Fig. 1 and Table 1. The calculations are performed according

Table 1. **Atomic radii values used in the reviewed and analysed study**

Atom	Number of valence electrons	Calculated radius R, Å	Van der Waals radius R_{VdW}, Å
H	1	1.29	1.2
C	4	1.75	1.7
P	5	1.85	1.9
O	6	1.85	1.4
F	7	1.96	1.4
Cl	7	1.96	1.8

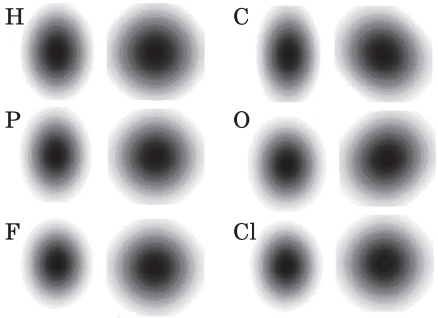

Fig. 1. Cross-section of valence electron density for H, C, P, O, F, and Cl atoms in the [110] and [100] planes (from left to right)

to the algorithms described above in the previous two subsections.

Since the calculation algorithm assumes the presence of translational symmetry in the studied atomic system, although it represents an isolated atom, an artificial rhombic superlattice is created, the primitive cell of which is a rectangular parallelepiped based on the primitive translation vectors **a**, **b**, **c**. In this regard, for the convenience of calculations, the crystallographic axes are conjugated with the axes of the Cartesian co-ordinate system *Oxyz*. The object of study is to determine the parameters of the superlattice and atomic basis. The size of the primitive unit cell is chosen so that the translationally repeating individual atoms do not affect each other. The number of plane waves in the packet of the total wave function is 389; the integration by volume of the Brillouin artificial superlattice is replaced by the calculation at the Γ-point, and the number of iterations of self-matching is 3 for all atoms. There are calculated spatial distributions of valence electron density, their cross sections, electron density of states and charges in the spherical neighbourhood of atoms with different radius, which is varied from the value of the core radius determined by the selected pseudo-potential [23, 24] to the value, at which the valence electron density disappeared (with a step of 0.05 Å). As a criterion of limiting the area of space occupied by the atom, we consider the distance where the total value of the positively charged ionic core density and negatively charged valence electron density becomes less $0.2e$ per volume. Analysing and comparing the calculated cross sections of the spatial distributions of the valence electron density, shown in Fig. 1, the values of effective electric charges in the spherical neighbourhood of atoms with different radius, as shown in Table 1, with known from the literature [35] demonstrate their good coincidence. This allows us to assume that the results of all calculations have a high degree of reliability.

3. Modifying Electronic Characteristics through the Local Chemical Functionalization

3.1. Chemical Adsorption of Graphene

Changing the electronic properties of two-dimensional semi-metal graphene layer is achievable through the functionalization, which can be realized in various ways, one of which is the chemisorption or physisorption of atoms or molecules (adsorbates) on its surface.

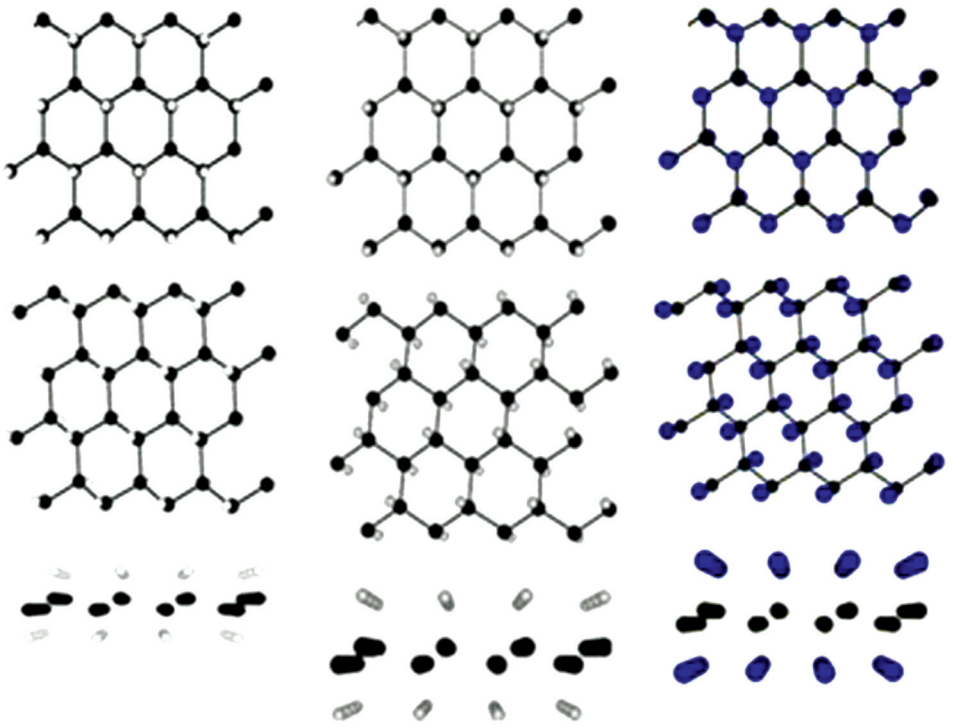

Fig. 2. Atomic structure of (*a*) graphane, (*b*) fluorographene, and (*c*) chlorographene (views from different angles) [9]

Functionalized graphenelike structures include graphane [36–39], fluorographene [39–42], and chlorographene [39, 43, 44], which have a similar structure. Graphane is a class of hydrogenated graphene structures, in which each carbon atom of the graphene layer is covalently bonded to the hydrogen atom by a sp^3-bond. Fluorographene and chlorographene have a similar structure and type of hybridization with F and Cl atoms, respectively. The atomic structures of graphane, fluorographene, and chlorographene are shown in Fig. 2.

We propose a new way of local chemical adsorption of graphenelike structures by combining non-functionalized and functionalized areas of graphene, formed according to a pre-planned pattern into a single whole system, *i.e.*, with creating by certain technological methods the separate areas of local adsorption of various chemical elements (*e.g.*, hydrogen, fluorine, chlorine) on the graphene sheet, we can organize the structure on a common carbon base. Similar experimental combinations of non-functionalized and functionalized graphene are discussed in Refs. [45–47].

To detect changes in the electronic properties of graphene-based structures due to local chemical adsorption of graphene, atomic model

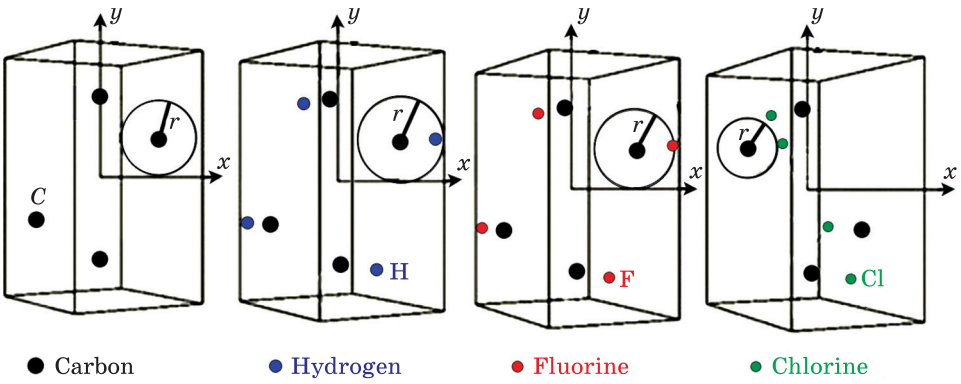

Fig. 3. Primitive cells with atomic basis for objects 1–4 from left to right: graphene, graphane, fluorographene, and chlorographene. Spheres (of r radius) mark areas of the calculated electric charge [9]

objects are developed for a computational experiment using the above-described algorithm. An artificial rhombic superlattice is created, the primitive cell of which is a rectangular parallelepiped built on the vectors of primitive translations **a**, **b**, **c**. In this regard, for the convenience of calculations, the crystallographic axes are conjugated with the axes of the Cartesian co-ordinate system *Oxyz*. The subject of study is to determine the parameters of the superlattice and atomic basis. Along the z direction, perpendicular to the surface of the graphene sheet, the size of the primitive cell is chosen so that translationally repeating sheets do not affect each other, while, in the xy plane, graphene sheets are either infinite or with finite sizes:

- object 1: infinite graphene sheet, symbol (C), primitive cell sizes: a = 2.46 Å, b = 4.26 Å, c = 2.65 Å; the atomic basis consists of 4 C atoms (Fig. 3);
- object 2: infinite graphane sheet, symbol (CH), primitive cell sizes: a = 2.52 Å, b = 4.56 Å, c = 3.18 Å; the atomic basis consists of 4 C atoms and 4 H atoms (see Fig. 3);
- object 3: infinite fluorographene sheet, symbol (CF), primitive cell sizes: a = 2.55 Å, b = 4.65 Å, c = 3.70 Å; the basis consists of 4 C atoms and 4 F atoms (see Fig. 3);
- object 4: infinite chlorographene sheet, symbol (CCl), primitive cell sizes: a = 2.85 Å, b = 5.16 Å, c = 4.76 Å; the basis consists of 4 C atoms and 4 Cl atoms (see Fig. 3);
- object 5: two-dimensional finite graphene/graphane structure; symbol (C/CH); cell sizes: a = 13.23 Å, b = 10.58 Å, c = 5.29 Å; the basis consists of 48 atoms, of which 32 C atoms and 16 H atoms;
- object 6: two-dimensional finite graphene/fluorographene structure; symbol (C/CF); cell sizes: a = 13.76 Å, b = 11.11 Å, c = 6.88 Å; the

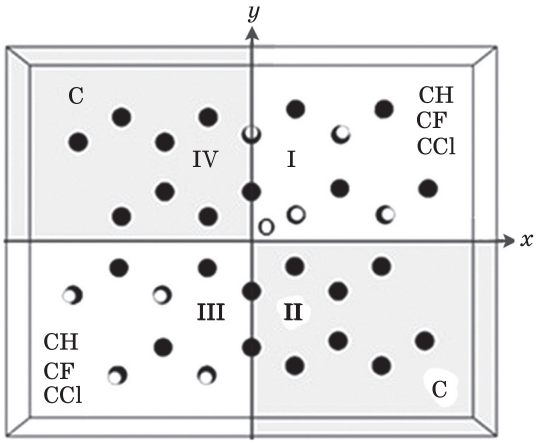

Fig. 4. Primitive cells with atomic basis of the finite-sized structures: graphene/graphane, graphene/fluorographene, graphene/chlorographene. Roman numerals I–IV denote coordinate quarters; x, y — coordinate axes [9]

basis consists of 48 atoms, of which 32 C atoms and 16 F atoms;

object 7: two-dimensional finite graphene/chlorographene structure; symbol (C/CCl); cell sizes: a = 15.35 Å, b = = 12.70 Å, c = 7.41 Å; the basis consists of 48 atoms, of which 32 C atoms and 16 Cl atoms.

The calculation is performed only for Γ-point of the *BZ*.

Structures of objects 5–8 with local chemical adsorption of graphene are modelled as finite atomic structures with the chess alternation of graphene and graphane/fluorographene/chlorographene regions [9]. When modelling finite-size systems, the isolation of the transmitted objects from each other is provided by a vacuum gap between them. The parameters of primitive cells are chosen to be larger in order to prevent interaction between atoms of atomic bases during translation. Primitive cells of superlattices with the inclusion of the atomic basis for objects 5–8, which are similar, are shown in Fig. 4.

Using the author's code [48], the spatial distributions of valence electron densities, electron densities of states, band gap widths, and charges on atoms and at regions of atomic model objects were calculated by methods of electron DFT and pseudo-potential from the first principles.

Analysing the calculated spatial distributions of valence electron densities, shown in Fig. 5, the change of hybridization from sp^2 to sp^3 is confirmed during the functionalization of graphene by atoms of hydrogen, fluorine, chlorine. Thus, in Fig. 5, *a*, the density distribution is

Table 2. **Values of electric charges on the carbon cores for objects 1–4 [9]**

Number of C atom in the atomic base	Object 1 (C)	Object 2 (CH)	Object 3 (CF)	Object 4 (CCl)
1	3.373	3.853	3.742	3.162
2	3.373	3.853	3.742	3.162
3	3.373	3.853	3.742	3.162
4	3.373	3.853	3.742	3.162

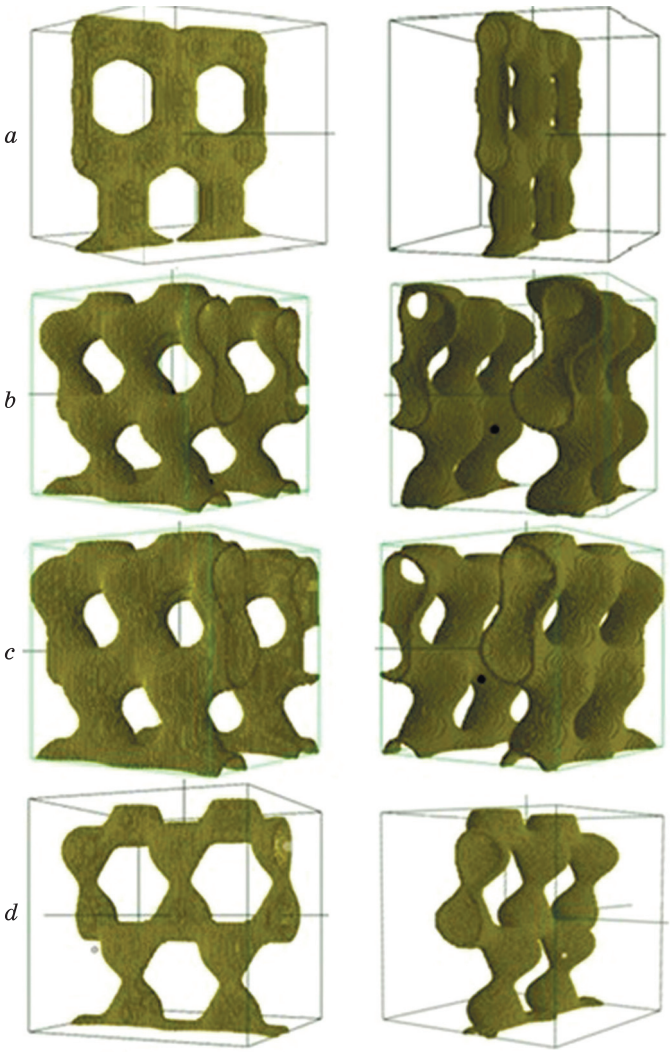

Fig. 5. Spatial distribution of the valence electrons' density (for 0.5–0.6 definition of the maximum) in (*a*) graphene with sp^2-hybridization of carbon atoms, (*b*) graphane, (*c*) fluorographene, and (*d*) chlorographene with sp^3-hybridization of C atoms [9]

flat, and, in Fig. 5, *b*–*d*, the distribution acquires three-dimensional forms of tetrahedral symmetry.

Table 2 shows the values of electric charges on carbon atoms of objects 1–4, which are estimated by formula (29) in a spherical volume centred in the carbon cores of the corresponding structures with radius r, which is half the distance between carbon atoms (see Fig. 3). Electric charges are calculated in the atomic system of units, in which the charge of the electron is equal to 1.

From Fig. 5 and Table 2, it is seen that the numerical values of the electric charges of objects 1–4 are the same on the all carbon atomic cores in the infinite sheets of graphene, graphane, fluorographene, and

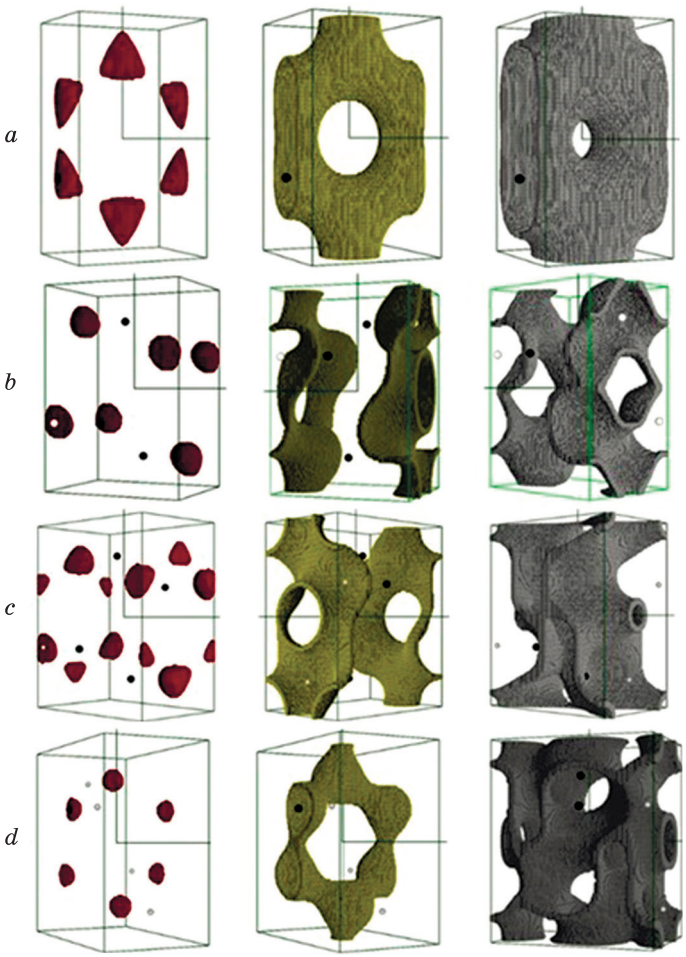

Fig. 6. Spatial distribution of the valence electrons' density (from left to right for 0.9–1.0; 0.5–0.6; 0.1–0.2 definition of the maximum) of (*a*) graphene with sp^2-hybridization of carbon atoms, (*b*) graphane, (*c*) fluorographene, and (*d*) chlorographene with sp^3-hybridization of C atoms [9]

chlorographene. The spatial distributions of the valence electron density for these atomic objects are shown in Fig. 6, confirming this homogeneity [9].

Another situation is with charge distributions in finite-size structures with local chemical adsorption of graphene. There is a redistribution of electric charges; moreover, a change in the electric charges is observed at atomic cores located at the joints, *i.e.*, at the interface between the regions of graphene and graphane, graphene and fluorographene, graphene and chlorographene. Numerical values of electric charges on the atomic cores of objects 5–7 are given in Table 3.

Spatial distribution of valence electron density for finite-size structures with local chemical adsorption of graphene, as shown in Fig. 7, demonstrates the charge regions of higher density localized in functionalized areas, namely, graphane, fluorographene, chlorographene.

Table 4 shows the widths of the electronic band gaps of objects 1–7, which are presented in a.u. and eV. It is seen that the infinite sheet of graphene has a zero band gap. After its functionalization by hydrogen, fluorine, and chlorine atoms, the band gap increases. Analysing objects 1–4 (endless sheets), we see that the width of the band gap of graphane is the maximum and is equal to 3.81 eV; for a sheet of chlorographene, it is of 1.36 eV; for a sheet of fluorographene, it is of 0.27 eV. Among objects 5–7 (the finite structures with chemical adsorption of graphene), the structure of graphene/chlorographene has the largest width of

Table 3. **Values of electric charges on the carbon cores with local chemical adsorption of graphene for objects 5–7 [9]**

Number of C atom in the atomic base	Object 5 C/CH	Object 6 C/CF	Object 7 C/CCl
1	3.912	3.842	3.952
2	3.747	3.489	3.598
3	3.309	3.284	3.519
4	3.953	3.914	3.977
5	3.995	3.880	3.572
6	3.998	3.996	3.893
7	3.991	3.757	3.411
8	3.999	3.997	3.991
9	3.460	3.394	3.599
10	3.097	3.142	3.376
11	3.429	3.277	3.428
12	3.077	3.167	3.404
13	3.706	3.258	3.372
14	3.968	3.812	3.535
15	3.444	3.201	3.374
16	3.996	3.979	3.519
17	3.968	3.812	3.535
18	3.706	3.258	3.372
19	3.996	3.979	3.519
20	3.444	3.201	3.374
21	3.097	3.142	3.376
22	3.460	3.394	3.599
23	3.077	3.167	3.404
24	3.429	3.277	3.428
25	3.998	3.996	3.893
26	3.995	3.880	3.572
27	3.999	3.997	3.991
28	3.991	3.757	3.411
29	3.747	3.489	3.598
30	3.912	3.842	3.952
31	3.953	3.914	3.977
32	3.309	3.284	3.519

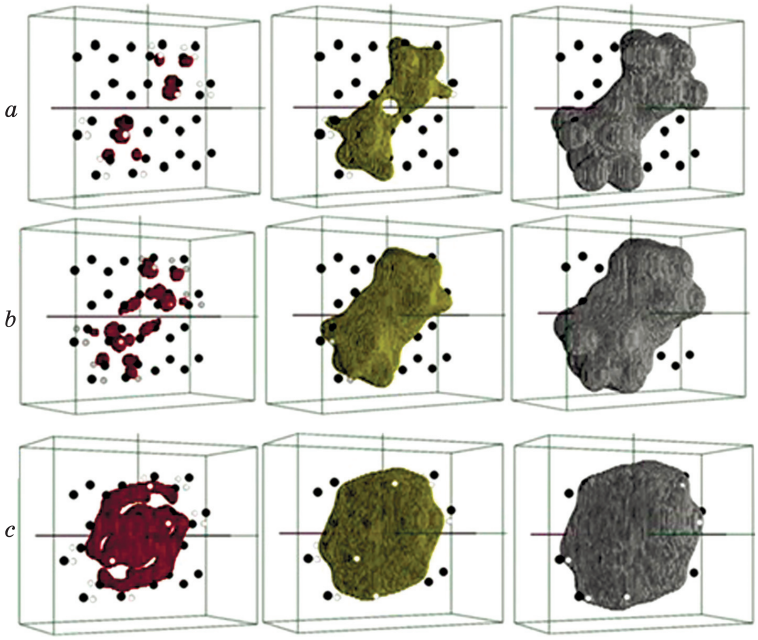

Fig. 7. Spatial distribution of valence electrons' density (from left to right for 0.9–1.0, 0.5–0.6, 0.1–0.2 definition of the maximum) in the structures with local chemical adsorption of graphene: (*a*) graphene/graphane, (*b*) graphene/fluorographene, (*c*) graphene/chlorographene [9]

Table 4. **Band gap values for objects 1–7**

Objects	Infinite objects		Finite objects	
	E_g, a.u.	E_g, eV	E_g, a.u.	E_g, eV
Object 1 (C)	0.00	0.00	0.07	1.90
Object 2 (CH)	0.14	3.81	0.11	2.99
Object 3 (CF)	0.01	0.27	0.03	0.82
Object 4 (CCl)	0.05	1.36	0.01	0.27
Object 5 (C/CH)	—	—	0.37	10.07
Object 6 (C/CF)	—	—	0.09	2.45
Object 7 (C/CCl)	—	—	0.38	10.34

the band gap of 10.34 eV; the structure of graphene/graphane has slightly smaller width of 10.07 eV; the structure of graphene/fluorographene has the smallest band gap of 2.45 eV.

The proposed combination of non-functionalized and functionalized areas of graphene in single structure leads to an increase in the band-gap width compared to the individual source objects.

3.2. Bending Strain Effect

Changes in the electronic properties of two-dimensional semi-metal graphene can also be achieved by bending deformation. In general, flexible electronics is burgeoning industry with a lot of promise. The facts that most of the 2*D* materials are mechanically stable make them as the natural choice for flexible electronics. It was experimentally demonstrated the thinnest, high performance, flexible, and transparent thin-film transistor fabricated using only two-dimensional layered materials for the first time [49]. Another flexible and transparent transistor based on two-dimensional materials was demonstrated by combining MoS_2 and graphene. The device exhibited extreme mechanical stability in terms of relatively small change in effective carrier mobility and threshold voltage as a function of the bending radius and number of bending cycles [50].

Graphene plays an important role for flexible electronics. This material affords the highest field-effect transistor mobilities, owing to its small effective mass. However, the lack of a band gap and the associated inability to switch off electrically precludes its use for digital transistors. Nevertheless, its high charge mobility and saturation velocity coupled with its intrinsic ambipolar character make it an attractive material for flexible RF analogue TFTs [51].

For extension of information about electronic properties of two-dimensional structures based on a local chemically functionalized graphene under bending strain effect, such objects are developed:

- object 1: 2*D* finite graphene/graphane structure with symbolic notation (C/CH); the primitive cell of the superlattice with parameters a = 13.23 Å, b = 10.58 Å, c = 9.53 Å; the basis consists of 48 atoms, among them 32 C atoms and 16 H atoms;

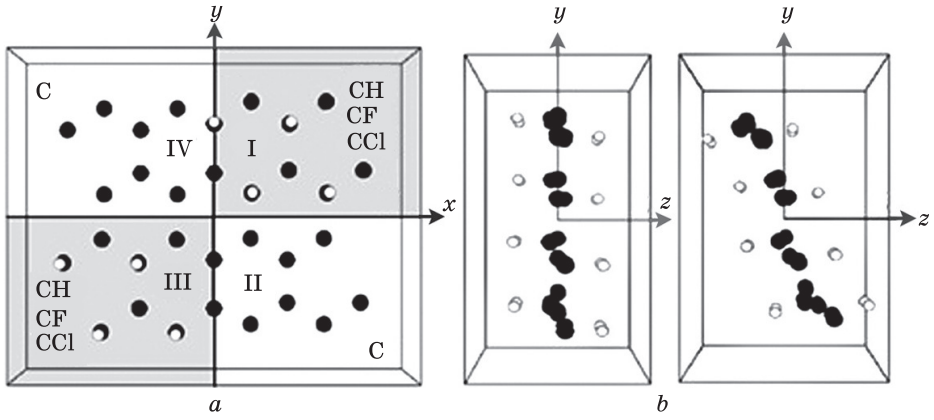

Fig. 8. (*a*) Primitive cells with atomic basis of graphene/graphane, graphene/fluorographene, graphene/chlorographene (view of the cell from the z axis); (*b*) view of the cell from the x axis (left $\alpha = 0°$, right $\alpha = 3°$) [12]

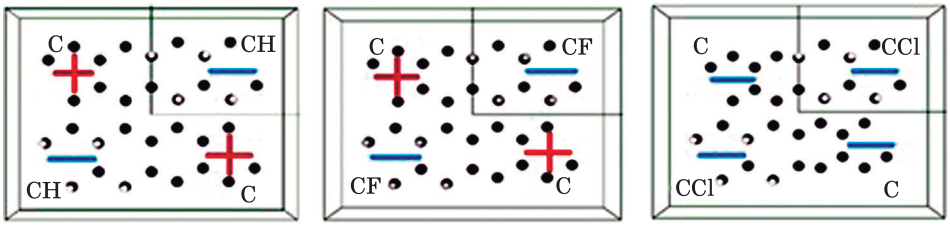

Fig. 9. Electric charge distribution for graphene/graphane (left), graphene/fluorographene (in the middle), and graphene/chlorographene (right) with chemical adsorption at α = 0°

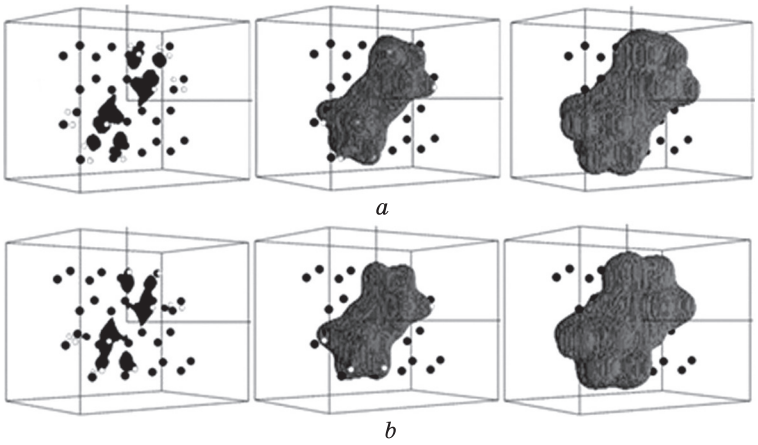

Fig. 10. Valence electron density spatial distribution in graphene/graphane depending on the bending strain (from left to right for 0.9–1.0, 0.5–0.6, and 0.1–0.2 definition of the maximum) for (*a*) α = 0° and (*b*) α = 3° [12]

• object 2: 2*D* finite graphene/fluorographene structure with symbolic notation (C/CF); the primitive cell of the superlattice with parameters a = 13.23 Å, b = 10.58 Å, c = 10.58 Å; the basis consists of 48 atoms, among them 32 C atoms and 16 F atoms;

• object 3: 2*D* finite graphene/chlorographene structure with symbolic notation (C/CCl); the primitive cell of the superlattice with parameters a = 13.76 Å, b = 11.64 Å, c = 10.58 Å; the basis consists of 48 atoms, among them 32 C atoms and 16 Cl atoms.

A primitive cell of a superlattice with an atomic basis of two-dimensional graphene/graphane, graphene/fluorographene, and graphene/chlorographene structures is demonstrated in Fig. 8, *a*. The bending strain effect that used in the research is consisted in bending the two-dimensional structure to the angle α (α = 0°, 1–5°). The atomic basis of the two-dimensional graphene/graphane structure for angles α = 0° and α = = 3° is shown in Fig. 8, *b* [12].

In the finite graphene/graphane, graphene/fluorographene, and graphene/chlorographene structures with local chemical functionalization, the charge distribution of valence electrons between non-functionalized and functionalized parts of structures and the bending strain effect is estimated. The point, around which the charge is calculated, is chosen in the centre of each section. The radius of the spherical volume is chosen to be the maximum according to the size of the section. Figure 9

Table 5. **Charge values in the regions of 2*D* structures depending on the bending strain [12]**

Structure	Angle α°	Quarters		Charge difference
		I, III	II, IV	
Graphene/ graphane	0	–27.86	10.73	38.59
	1	–27.49	10.62	38.11
	2	–30.05	10.58	40.63
	3	–31.97	10.48	42.45
	4	–29.85	2.27	32.12
	5	–27.81	2.11	29.92
Graphene/ fluorographene	0	–33.29	0.43	33.72
	1	–39.52	0.33	39.85
	2	–37.50	0.50	38.00
	3	–41.44	–3.71	37.73
	4	–39.60	–3.56	36.04
	5	–36.43	–7.62	28.81
Graphene/ chlorographene	0	–31.71	–16.26	15.45
	1	–31.77	–16.26	15.51
	2	–38.29	–20.53	17.76
	3	–41.38	–20.73	20.65
	4	–32.75	–20.59	12.16
	5	–30.43	–23.85	6.58

Table 6. **Band-gap width values for 2*D* structures depending on the bending strain (in different units)**

Angle α°	Structure					
	Graphene/graphane		Graphene/fluorographene		Graphene/chlorographene	
	E_g, a.u.	E_g, eV	E_g, a.u.	E_g, eV	E_g, a.u.	E_g, eV
0	1.33	36.18	0.91	24.75	0.48	13.06
1	1.55	42.16	0.57	15.50	0.61	16.59
2	0.85	23.12	0.73	19.86	0.05	1.36
3	0.59	16.05	0.46	12.51	0.14	3.81
4	0.24	6.53	0.18	4.90	0.12	3.26
5	1.16	31.55	0.41	11.15	0.15	4.08

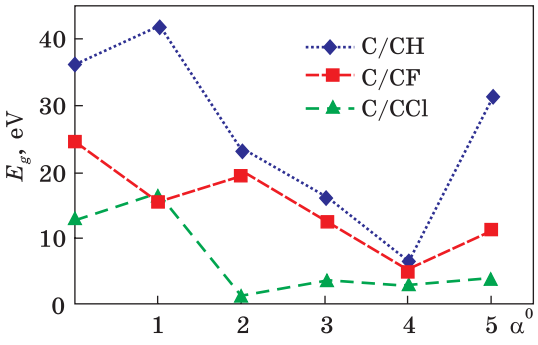

Fig. 11. Band gap width *vs.* the bending strain for C/CH, C/CF, and C/CCl structures [12]

shows the distribution of electric charge in two-dimensional structures at $\alpha = 0°$; the calculated values of charges for α from $\alpha = 0°$ to $\alpha = 5°$ are given in Table 5.

Redistribution of electric charge is observed with the formation of regions of different signs in the structures of graphene/graphane and graphene/fluorographene. The largest value of the charge difference is recorded in the graphene/graphane structure at the bending angle $\alpha = 3°$. In the structure of graphene/fluorographene, this difference is less noticeable; the largest value of the charge difference is achieved at the angle $\alpha = 1°$. In the structure of graphene/chlorographene, charge redistribution takes place, but without the formation of charge regions of different signs. Charge redistributions are illustrated by maps of the spatial distribution of valence electron densities for two-dimensional structures C/CH, C/CF, C/CCl (Fig. 10).

The values of the electronic band-gap width for two-dimensional structures, depending on the bending strain from $\alpha = 0°$ to $\alpha = 5°$, are given in Table 6 and in Fig. 11. For the graphene/graphane structure, the maximum value of the band gap is reached with bending at an angle $\alpha = 1°$. For the graphene/fluorographene structure, the bend provokes a decrease in the band gap compared to the flat structure. The largest value of the band gap for the graphene/chlorographene structure is recorded at a bending angle $\alpha = 1°$.

3.3. Effect of Static Pressure

Static pressure is another way to change the electronic properties of two-dimensional semi-metal graphene. For extension of information about electronic properties of two-dimensional structures based on local chemical functionalized graphene under effect of static pressure, a superlattice model is developed. It is an infinite periodic alternation of areas of graphene (graphane) non-functionalized and functionalized by hydrogen atoms. The primitive cell of the rhombic superlattice has the following parameters: $a = 9.96$ Å, $b = 8.82$ Å, $c = 5.29$ Å (Fig. 12). The atomic basis consists of 48 atoms, among them 32 C atoms and 16 H atoms. Details of the calculation are similar to those used in the previous two subsections [10].

Modelling of the reaction of atoms in two-dimensional graphene/graphane structure to the action of static pressure is carried out by

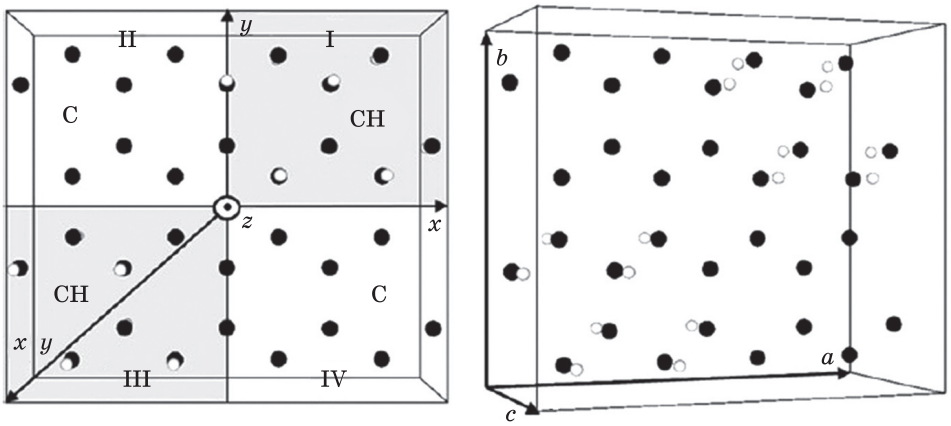

Fig. 12. Primitive cell of a superlattice with an atomic base of infinite graphene/graphane structure (top and side view) [11]

Table 7. **Values of forces (in [a.u.]) acting on the hydrogen atom at different pressure magnitudes [10]**

No. of H atom	Pressure values				
	0%	2.5%	5%	7.5%	10%
1	1.672	1.741	1.815	1.894	1.979
2	1.647	1.719	1.794	1.876	1.963
3	1.622	1.695	1.773	1.856	1.945
4	1.673	1.743	1.816	1.895	1.980
5	1.647	1.718	1.794	1.875	1.963
6	1.673	1.742	1.816	1.895	1.980
7	1.674	1.743	1.817	1.896	1.981
8	1.622	1.695	1.773	1.856	1.945
Average value	1.65	1.72	1.80	1.88	1.96

Table 8. Static pressure values (in different units) [10]

No.	Pressure, %	Pressure, a.u.	Pressure, $\times 10^{-9}$ H	No.	Pressure, %	Pressure, a.u.	Pressure, $\times 10^{-9}$ H
1	0	0	0	4	7.5	0.23	18.4
2	2.5	0.07	5.6	5	10	0.31	24.8
3	5	0.15	12.0				

changing the co-ordinates of the atomic basis that reflects the uniform compression from both surfaces of the structure. It is believed that the action of static pressure affects only the positions of the hydrogen atoms, which are part of graphane (CH), *i.e.*, their distance to the graphene framework. Five compression ratios are selected for comparison: (i) without compression (0%), the C–H distance is a_{CH} = 1.12 Å (CH);

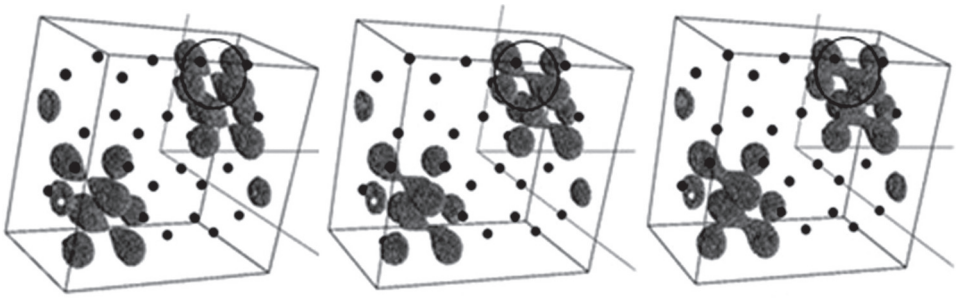

Fig. 13. Spatial distribution of valence electrons density (for 0.5–0.6 definition of the maximum) of graphene/graphane structure under static pressure effect [10]

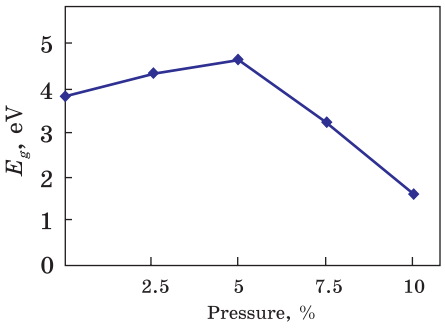

Fig. 14. Band gap width *vs*. the static pressure for graphene/graphane structure [10]

(ii) compression by 2.5%, the C–H distance is reduced by 2.5% from a_{CH} of graphane; (iii) compression by 5%; (iv) compression by 7.5%; (v) compression by 10%.

The magnitude of the pressure is estimated from the forces according to the formulas (40)–(42), which act on the hydrogen atoms from the rest of the cores and electrons' subsystem. Based on Newton's third law, it is obvious that these forces are the reactions equal in modulus but opposite in direction to the external influence of static pressure. As a result, the values of forces acting on each hydrogen atom are obtained when the corresponding pressure is applied (Table 7); they were then averaged over the atoms of the entire basis.

To estimate the pressure, the values of forces acting in the electron–core system in the absence of compression are subtracted from the obtained values of forces (Table 8). Recalculation of the pressure units with a.u. of forces (a.u.f.) into newtons (N) is carried out taking into

Table 9. **Band gap values of graphene/graphane structure under the static pressure effect (in different units) [10]**

No.	Pressure, %	E_g, a.u.	E_g, eV	No.	Pressure, %	E_g, a.u.	E_g, eV
1	0	0.14	3.81	4	7.5	0.12	3.27
2	2.5	0.16	4.35	5	10	0.06	1.63
3	5	0.17	4.63				

account that 1 N = 1 a.u.f. × $0.08 \cdot 10^{-6}$, which is obtained from the ratios of measurement units of the corresponding physical quantities.

Figure 13 shows maps of the spatial distribution of valence electron density under static pressure effect. Apparently, the change in pressure leads to the rearrangement of the electron 'clouds' of C–H covalent bonds, namely, to an increase in the valence electrons' density along these bonds.

The change in the band-gap width for the graphene/graphane structure at different pressure values is shown in the graph (Fig. 14). The numerical values of the band-gap width are given in Table 9. When the structure is compressed by 2.5% and 5%, an increase in the width of the band gap is recorded. With further compression of the structure by more than 5%, there is a significant reduction in the width of the band gap that indicates an increase in the conductive properties of such a structure [10].

3.4. Fluorination Effect

Recently, a new 2*D* counterpart of graphane, namely, hydrogenated fluorographene (CFH), was obtained by benign wet chemical synthesis. The authors emphasized its significant nonlinear optical properties; they revealed the importance of the nature of functional group and the degree of functionalization on the nonlinear optical properties of graphene sheets [52]. In turn, we decided to investigate the fluorination effect on electronic properties of two-dimensional local chemical adsorption structures, namely, graphene/graphane. The primitive cell of superlattice and atomic basis are chosen the same ones as in the previous subsection (see Fig. 12).

The modelling process of fluorination is carried out in pairs by replacing the atoms of hydrogen with fluorine atoms. The following structural configurations are numerically investigated: (i) C/CH without fluorine atoms (0% fluorination); (ii) C/CFH (32 C + 14 H + 2 F) with

Table 10. **Values of charges in the areas of C/CH and C/CFH structures under the fluorination effect [11]**

2*D* structure	Degree of fluorination	Structural configuration	Charge values		Charge difference
			I, III	II, IV	
C/CH	0	32C + 16H	–35.20	13.40	48.60
C/CFH	12.5	32C + 14H + 2F	–39.80	11.65	51.45
	25	32C + 12H + 4F	–39.38	10.76	50.14
	37.5	32C + 10H + 6F	–42.37	8.76	51.13
	50	32C + 8H + 8F	–48.26	6.06	54.32

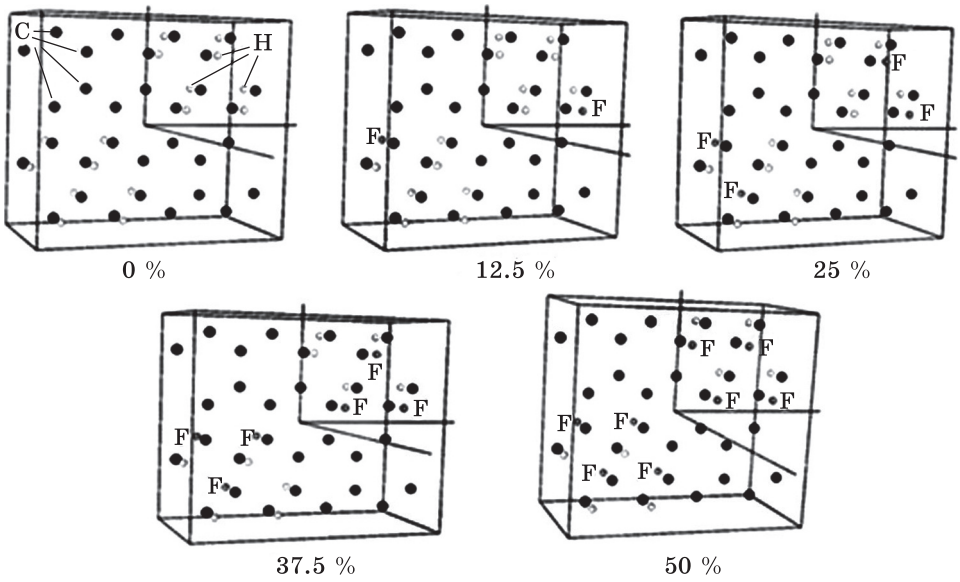

Fig. 15. Modelling the fluorination process of graphene/graphane structures [11]

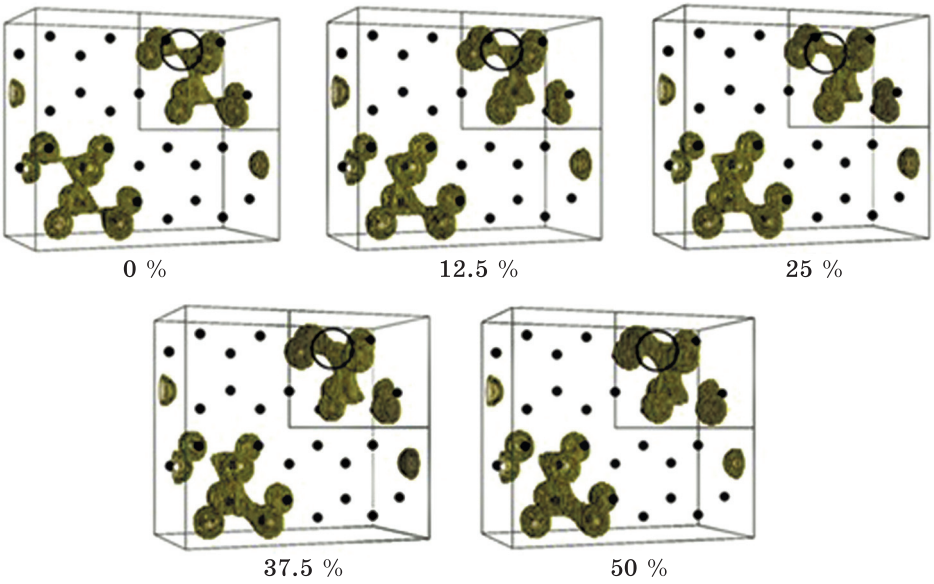

Fig. 16. Spatial distribution of valence electrons' density (for 0.5–0.6 definition of the maximum) of graphene/graphane structures under the fluorination effect [11]

2 F atoms (12.5% fluorination); (iii) C/CFH (32 C + 12 H + 4 F) with 4 F atoms (25% fluorination); (iv) C/CFH (32 C + 10 H +6 F) with 6 F atoms (37.5% fluorination); (v) C/CFH (32 C + 8 H + 8 F) with 8 F at-

Table 11. **Band gap values of C/CH and C/CFH structures under the fluorination effect [11]**

2*D* structure	Degree of fluorination	Structural configurations	E_g, a.u.	E_g, eV
C/CH	0	32C + 16H	0.14	3.81
C/CFH	12.5	32C + 14H + 2F	0.06	1.63
	25	32C + 12H + 4F	0.15	4.08
	37.5	32C + 10H + 6F	0.02	0.54
	50	32C + 8H + 8F	0.11	2.99

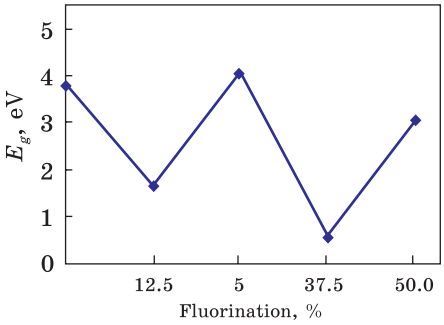

Fig. 17. Fluorination effect on the band gap width of graphene/graphane structure [11]

oms (50% fluorination) (Fig. 15). The percentage of fluorination is calculated by finding the proportion of fluorine atoms from the total number of hydrogen atoms [11].

In this case, the changes in the electronic properties of the two-dimensional C/CH and C/CFH structures are recorded. The charge values in the areas of these structures are calculated and are shown in Table 10. There is clear charge distribution with different signs on parts of C/CH structure. After the fluorination, there is a redistribution of charge with increasing charge difference. The highest value of charge redistribution is achieved with 50%-fluorination (32 C + 8 H + 8 F).

Numerical values of charges depending on the degree of fluorination are illustrated by maps of the spatial distribution of valence electron density for 2*D* structures C/CH and C/CFH, which are shown in Fig. 16. The fluorination effect enhances the covalent C–H bonds of functionalized graphene that is manifested in an increase in the intensity of the valence electron density along the bond directions (see the region bounded by the circle in Fig. 16).

The change of the band gap of two-dimensional structures C/CH and C/CFH under the fluorination effect is shown in the graph of Fig. 17. Numerical values of the band-gap width are given in Table 11.

Non-monotony in the change of the band-gap width values of two-dimensional C/CH and C/CFH structures under the fluorination effect is recorded. Non-monotony is oscillating that accordingly causes fluctuations in the electrical conductivity of the structure. Thus, the maximum value of the band gap is recorded at 25% fluorination; at 37.5% fluorination, the band-gap width reaches a minimum value. Therefore,

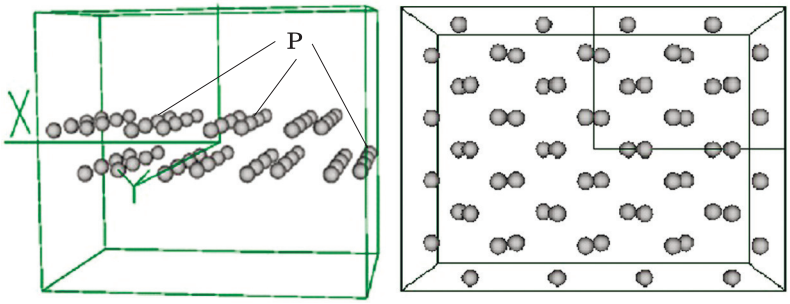

Fig. 18. Primitive cell of a superlattice with an atomic base of an infinite black phosphorene monolayer (side and top view) [13]

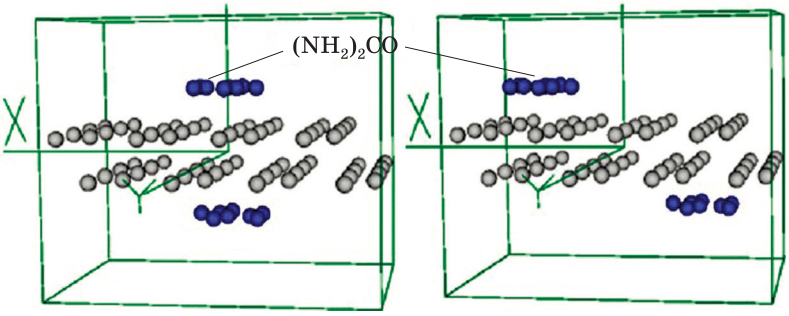

Fig. 19. Primitive cell of a superlattice with an atomic base of the infinite black phosphorene monolayer with adsorbed carbamide molecules for two types of localization: (left) 'one against each other' and (right) 'one offset each other' (displaced with respect to each other) [13]

by changing the degree of fluorination in the areas of two-dimensional C/CFH structures, it is possible to control their electrical-resistance properties [11].

3.5. Impurity Doping of Black Phosphorene

Molecule doping is a flexible and effective method towards modulating the electronic properties of two-dimensional materials [53]. Molecules adsorbed on the surface can influence electrotransport in the two-dimensional material, for example, by introducing doping effects, and a p–n junction can, thus, be fabricated by locally doping the material [54]. Authors of work [53] used benzyl viologen as an effective electron dopant to part of the area of a few-layer black phosphorus flake and achieved an ambient stable in-plane p–n junction. Such chemical doping with benzyl viologen molecules modulates the electron density and allows acquiring a large built-in potential in this in-plane black phosphorus p–n junction.

Black phosphorus constitutes a new class of 2D materials. It is intensively studied as a 2D semi-conductor [55–56575859]. Phosphorene,

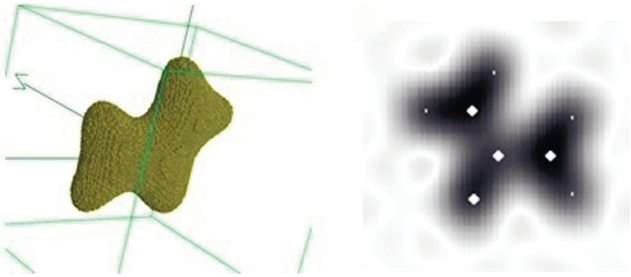

a *b*

Fig. 20. Valence electron density spatial distribution (for 0.5–0.6 definition of the maximum) of the carbamide molecule (*a*) and its cross-section (*b*) [13]

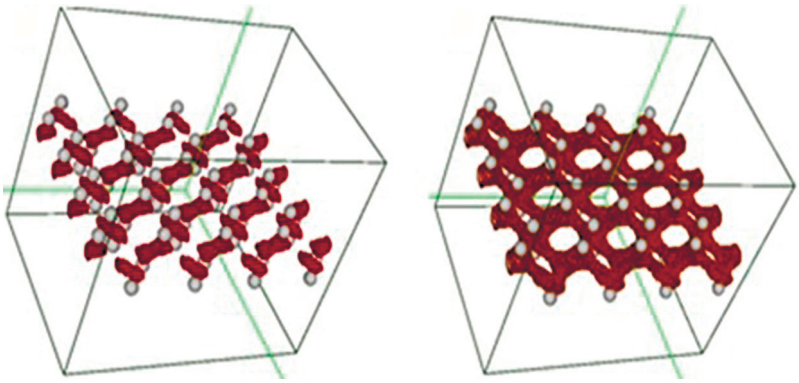

a *b*

Fig. 21. Spatial distribution of valence electrons' density (within the ranges 0.1–0.2 (*a*) and 0.2–0.3 (*b*) definition of the maximum) of the infinite black phosphorene monolayer [13]

as a phosphorus analogue of graphene, refers to the monolayer black phosphorus crystal [60]. The presence of an appreciable direct band gap and high carrier mobility makes phosphorene a promising candidate for novel semi-conductor applications [61]. The authors of [62] reported that the band gap of phosphorene is dependent on the number of layers and the in-layer strain, and is significantly larger than the bulk value.

For the study of electronic properties of the black phosphorene sheet with the impurity doping, the model of the superlattice is developed (Fig. 18). The rhombic primitive cell of the superlattice has the following parameters: a = 17.72 Å, b = 13.08 Å, c = 14.82 Å [13]. The geometric properties of primitive cell are such that it is convenient to use the Cartesian coordinate system. The dimensions of the primitive cell in the directions x and y are chosen so that the translation of cell organizes an infinite black phosphorene sheet. The size of the primitive cell in the direction z is chosen to avoid the interaction of atomic planes transmitted in this direction. The atomic basis contains 64 phosphorene atoms. The calculation is performed only for Γ-point of the *BZ* of superlattice.

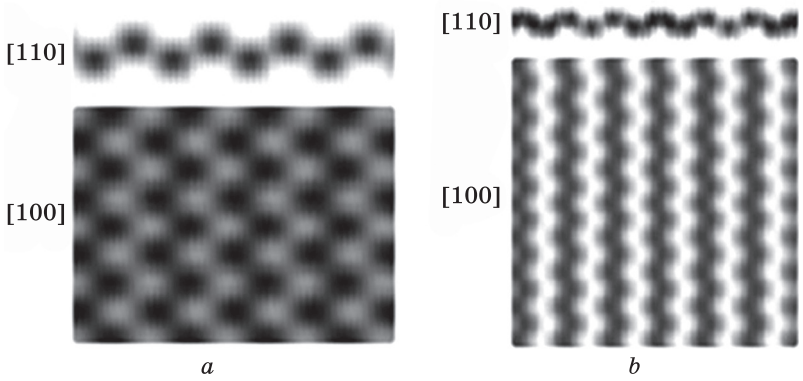

Fig. 22. Cross-sections of the infinite black phosphorene monolayer in the [110] and [100] planes within (*a*) one primitive cell and (*b*) several primitive cells [13]

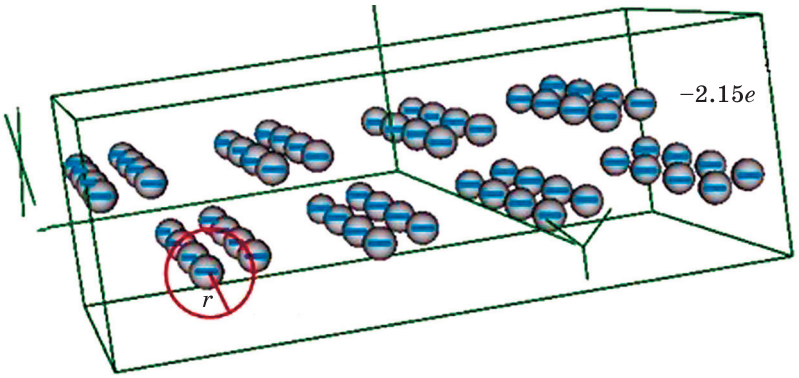

Fig. 23. Electric charge values on the cores of P atoms of the infinite black phosphorene monolayer within the spherical volume with radius $r = 1.32$ Å

Carbamide (urea) molecule $(NH_2)_2CO$ is selected for impurity doping of the black phosphorene sheet. It forms a colourless crystalline substance having a melting point of 132.7 °C. A primitive cell of a superlattice with an atomic basis for simulation of an infinite monolayer (which consists of two atomic layers) black phosphorene sheet with adsorbed carbamide molecules, placed on both black phosphorene sides either one against each other or one offset (displaced with respect to) each other, is represented in Fig. 19.

For comparison, several distances between the carbamide molecules and the black phosphorene sheet are chosen. These distances are changed from 1.87 Å (the smallest distance between atoms that equals the sum of covalent radius of phosphorene atom and molecule atoms) with subsequent increase up to 2.0 Å, 2.5 Å, and 3.0 Å.

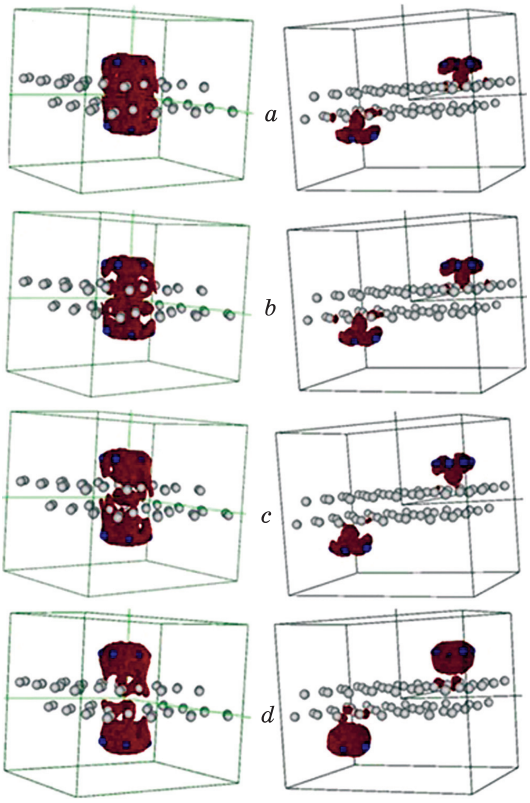

Fig. 24. Spatial distribution of valence electrons' density (in the 0.1–0.2 definition of the maximum) of an infinite black phosphorene monolayer with adsorbed carbamide molecules for the 'one against each other' (left) and 'one offset each other' (right) types of localization at different adsorption distances: (*a*) 1.87 Å, (*b*) 2.0 Å, (*c*) 2.5 Å, (*d*) 3.0 Å [13]

Figure 20 presents the spatial distribution of valence electrons' density of the carbamide molecule and its cross-sections. By means of concentration of valence electrons' density in the molecule plane, one can determine the intensity of the covalent bonds between the atoms within the molecule.

The spatial distribution of valence electrons' density of the black phosphorene sheet and its cross-sections are shown in Figs. 21 and 22.

In the sheet of black phosphorene, there is a homogeneous distribution of the valence electrons' density with charge of 2.15*e* on the phosphorene atoms' cores (Fig. 23). The electric charge is evaluated in a spherical volume with the radius r = 1.32 Å.

Table 12. **Values of charges on the black phosphorene atoms for the 'one against each other' type of localization [13] (see also Fig. 19)**

No. of the black phosphorene atom	1.87 Å	2.0 Å	2.5 Å	3.0 Å
22	–17.77	–17.63	–16.88	–15.47
23	–14.37	–14.10	–12.54	–10.09
26	–17.96	–17.86	–17.22	–15.84
28	–16.71	–16.49	–15.20	–13.34
37	–17.96	–17.86	–17.22	–15.84
39	–16.71	–16.49	–15.20	–13.34
41	–17.77	–17.63	–16.88	–15.47
44	–14.37	–14.10	–12.54	–10.09

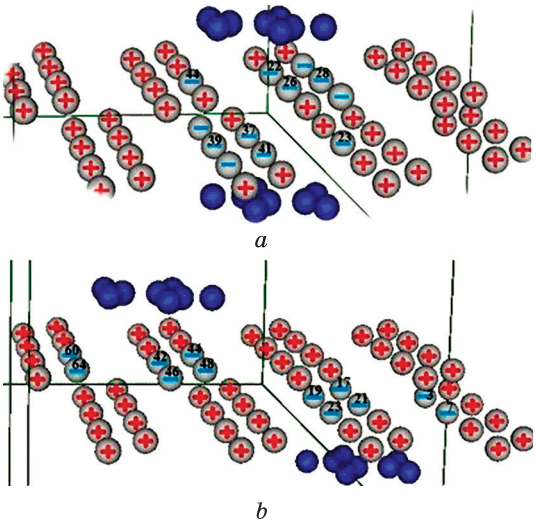

Fig. 25. Electric charges on the cores of P atoms of an infinite black phosphorene monolayer with carbamide admolecules for the (*a*) 'one against each other' and (*b*) 'one offset each other' types of localization [13]

Figure 24 depicts the maps of the spatial distribution of valence electrons' density of black phosphorene sheet with adsorbed carbamide molecules of 'one against each other' and 'one offset each other' localizations depending on the distance to the black phosphorene sheet. It is found that the adsorption of urea molecules by the monolayer of black phosphorene leads to a redistribution of the valence electrons' density in it. It is recorded that, in the black phosphorene sheet with adsorbed carbamide molecules of both types of localization, the charge regions of the highest density are located below the atoms of the carbamide molecules, creating a region of electron density of high concentration. The removal of the molecules leads to a decrease in their effect on the redistribution of the valence electrons' density in a black phosphorene sheet that is confirmed by the calculated electric charges on the black phosphorene atoms located directly under the molecules (Fig. 25). The values of the

Table 13. **The same as in the previous table, but for 'one offset each other' (*i.e.*, with a displacement) type of localization [13] (see also Fig. 19)**

No. of the black phosphorene atom	1.87 Å	2.0 Å	2.5 Å	3.0 Å
3	–9.47	–9.13	–7.69	–5.82
7	–5.68	–5.22	–3.51	–1.94
17	–10.83	–10.52	–8.81	–7.34
19	–14.99	–14.60	–12.98	–11.34
21	–17.30	–17.09	–16.29	–15.25
23	–8.17	–7.83	–6.41	–4.98
42	–17.30	–17.09	–16.29	–15.25
44	–8.17	–7.83	–6.41	–4.98
46	–10.83	–10.52	–8.81	–7.34
48	–14.99	–14.60	–12.98	–11.34
60	–5.68	–5.22	–3.51	–1.94
64	–9.47	–9.13	–7.69	–5.82

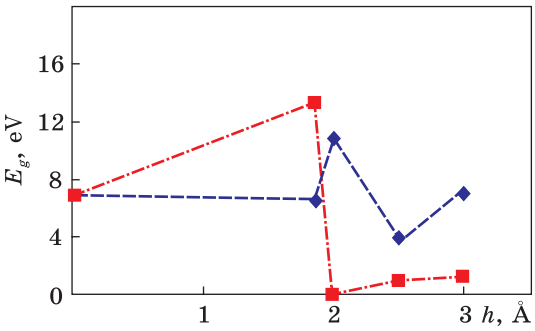

Fig. 26. Band gap widths of an infinite black phos-phorene monolayer with carbamide admolecules for the 'one against each other' (dash line) and 'one offset each other' (dash-dot line) types of localiza-tion at different adsorp-tion distances [13]

electric charge on the above-mentioned cores of the black phosphorene atoms at various adsorption distances for 'one against each other' and 'one offset each other' types of localization are given in Tables 12 and 13.

The accumulation of the electric charge of the black phosphorene sheet in the region under the carbamide molecules leads to redistribution of the electric charge in the monolayer and, sometimes, changes in the sign of the charges on the core of black phosphorene atoms to the opposite one. That is, the homogeneity of the distribution of electron density in the black phosphorene sheet (see Figs. 21–23) disappears and forms areas of electric charge of different signs (see Fig. 25). In this case, the negative sign of the electric charge in the vicinities of the cores of black phosphorene atoms located directly below the molecules is maintained with a significant increase in the modulus of charge. Whereas, the sign of the electric charges in the vicinity of the cores of black phosphorene atoms away from the adsorbed molecules changes to the opposite one. Such charge redistributions indicate the possibility of creating a built-in two-dimensional p–n junction in the sheets of black phosphorene with impurity doping with carbamide molecules.

Table 14. **Values of the band gap width of an infinite black phosphorene monolayer with adsorbed carbamide molecules for the 'one against each other' and 'one offset each other' types of localization [13]**

Adsorption distance l, Å	Type of localization			
	'one against each other'		'one offset each other'	
	E_g, a.u.	E_g, eV	E_g, a.u.	E_g, eV
1.87	0.24	6.53	0.49	13.33
2.0	0.40	10.88	0.004	0.10
2.5	0.14	3.81	0.03	0.82
3.0	0.26	7.07	0.04	1.09

Table 14 and graphs in Fig. 26 show the obtained values of the band gap for the infinite black phosphorene monolayer with adsorbed carbamide molecules for the 'one against each other' and 'one offset each other' types of localization. There is a non-monotony nature of the change in the band gap with a change in the adsorption distance that is more pronounced for adsorption of the 'one against each other' type. The displacement of the boundaries of the conduction bands and the valence band relative to the corresponding values for pure black phosphorene is significant for adsorption on the type 'one against each other'. The band-gap values are significantly reduced for 'one offset each other' adsorption type for all calculated distances. Thus, for the 'one against each other' type of localization with an adsorption distance of 2.0 Å, an increase in the band gap of the infinite black phosphorene monolayer to almost 11 eV is observed, compared to 6.8 eV for the pure monolayer. Whereas for the type of localization 'one offset each other' at the same adsorption distance, there is a noticeable reduction in the band gap to 0.1 eV. Therefore, the adsorption of carbamide molecules on the black phosphorene monolayer changes its conductivity, which can be controlled by controlling the localization of the adsorbed molecules [13].

4. Straintronics and Defect Engineering in Graphene

The pristine (*i.e.*, defect-free) and structurally perfect graphene exhibits outstanding electronic properties such as ballistic electron propagation with extremely high charge carrier mobility [6] or quantum Hall effect at a room temperature [63]. However, one of the challenges for graphene to be extensively used in the mass production of electronic devices [64] and in the bioengineering [65] is either an absence of the sufficient band gap in its electronic spectrum or problem with the gap modulation. Current–voltage behaviour of graphene is symmetrical with respect to the zero-voltage point and thereby does not allow switching of graphene-based transistors with a high on–off ratio. There are several ways for engineering a band gap in graphene. They are cutting graphene into nanoribbons [66] or nanomeshes [67], applying perpendicular magnetic field to bilayer graphene [68], surface adsorption or/and introducing specific defects [69, 70], using substrate [71, 72], configuring (ordering [73–78]) of impurity (adsorbed either substitutional or interstitial) atoms [79–83], applying different strains such as uniaxial tensile [84–88] and shear [89, 90] deformations or their combination [91].

Among many remarkable features of graphene, its mechanical properties are miraculous. Graphene is the strongest material ever tested with an intrinsic tensile strength of ≈130 GPa, Young's modulus (stiffness) of ≈1 TPa [92] and even increases with the density of defects [93]. Graphene sheet can sustain reversible (elastic) deformations up to about ≈25–27% [92, 94, 95]. Deformations (stresses) can arise naturally in

graphene or/and be intentionally induced and controlled via different techniques [96, 97]. Above-mentioned mechanical characteristics indicate that the strain yields an interesting possibility for tuning graphene's properties and that is why even opens a new research field, which some authors already called as 'straintronics', *i.e.*, strain (mechanical, deformation) electronics or strain engineering [96–98].

The disagreements in the literature [84–91, 99–103] regarding the fingerprints of different types of deformation (*e.g.*, uniaxial, (non)isotropic biaxial, shear, local strains, *etc.*) in graphene's electronic structure, particularly in the possible band-gap opening, are reviewed in [104–106], while the discrepancies [107–111] concerning the stability of differently (randomly, correlatively, or orderly) distributed adsorbed atoms on graphene surface are reviewed in [105–113]. The presence of both types of contradictions is not surprising inasmuch as two reasons. First, the 'straintronics' (strain electronics) only opens its evolution [97]. Second, in overwhelming majority of theoretical and computational studies of the strained graphene, the size of graphene computational domains are mostly limited to periodic supercells and localized fragments containing a relatively small number (usually some hundreds) of atoms (sites). These restrictions are caused by the commonly used first-principles density-functional calculations requiring high computational capabilities. The summarized discrepancies dealing with deformation effect (see Ref. [104]) concern results for even perfect graphene without any structural defects and external magnetic fields. However, fabricated graphene samples actually contain different point and/or extended defects [114] that can strongly affect electronic and even mechanical properties of graphene [115–117].

As known, the strains modify distances between ions in graphene-lattice sites and can be described by a vector potential, which is analogous to that of the external magnetic field [96, 118]. Therefore, an impact of different nonuniform strains on electronic properties of graphene is frequently associated in the literature (see, *e.g.*, [119, 120]) with an influence of the effective pseudo-magnetic field. Nevertheless, such a field differs from the real magnetic field by the opposite directions in the two inequivalent (Dirac) high-symmetry points K and K' within the 1st *BZ* of the reciprocal space.

Among various types of structural (point [121–126] or extended [127–130]) defects [131] in the physics of graphene, adsorbed atoms or molecules are probably the most important examples [132]. Acting as lattice imperfections, such defects govern many characteristics, such as electron states, electrical conductivity, degree of localization of electrons (and their spins) [114], and therefore strongly affect electronic, transport, optical, thermal, mechanical, and electrochemical [112, 133–135] properties of graphene. Distributions of impurity (adsorbed) atoms

over the graphene-lattice (adsorption) sites or interstices are not always random, as it usually takes place for three-dimensional metals and alloys, where adatoms are introduced *via* the alloying, which is generically a random process [136]. Diluted atoms may have a tendency towards the spatial correlation [137] or even ordering [138–142]. Moreover, graphene is an open surface, therefore (ad)atoms can be positioned onto it with the use of scanning tunnelling [143] or transmission electron [144] microscopes allowing to design (ad)atomic configurations as well as ordered (super)structures with atomic precision. Several ordered configurations of hydrogen adatoms on graphene have been directly observed [145] using the scanning tunnelling microscope.

Above-mentioned inconsistencies (regarding the stability of randomly-, correlatively-, or orderly-distributed adatoms on graphene surface [107–111] and the impact of strain on electronic properties of even defect-free graphene [84–91, 99–103]) contributed to the motivation of this study. Note that realistic graphene samples contain different structural defects, particularly, due to the peculiarities of the fabrication technology.

4.1. Theoretical Grounds for Electron Diffusivity and Conductivity

Within the framework of Kubo–Greenwood formalism (see, *e.g.*, [146]), the energy (E) and time (t) dependent diffusivity (commonly known in the literature as an electron diffusion coefficient) is defined as [147, 148]

$$D(E,t) = t^{-1}\,\Delta\langle\hat{X}^2(E,t)\rangle, \tag{44}$$

where the wave-packet mean-quadratic spreading (propagation) along the spatial x-direction is [147, 148]

$$\langle\Delta X^2(E,t)\rangle = \frac{\mathrm{Tr}[(\hat{X}(t)-\hat{X}(0))^2\,\delta(E-\hat{H})]}{\mathrm{Tr}[\delta(E-\hat{H})]} \tag{45}$$

with $\hat{X}(t) = \hat{U}^{\dagger}(t)\hat{X}\hat{U}(t)$ being the position operator in the Heisenberg representation, $\hat{U}(t) = \exp(-i\,\hat{H}t/\hbar)$ is a time-evolution operator, and tight-binding Hamiltonian $\hat{H}$ with hopping integrals up to the first three coordination shells (spheres) defines the Bernal-stacked few-layer honeycomb lattice [149, 150],

$$\hat{H} = \sum_{l=1}^{N_{\mathrm{layer}}}\hat{H}_l + \sum_{l=1}^{N_{\mathrm{layer}}-1}\hat{H}_l', \qquad H = \sum_{l=1}^{N_{\mathrm{layer}}}\hat{H}_l + \sum_{l=1}^{N_{\mathrm{layer}}-1}\hat{H}_l', \tag{46}$$

where N_{layer} is a number of layers, $\hat{H}_l$ is a Hamiltonian contribution of l-th layer, and $\hat{H}_l'$ describes hopping parameters between neighbour layers (vanishes in case of one layer), *i.e.*,

$$\hat{H} = -\gamma_0^1\sum_{\langle i,j\rangle}c_i^{\dagger}c_j - \gamma_0^2\sum_{\langle\langle i,j\rangle\rangle}c_i^{\dagger}c_j - \gamma_0^3\sum_{\langle\langle\langle i,j\rangle\rangle\rangle}c_i^{\dagger}c_j + \sum_i V_i c_i^{\dagger}c_i; \tag{47}$$

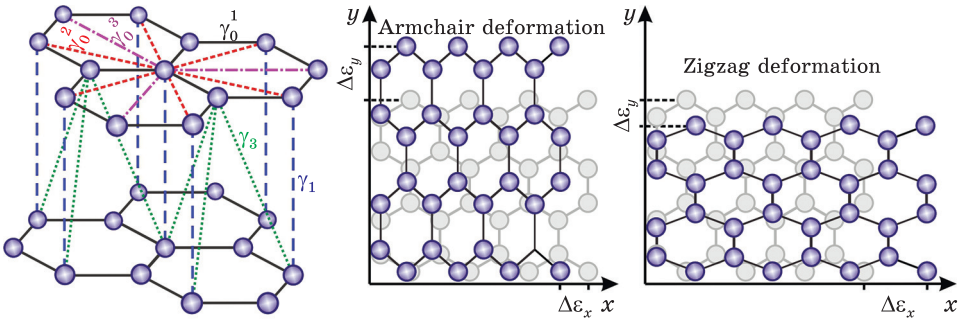

a *b* *c*

Fig. 27. Intralayer (γ_0^1, γ_0^2, γ_0^3) and interlayer (γ_1, γ_3) hopping parameters for two layers (*AB*) of Bernal-stacked multilayer graphene (*a*). Two types of uniaxial tensile strain (by ≈30%) along armchair- (*b*) or zigzag-type (*c*) edges for single graphene layer [104]

here, the creation (annihilation) operator $c_i^\dagger(c_i)$ acts on a quasi-particle located at a site $i = (m, n)$, where m and n are numbers of each i-th site along zigzag edge (x-direction) and armchair edge (y-direction), respectively, as shown in Fig. 27. The summation over i runs the entire honeycomb lattice, while j is restricted to the nearest-neighbours (in the first term), next nearest-neighbours (second term), and next-to-next nearest-neighbours (third term) of i-th site. The parameter $\gamma_0^1 = 2.78$ eV [64] is an inlayer hopping for the nearest-neighbouring carbon atoms occupying i-th and j-th sites at a lattice-parameter distance $a_0 = 0.142$ nm between them [149, 150] (a_0 is an unstrained graphene lattice parameter). Parameters $\gamma_0^2 = 0.085\gamma_0^1$ and $\gamma_0^3 = 0.034\gamma_0^1$ are intralayer hoppings for next (second) and next-to-next (third) nearest-neighbour sites at the second and third coordination shells, respectively [87] (see Fig. 27, *a*). The on-site potential V_i defines the defect strength at a given graphene-lattice site i due to the presence of different defects (often identifying in graphene literature with the sources of disorder) [149, 150].

The interlayer interactions can be described using the standard Slonczewski–Weiss–McClure (SWM) model of electronic states in graphite [151–153]:

$$\hat{H}_l' = -\gamma_1 \sum_j (a_{l,j}^\dagger b_{l+1,j} + \text{H.c.}) - \gamma_3 \sum_{j,j'} (b_{l,j}^\dagger a_{l+1,j'} + \text{H.c.}) \qquad (48)$$

with $\gamma_1 = 0.12\gamma_0^1$, $\gamma_3 = 0.1\gamma_0^1$ [150] defining the interlayer-hopping amplitudes, *i.e.*, the strength of the interlayer coupling (Fig. 27, *a*). To simplify calculation procedure and enhance the computation speed, other SWM tight-binding parameters are omitted.

The dc conductivity σ can be extracted from the electron diffusivity $D(E,t)$, when it saturates reaching the maximum in a diffusive electron transport regime,

$$\lim_{t\to\infty} D(E,t) = D_{\max}(E),$$

and the semi-classical dc conductivity at a zero temperature is defined as [154, 155]

$$\sigma \equiv \sigma_{xx} = e^2 \rho_0(E) D_{\max}(E), \tag{49}$$

$-e < 0$ denotes the electron charge, and $\rho_0(E) = \rho/S = \mathrm{Tr}[\delta(E - \hat{H})]/S$ is the density of electronic sates (DOS) per unit area S (and per spin). We can use the DOS to calculate the electron density:

$$n_e(E) = \int_{-\infty}^{E} \rho_0(E)\, dE - n_{\text{ions}},$$

where $n_{\text{ions}} = 3.9 \cdot 10^{15}$ cm^{-2} is density of positive ions compensating the negative charge of p-electrons in graphene. For the defect-free graphene, at a neutrality (Dirac) point, $n_e(E) = 0$. Combining calculated $n_e(E)$ with $\sigma(E)$, we can compute the density-dependent conductivity $\sigma = \sigma(n_e)$.

The computational methodology utilized for numerical calculation of the density of states (DOS), electron diffusivity ($D(E,t)$), and conductivity (σ) is described in Ref. [156] (particularly, see appendix therein for details). This methodology includes the Chebyshov method for solution of the time-dependent Schrödinger equation, calculation of the first diagonal element of the Green's function using continued fraction technique and tridiagonalization procedure of the Hamiltonian matrix, averaging over realizations of impurity (ad)atoms, sizes of initial wave packet and computational domain, boundary conditions, *etc*.

4.2. Modelling Approach or Structural Deformations and Defects

Let us consider two orthogonally related directions for uniaxial tensile strain in graphene lattice: along so-called armchair (Fig. 27, *b*) and zigzag (Fig. 27, *c*) directions (edges). For these mutually transverse directions (as well as for any other one), the uniaxial strain induces lattice deformation: changes bond lengths and, therefore, hopping parameters between different sites. Generally, hopping parameters can be different among different neighbouring sites. However, in case of a homogeneous elastic tensile deformation, though hoppings from a given site to its neighbours can be all different, they should be the same for every such site. Therefore, model Hamiltonian contains only three distinct hoppings, and our goal turns to investigation of the changes that strain induces in these hoppings and impacts electronic structure. Following [86–88, 157, 158], where random strain is modelled by the Gaussian function, we can obtain dependence of the bond lengths on the deformation tensor components and then relate hopping parameters of the

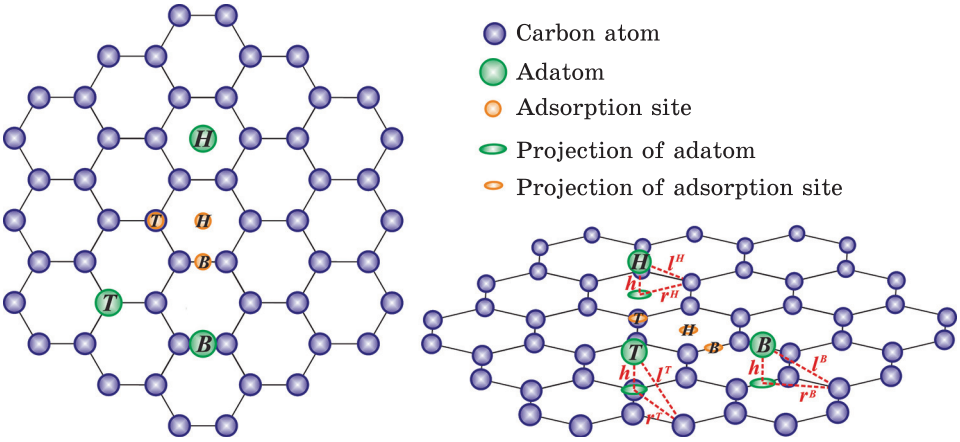

Fig. 28. Typical configurations of adatom–graphene system [112]: top (left) and perspective (right) views of graphene lattice with hollow centre (*H*), bridge centre (*B*), and (a)top (*T*) adsorption sites

strained, γ, and unstrained, γ_0^1, graphene *via* exponential decay

$$\gamma(l) = \gamma_0^1 \exp\left(-\beta\left(\frac{l}{a_0} - 1\right)\right) \tag{50}$$

with the strained bond length l, the decay rate $\beta \approx 3.37$ [86, 87] extracted from experimental data [159], and the Poisson's ratio $\nu = 0.15$ selected between that measured for graphite [160] and calculated for graphene [161].

The disorder in graphenelike lattice can be represented by different types of (zero-dimensional and one-dimensional) defects. They can be modelled *via* the above-mentioned (in Eq. (47)) on-site potential V_i modifying the Hamiltonian matrix central diagonal. Below, we present models can be used to describe different types of defects.

Manifestly short-range (weak or strong) impurities, represented as neutral adatoms, occupying different types of adsorption sites over the honeycomb lattice as shown in Fig. 28, or chemisorbed molecules (*e.g.*, hydroxyl, methyl, nitrophenyl functional groups [162]) covalently bound to carbon atoms, can be modelled by the delta-function potential [149, 156, 163]

$$V_i \equiv V_i^{\delta} = \sum_{j=1}^{N_{\text{imp}}^{\delta}} V_j^{\delta} \delta_{ij} \tag{51}$$

for each i-th site of the honeycomb lattice where N_{imp}^{δ} δ-like impurities occupy j-th sites. This potential acts as a weak or strong depending on weak, $V_j^{\delta} = V_0 \leq |\gamma_0^1|$, or strong, $V_j^{\delta} = V_0 \gg |\gamma_0^1|$, scattering of charge carriers (electrons). The *ab initio* and T-matrix approach based calculations for strong impurity adatoms provide typical estimated values for the

on-site potential $V_j^{\delta} = V_0 \leq 80|\gamma_0^1|$ [164–167], *e.g.*, for so-called resonant impurities [149] (CH_3, C_2H_5OH, CH_2OH as well as hydroxyl groups), $V_0 \approx 60|\gamma_0^1|$. In case of a strong scattering regime, occurring for resonant impurities (RI), studied in Ref. [156], the on-site potential was assumed to be $V_0 \equiv V^{\mathrm{RI}} = 37|\gamma_0^1| \approx 100$ eV.

There is another way for modelling N_{imp} resonant impurities through the Hamiltonian part [149]

$$\hat{H}_{\mathrm{imp}} = \epsilon_d \sum_i^{N_{\mathrm{imp}}} d_i^{\dagger} d_i + V \sum_i^{N_{\mathrm{imp}}} \left(d_i^{\dagger} c_i + \mathrm{H.c.} \right) \tag{52}$$

with parameters $V \approx 2\gamma_0^1$ and $\epsilon_d \approx -\gamma_0^1/16$ obtained from density-functional theory calculations [165]. Resonant impurities behave themselves similarly to the vacancies because of completely electron localization at an impurity site. The distinction of influence of vacancies on electronic structure from the effect of the resonant impurities is strong zero energy modes [149, 150, 168]. A vacancy can be regarded as a site with hopping parameters to other sites being zero, though another way to model vacancy at the site i is $V_i \to \infty$ [149, 150]. In our simulations, we implement a vacancy removing the atom at a vacancy site.

Screened charged impurity ions, adatoms (Fig. 28) or admolecules, on graphene or its dielectric substrate are commonly described in the literature *via* Gaussian-type on-site scattering potential [149, 150]

$$V_i \equiv V_i^{\mathrm{Gauss}} = \sum_{j=1}^{N_{\mathrm{imp}}^{\mathrm{Gauss}}} U_j^{\mathrm{Gauss}} \exp\left(-\frac{|\mathbf{r}_i - \mathbf{r}_j|^2}{2\xi^2} \right), \tag{53}$$

where $N_{\mathrm{imp}}^{\mathrm{Gauss}}$ Gaussian impurities reside j sites with radius-vectors $\mathbf{r}_j$, ξ is interpreted as an effective potential radius, and the potential height U_j^{Gauss} is uniformly distributed within the range $[-\Delta_{\mathrm{imp}}^{\mathrm{Gauss}}, \Delta_{\mathrm{imp}}^{\mathrm{Gauss}}]$ with $\Delta_{\mathrm{imp}}^{\mathrm{Gauss}} = |\gamma_0^1|$ as a maximal potential height. Depending on effective potential radius ξ, potential (53) can manifest both short-range (where the range is smaller than the lattice constant) and long-range (where the range is comparable or slightly larger than the lattice constant but still much smaller than the typical electron wavelength) features. Varying these parameters allows consideration of two types of such impurities: with short-range (*e.g.*, for $\xi = 0.65a$ and $\Delta = 3\gamma_0^1$) and (rather) long-range (*e.g.*, for $\xi = 5a_0$ and $\Delta = \gamma_0^1$) action.

Another way to introduce scattering on the charged impurities is use of the Coulomb-type potential. For instance, in case of adatoms, randomly distributed above the honeycomb-lattice centres j (Fig. 28) or located at the substrate, the Coulomb on-site (i) potential reads as [163]

$$V_i \equiv V_i^{\mathrm{Coulomb}} = \sum_{j=1}^{N_{\mathrm{imp}}^{\mathrm{Coulomb}}} \pm \frac{e^2}{4\pi\epsilon_0\epsilon\,|\,\mathbf{r}_i - \mathbf{r}_j|} \tag{54}$$

with $\mathbf{r}_i$ ($\mathbf{r}_j$) radius-vector for i-th site (j-th hexagon), vacuum permittivity ϵ_0, and substrate dielectric constant ϵ. In case of adatomic location, *e.g.*, at SiO_2 substrate on the distance of $\approx(2-3)a_0$ [169] from graphene layer, dielectric constant $\epsilon = 3.9$ that enables to take into account the screening effect. In case of other substrates (*e.g.*, hexagonal boron nitride [163]), another value of dielectric constant slightly changes results quantitatively, but not qualitatively. Depending on the sign (±), there are three types of $N_{\text{imp}}^{\text{Coulomb}}$ Coulomb impurities [163]: (i) randomly distributed positive and negative charges (±) with electric neutrality of the whole sample, (ii) only positive (+) and (iii) only negative (–) impurities. However, we consider positive–negative impurities (cases (i)) and positive only impurities (case (ii)). Case (iii) results to DOS curves analogous to case (ii) but with opposite asymmetry with respect to the Dirac point. Varying parameters entered into the scattering potentials (53) and (54), they may be also adopted for modelling so-called mixed (hetero) doping, *e.g.* observed co-doping with boron and silicon atoms [170].

One more type of defects is so-called Gaussian hopping [150, 163]. Usually, they originate from the substitutional impurities causing the atomic-size misfit effect as local in-plane or out-of-plane displacements of atoms, and short- or long-range distortions in graphene lattice due to the curved ripples or wrinkles. The modified distribution of the hopping integrals between different (i, j) sites reads as [150, 163]

$$\gamma_{i,j} = \gamma + \sum_{k=1}^{N_{\text{hop}}^{\gamma}} U_k^{\gamma} \exp\left(\frac{-\left|\mathbf{r}_i - \mathbf{r}_j - 2\mathbf{r}_k\right|^2}{8\xi_{\gamma}^2}\right) \tag{55}$$

with N_{hop}^{γ} (Gaussian) straining centres at $\mathbf{r}_k$ positions, ξ_{γ} is an effective potential length, and hopping amplitude $U_k^{\gamma} \in [-\Delta_{\gamma}, \Delta_{\gamma}]$. The distortion centres can be considered with shortly ($\xi_{\gamma} = 0.65a_0$, $\Delta\gamma = 1.5\gamma_0^1$) or more distantly acting ($\xi_{\gamma} = 5a_0$, $\Delta\gamma = 0.5\gamma_0^1$) hoppings. The summation in expressions for Gaussian impurities and hoppings is commonly restricted to the sites belonging to the same layer, *i.e.*, possibility for the overlapping of Gaussian distributions in different layers is usually omitted [104, 150, 163].

Finally, extended (line-acting) defects are present in epitaxial graphene, where they comprise atomic terraces and steps [171, 172], and polycrystalline chemically-vapour-deposited (CVD) graphene as the grain boundaries [173–174175] or quasi-periodic nanoripples (wrinkles) [176, 177]. The effective potential for N_{lines} charged lines could be derived within the Thomas–Fermi approximation [178] and can be very well fitted by the Lorentzian-shaped function [179, 180]:

$$V_i \equiv V_i^{\text{Lorentz}} = \sum_{j=1}^{N_{\text{lines}}} U_j^{\text{Lorentz}} \frac{A}{B + Cr_{ij}^2}, \tag{56}$$

where r_{ij} is a distance between the i-th site and j-th line. Fitting para-

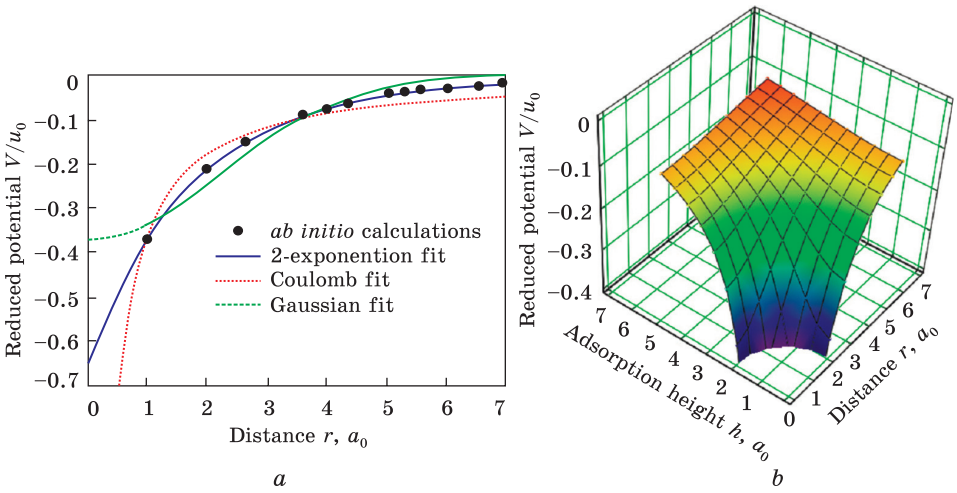

Fig. 29. Scattering potential for potassium (K) adatoms on the fixed adsorption height h = 2.4 Å (*a*) and for K adatoms with varying h (*b*). *Ab initio* calculations (•) [184] are fitted *via* the Gaussian potential $V = Ue^{-r^2/2\xi^2}$ (fitting parameters $U = -0.37\gamma_0^1$ and $\xi = 2.21a$ define the potential height and effective potential radius, respectively), the Coulomb potential $V = Q/r$ ($Q = -0.36\ \gamma_0^1 a$), and two-exponential function $V = U_1 e^{-r/\xi_1} + U_2 e^{-r/\xi_2}$ ($U_1 = -0.45\gamma_0^1$, $\xi_1 = 1.47a$, $U_2 = -0.20\gamma_0^1$, $\xi_2 = 2.73a$), where r is a distance from the projection of adsorbed atom to the lattice site [112]

meters A, B, and C depend weakly on electron density; they are calculated in Refs. [179, 180]: $A = 1.544$, $B = 0.78$, and $C = 0.046$. The potential height U_j^{Lorentz} is commonly chosen randomly in the range $[-\Delta^{\text{Lorentz}}, \Delta^{\text{Lorentz}}]$ or $[0, \Delta^{\text{Lorentz}}]$ with potential strength (maximum potential height) $\Delta^{\text{Lorentz}} = 0.25|\gamma_0^1| = 0.675$ eV close to the values of the contact potential variation at the substrate atomic steps observed in epitaxially-grown graphene *via* the Kelvin probe force microscopy [181–182183].

Depending on the range $[-\Delta^{\text{Lorentz}}, \Delta^{\text{Lorentz}}] \ni U_j^{\text{Lorentz}}$ or the range $[0, \Delta^{\text{Lorentz}}] \ni U_j^{\text{Lorentz}}$, we consider (alternating) symmetric (sign-changing, $V \gtrless 0$, *i.e.* attractive–repulsive) or asymmetric (constant-sign, $V > 0$, *i.e.* repulsive for electrons) scattering potential. In contrast to the Gaussian potential (53), which is not strongly long-range even for a large effective potential radius (ξ), the Lorentzian one (56), as well as Coulomb potential (54), is definitely a long-range potential.

However, sometimes Gaussian (and even Coulomb) scattering potentials are not the most appropriate to describe scattering by various (specific) point defects as Fig. 29, *a* demonstrates [112]. Therefore, sometimes it is more adequately to use scattering potential adapted from the independent self-consistent *ab initio* calculations [184], as it has been realized for potassium adatoms on the height $h \cong 2.4$ Å over

the graphene surface: Fig. 29, *a*. Transforming the scattering potential $V = V(r)$ into its dependence on a distance from the lattice site directly to adatom, $V = V(l)$, where $l = r^2 + h^2$ as demonstrably from Fig. 29, one can obtain its dependence on both r and h, $V = V(r, h)$, which is plotted in Fig. 29, *b*.

At a correlation (short-range order), impurities are no longer considered to be randomly located. To describe their spatial correlation, it is conveniently to introduce a pair distribution function $p(\mathbf{R}_i - \mathbf{R}_j) \equiv p(r)$ [185, 186]: $p(r) = 0$ for $r < r_0$, $p(r) = 1$ for $r \geq r_0$, where $r = |\mathbf{R}_i - \mathbf{R}_j|$ is a distance between the two adatoms, and a correlation length r_0 defines minimal distance that can separate any two of them. If adatoms are randomly distributed, then, $r_0 = 0$. The maximal correlation length $r_{0\max}$ depends on both relative concentration of impurities as well as their (adsorption) positions (as substitutional or interstitial) [112]. For a pronounced correlation effect, it is better to choose maximal possible correlation length, as for $n_K = 3.125\%$ of correlated potassium adatoms in [112], where correlation length was selected as $r_0 = r_{0\max} = 7a_0$ for hollow- (*H*) and bridge-type (*B*) sites, and $r_0 = r_{0\max} = 5a_0$ for top-type (*T*) sites (see Fig. 28). Analogously, in the case of adatomic ordering (long-range order), for a pronounced ordered effect, it is reasonably to consider superlattice structures with the same relative content of ordered impurity (ad)atoms as for random and correlation cases [112].

4.3. The Strain and Defect Responses in the Electronic States and Transport

Within the scope of the theoretical methodology and modelling approach presented in the previous two subsections, this subsection (including several sub-subsections) mainly exhibits the calculated electronic densities of states, diffusivities, and conductivities in the imperfect (impure) (un)strained graphene sheets. In most of the reported below results of the numerical calculations, the size of computational domain was 1.7 million of atoms, which corresponds to graphene lattice of $\approx 210 \times 210$ nm^2 size. There are also comparisons of numerical and relevant experimental findings.

4.3.1. Sensitivity to Direction of the Uniaxial Tensile Strain

Before considering the graphene with defects of various types, it is reasonably to examine firstly the defect-free graphene subjected to different values of relative uniaxial tension $\varepsilon \in [0\%, 30\%]$ along above-mentioned two directions. Numerically calculated DOS curves in Fig. 30 agree with analytically obtained results [87]. A spectral gap appearance requires deformations at least of $\approx 20\%$ along zigzag direction (Fig. 30, *a*), while there is no any gap opening for (even large) deformations

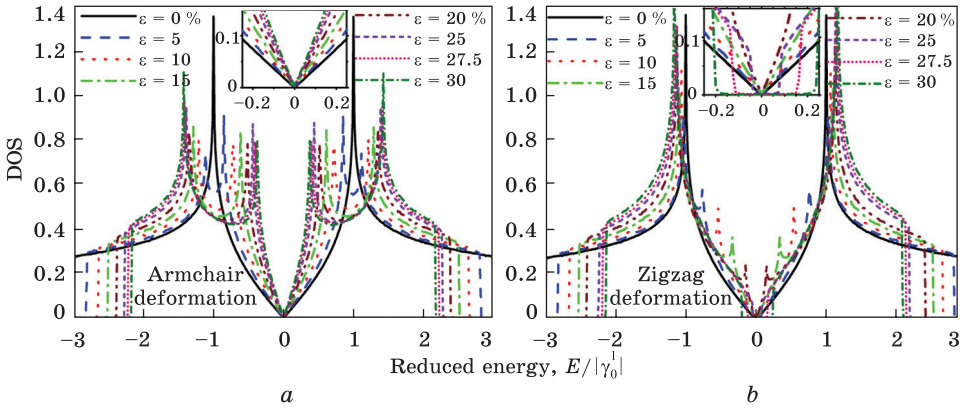

Fig. 30. Density of states (DOS), in units of $1/|\gamma_0^1|$, as a function of the relative longitudinal strain (ε) for pristine graphene monolayer stretched along directions parallel to the armchair (*a*) and zigzag (*b*) edges [104]

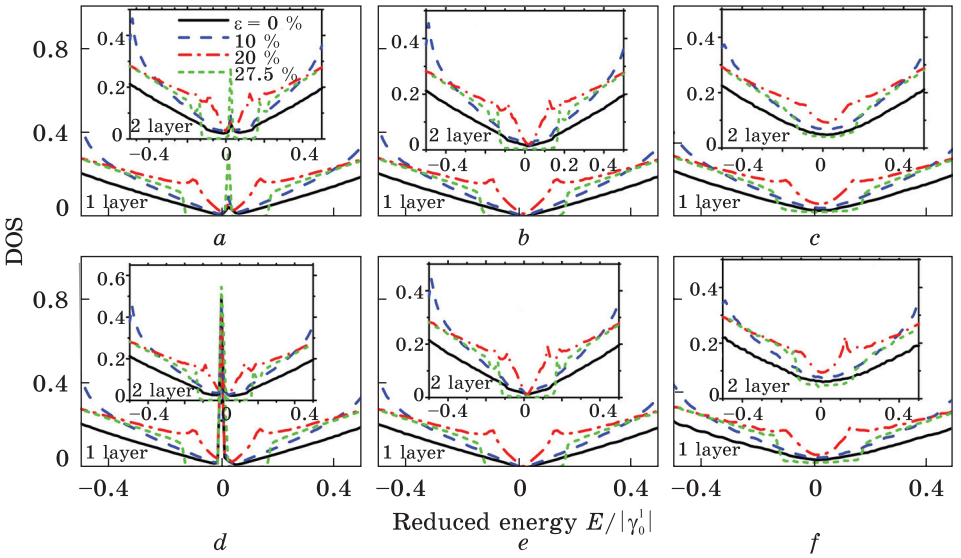

Fig. 31. DOS for zigzag strained (0% ≤ ε ≤ 27.5%) single- (main panels) and bilayer (insets) graphene containing 0.1% of randomly-distributed point defects, namely: (*a*) resonant impurities (52), (*b*) short- and (*c*) long-range Gaussian impurities (53), (*d*) vacancies, (*e*) short- and (*f*) long-range Gaussian hoppings (55) [104]

along armchair direction (Fig. 30, *b*). Some authors [87, 91, 97, 100] explain the band-gap opening in the terms of the location of the Dirac points in the Brillouin zone (Dirac point is a point of vanishing DOS where the valence and conduction bands touch each other conically). They [87, 91, 97, 100] write that spectral gap appears because of 'moving' the two non-equivalent Dirac points within the first Brillouin zone of

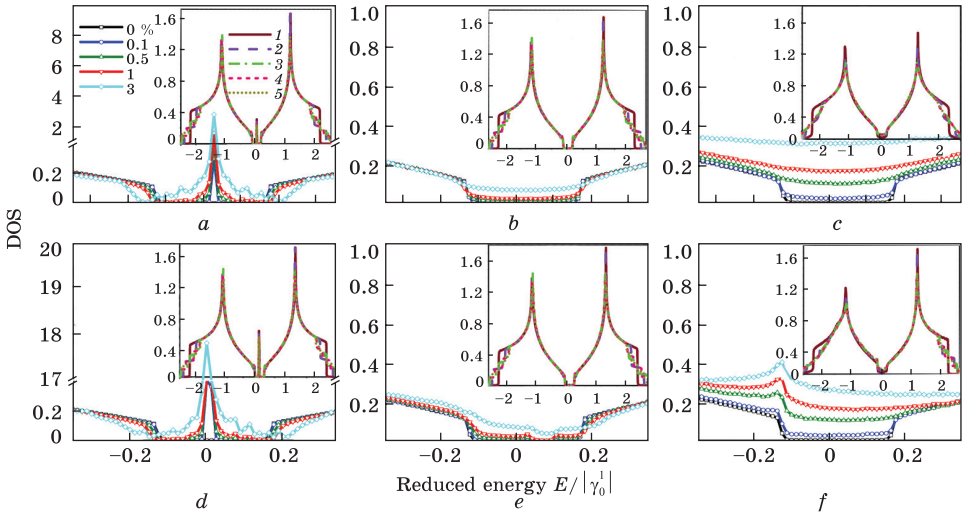

Fig. 32. The same as in the previous figure, but for a fixed zigzag strain (ε = = 27.5%), different (0–3%) concentrations of defects (main panels) and various numbers (1–5) of layers (insets) [104]. Main panels: graphene is single-layer. Insets: defect content is 0.1%

the reciprocal space; they shift at a zigzag deformation, come nearer towards each other, and eventually merge. However, we stress that the modification of the Brillouin zone is only a simple effect of lattice transformation from honeycomb into orthorhombic one due to the applied tensile strain. In fact, the band gap opening originates from an additional displacement of both graphene sublattices with respect to each other that occurs most pronouncedly at a deformation along zigzag direction. Indeed, an armchair deformation identically influences on all bond lengths, — increases them (Fig. 27), — and remains both sublattices undisplaced (besides their equilibrium shift by the vector $\mathbf{h} = \mathbf{a}_1/3 + 2\mathbf{a}_2/3$). Whereas zigzag deformation affects bond lengths differently, — increases bonds in the zigzag direction, while decreases those in the armchair one (Fig. 27), — and (besides the shift onto the **h** vector) additionally displaces the sublattices.

Since the armchair deformation does not result to the band gap opening even for pristine graphene, results in Figs. 31 and 32 deal with case of uniaxial tensile strain along zigzag direction only. High energy values (far from the Dirac point, conventionally at $E = 0$) are less practically (experimentally) realizable, therefore they are not depicted in Fig. 31, where DOS is calculated for single- (main panels) and two-layer (insets) strained graphene with a fixed (0.1%) content of random defects. The DOS curves for mono- and bilayer graphene (Fig. 31) as well as for three-layer, four-layer, and five-ply one (Fig. 32) are similar ex-

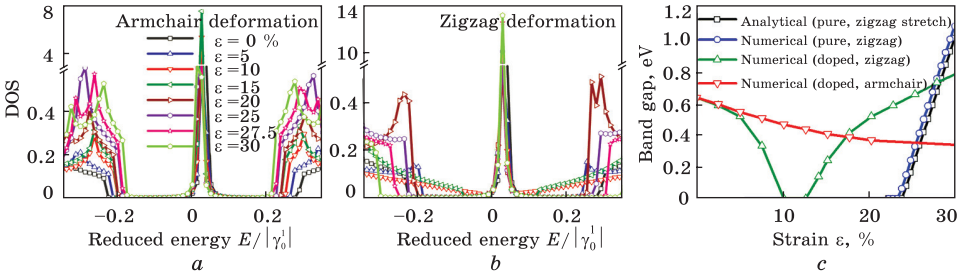

Fig. 33. (*a*, *b*) DOS for graphene monolayer with 3.125% of ordered resonant impurities (oxygen- or hydrogen-containing molecules) at different (up to 30%) values of the stretching along armchair (*a*) and zigzag (*b*) directions [104]. (*c*) Comparison of analytically [87] and numerically calculated band gap energies *vs.* the uniaxial deformation along zigzag direction for monolayer graphene without defects (squares and circles) and with 3.125% of ordered hydroxyl groups (triangles) [104]

cept near the edge of spectrum for large energies E (see insets in Fig. 32), which is an indication of the band-structure similarity, independently on the number of layers. As for unstrained graphene [150], the cause of such similarity lies in the energy band parameters defining intra- and inter-layer hopping integrals designated in Fig. 27: intra-layer nearest-neighbour hoping integral is circa ten times larger than the both inter-layer parameters, *i.e.*, inter-layer interaction is much weaker than the intra-layer one.

As Figures 31, *a*, *d* and 32, *a*, *d* show, resonant impurities (oxygen- or hydrogen-containing molecules) and vacancies similarly alter the DOS of the strained graphene; they bring an increase in spectral weight (central peak) near the Dirac point. The central peak (being attributed to the impurity (or vacancy) band) increases and broadens with increasing the resonant impurity (or vacancy) concentration (see Fig. 32, *a*, *d*). The principle distinction between O- or H-containing molecules and vacancies concerning their effects on the spectrum consists in position of the central peak (impurity/vacancy band) in the DOS curves: it is centred at a neutrality point in case of vacancies, whereas it is shifted from it for the hydroxyl groups due to the nonzero (positive) on-site potential modelling them. In contrast to the resonant impurities and vacancies, the Gaussian potentials and hoppings do not induce low-energy impurity (vacancy) band around the neutrality point as shown in Fig. 31, *b*, *c*, *e*, *f*. However, the van Hove singularities also undergo suppressing, especially at a long-ranged potential (hopping) action (Fig. 32, *b*, *c*, *e*, *f*).

Like for the perfect graphene (Fig. 30, *b*), the spectrum is also strongly gapless for small and even moderate strains of impure graphene (Fig. 31). The gap overcoming requires the threshold (zigzag) deformations over $\varepsilon \approx 20\%$ for non-long-range acting impurities or vacancies (Fig. 31, *a*, *b*, *d*, *e*), whereas the 'long-range' potentials (hoppings) smear

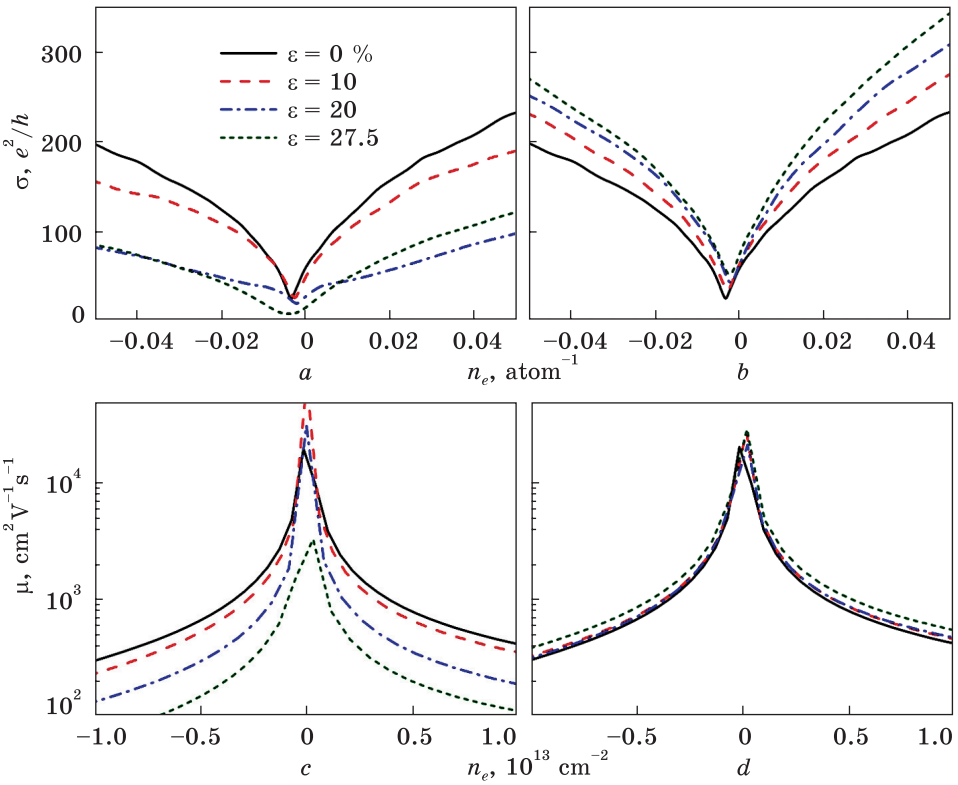

Fig. 34. (*a*, *b*) Conductivity σ (49) and (*c*, *d*) mobility $\mu = \sigma/(en_e)$ *vs.* the electron (or hole) density n_e ($-n_e$) for graphene containing 0.1% of random weak impurities (51) strained uniaxially along (*a*, *c*) zigzag or (*b*, *d*) armchair edge [188]. Both conductivity ($\sigma \equiv \sigma_{xx} \equiv \sigma_{\text{zigzag}}$) and mobility ($\mu \equiv \mu_{xx} \equiv \mu_{\text{zigzag}}$) are calculated along zigzag edge (see Fig. 27, *b*, *c*)

gap region and transform it into quasi- or pseudo-gap — plateau-shaped deep minimum in DOS near the Dirac point (Fig. 31, *c*, *f*). Increase in defect concentration does not change the plateau width, however enhances its spectral weight to the complete smearing even at the short-range potentials (hoppings) as shown in Fig. 32, *b*, *c*, *e*, *f*).

Figure 33, *a* and *b* shows DOS around the Fermi level as a function of tensile strain $\varepsilon \in [0\%, 30\%]$ for single-layer graphene with a fixed concentration of the ordered hydrogen or oxygen adsorbed atoms. The band gap decreases slowly (however permanently), if armchair deformation increases. However, in case of the zigzag strain, the band gap initially (for $0\% \le \varepsilon \le 10\%$) becomes narrower and narrower up to the total disappearance, but then, at a certain threshold strain value ($\varepsilon_{\text{min}} \approx 12.5\%$), the gap reappears, grows up, and can be even wider than it was before the stretching (Fig. 33, *c*). Importantly, this threshold value ε_{min}, when

the band gap opens, is lower in comparison with those that have been estimated earlier for perfect defect-free graphene layers subjected to the uniaxial zigzag strain ($\varepsilon_{min} \approx 23\%$ [87]), shear deformation ($\varepsilon_{min} \approx 16\%$ [91]), and almost coincides with the value expected combining shear with armchair uniaxial deformations ($\varepsilon_{min} \approx 12\%$ [91]).

Comparing the band-gap energies calculated analytically in [87] and numerically computed for pristine as well as for doped graphene subjected to uniaxial tensile deformation along zigzag-edge direction (Fig. 33, *c*), one can see a pronounced non-monotony of the curve for strained graphene with ordered pattern of defects. Such abnormal nonmonotonic behaviour of the strain-dependent band gap mainly originates from the simultaneous contribution of two factors: impurity ordering and applied strain. Note that numerically obtained curve for defect graphene in Fig. 33, *c*) also becomes linear for strains beyond the ≈20% and crosses other two curves for pristine graphene close to its predicted failure limit point (≈27.5% [94]).

In Figure 33, *c*, for predicted graphene failure strain of ≈27.5%, the maximal band gap reaches ≈0.74 eV. If the strain reaches value of 30%, the band gap energy is expected of ≈0.8 eV (Fig. 33, *c*). These calculated band gap values are strongly particular, since the DOS curves in Fig. 33, *a*, *b* are calculated for a fixed (3.125%) content of ordered dopants described by the model on-site potentials with model band parameters adopted from independent approximations. Other impurity concentrations and model potentials give different results. For example, in Fig. 31, *b*, *e* as well as in Fig. 32, *b*, *e*, for 0.1% of random short-range Gaussian impurities (hoppings), the band gap amounts to ≈0.75 eV around the Dirac point, without breaking by the impurity band (central peak) as it is for the resonant impurities. All these estimated band gap energies are comparable with those (up to ≈0.9–1.0 eV) reported in Refs. [91, 100, 101, 187] for ideal (*i.e.*, clean, undoped, without any defects) graphene sheets in the fields of periodic inhomogeneous [100], local [187], anisotropic biaxial [101], or combined [91] strains.

The field-effect charge carrier conductivity σ and mobility $\mu = \sigma/(en_e)$, calculated along fixed, *viz*. zigzag-edge, direction, are shown in Fig. 34 [188]. This figure clearly demonstrates that conductivity and mobility are sensitive to the direction of uniaxial strain. The stretching up to 27.5% along the zigzag edge substantially reduces both conductivity and mobility, while the same stretching along armchair edge slightly enhances the conductivity and mobility. The revealed charge carrier (electron) transport anisotropy is attributed to difference of deformations of bonds, and therefore hopping parameters, in cases when honeycomb lattice is stretched uniaxially along zigzag- and armchair-edge directions (see Fig. 27, *b*, *c*).

4.3.2. An Ability to Affect the Conductivity through the Dopant Configuration

Since here and further we consider a graphene monolayer only, (for simplicity) let us denote the in-layer nearest-neighbour hopping parameter γ_0^1 (see designations in the previous subsection and Fig. 27 particularly) as u, *i.e.*, $\gamma_0^1 \equiv u_0 = 2.78$ eV — the hopping integral for neighbouring atoms at the equilibrium distance $a_0 = 0.142$ nm.

Due to the honeycomb structure of unstrained graphene lattice, possible adsorption sites can be reduced into three types with high-symmetry favourable (stable) positions; so-called hollow centre (H-type), bridge centre (B-type), and (a)top (T-type) adsorption sites are illustrated in Fig. 28. Taking into account discrepancies in the literature [107–111] on the energy stability (favourableness) of adsorption sites, it is interesting to study how electrotransport properties of unstrained graphene depend on types of adsorption sites (H, B, T) which dopants occupy.

In the case of random configuration of adatoms, the steady diffusive regime is reached for a relatively short time, when electron diffusivity $D_{\text{rnd}}(t)$ saturates (Fig. 35, *a*). If adatoms are correlated (short-range ordered), diffusivity $D_{\text{cor}}(t)$ exhibits an unsaturated behaviour for a longer time, which means that diffusive regime is not yet reached (Fig. 35, *b*). Such a quasi-ballistic behaviour of diffusivity indicates a low-scattered electronic transport, when the scattering process is rather inefficient and gives rise to the quasi-ballistic transport more than to the quasi-diffusive one. However, since there is no the total long-range order, the quasi-diffusive regime occurs when the diffusivity $D_{\text{cor}}(t)$ reaches the maximal value. In the case of adatomic ordering with ideal long-range order, when there are no any disorders, we observe a ballistic linear behaviour of $D_{\text{ord}}(t)$ for much more longer times (Fig. 35, *c*) as compared with $D_{\text{rnd}}(t)$ and $D_{\text{cor}}(t)$. This situation resembles case [189] when electrons propagate mainly out-of-the-sublattice containing (ordered) substitutionally-dopant atoms. We would expect such a ballistic regime for very large times (and even at $t \to \infty$) for infinite graphene

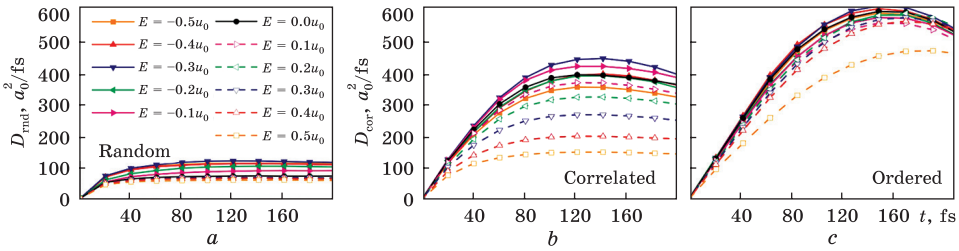

Fig. 35. Electron diffusivity *vs.* time within the energy range $E \in [-0.5u_0, 0.5u_0]$ for random (*a*), correlated (*b*), and ordered (*c*) potassium adatoms located on hollow (H) adsorption sites (see Fig. 28) [112]

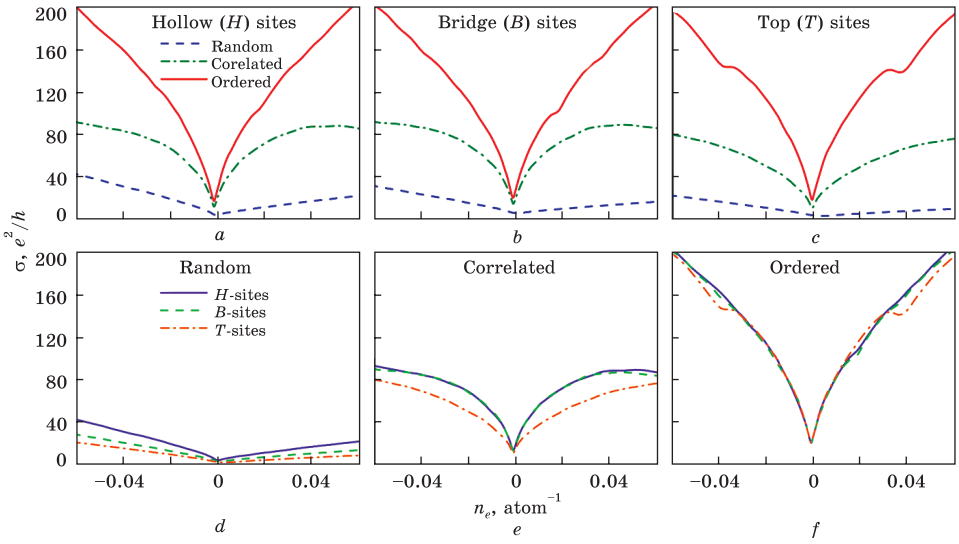

Fig. 36. Conductivity *vs.* the electron density for 3.125% of random, correlated, and ordered potassium adatoms occupying hollow (*H*), bridge (*B*), or top (*T*) adsorption sites (see Fig. 28) [112]

sheet. However, although our graphene computational domain contains several millions of atoms as indicated above, it is finite at all. When the electron wave packet reaches the reflecting edges of graphene domain, the quasi-localization effects can contribute to $D_{\text{ord}}(t)$, especially, due to those long-range ordering adatoms, which are close to the boundary of the sample and, therefore, differ in their local coordination environment from those reside in the sample interior. Another contribution to immobilization disorder comes from the tails of scattering potential due to its long-range features. That is why $D_{\text{ord}}(t)$ decreases after reaching the maximum in the shown time interval. Nevertheless, the maximal value of $D_{\text{ord}}(t)$ is substantially higher than the maximum of both $D_{\text{cor}}(t)$ and $D_{\text{rnd}}(t)$: $D_{\text{rnd}}^{\max}(t) < D_{\text{cor}}^{\max}(t) < D_{\text{ord}}^{\max}(t)$ (Fig. 35). Note that, if the diffusive regime is not reached completely, the semi-classical conductivity σ cannot be defined in principle. However, σ is extracted for the case of ordered adatoms using the highest $D_{\text{ord}}(t)$, when its quasi-ballistic behaviour turns to quasi-diffusive one.

Figure 36 represents the calculated conductivity (σ) as a function of electron ($n_e > 0$) or hole ($n_e < 0$) concentration, $\sigma = \sigma(n_e)$, for different positions (*H*, *B*, *T*) and distributions (random, correlated, and ordered) of adatoms in graphene. For a visual convenience, the same (nine) curves in Fig. 36, *a*–*f* are positioned in two panels (upper and lower). In the upper panel, figures *a*–*c* demonstrate how correlation and ordering affect the conductivity for each of *H*, *B*, and *T* adsorption types. In the

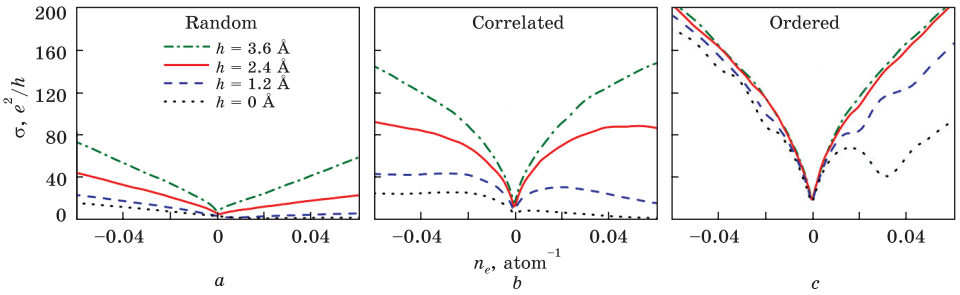

Fig. 37. The same as in the previous figure, but when adatoms occupy hollow (*H*) adsorption sites (see Fig. 28) at different adsorption heights *h* [112]

lower panel, figures *d*–*f* exhibit how these three types of sites influence on the conductivity for each of random, correlated (with maximal correlation lengths), and ordered adatomic distributions. The conductivity, σ, exhibits linear or nonlinear (sublinear) electron-density dependencies. The linearity of $\sigma = \sigma(n_e)$ takes place at the randomly distributed potassium adatoms and indicates dominance of the long-range contribution to the scattering potential, while sublinearity occurs at non-random (correlated and ordered) positions of potassium adatoms and is indicative of the dominance of short-range component of the scattering potential. This is in accordance with other studies (see, *e.g.*, [156] and references therein), where the pronounced linearity and sublinearity of $\sigma = \sigma(n_e)$ are observed for long-range scattering potential (appropriate for screened charged impurities with ionic bond in graphene) and short-range potential (appropriate for neutral covalently bond adatoms), respectively. These results illustrate manifestation of contrasting scattering mechanisms for different spatial distributions of metallic (and even non-metallic as recently revealed in Ref. [190]) impurity atoms.

Since maximal value in a temporal evolution of diffusivity for ordered impurities substantially exceeds its value for correlated defects and much more for randomly distributed ones (Fig. 35), a considerable increase in conductivity due to the correlation and, much more, to the ordering of adatoms as compared with their random distribution is seen from graphs in Fig. 36, *a*–*c*. Graphs in Fig. 36, *d*–*f* allow seeing how different types of adsorption sites affect the conductivity for each type of distribution. If adatoms are randomly distributed, conductivity depends on types of adsites: *H*-, *B*-, or *T*-type ones (Fig. 36, *d*: $\sigma^H_{\text{rnd}} > \sigma^B_{\text{rnd}} > \sigma^T_{\text{rnd}}$. For a correlated distribution, conductivity depends on how adatoms manifest themselves: as substitutional (being on *T*-sites) or interstitial (being on *H*- or *B*-sites) atoms (Fig. 36, *e*): $\sigma^H_{\text{cor}} \approx \sigma^B_{\text{cor}} > \sigma^T_{\text{cor}}$. If adatoms form the ordered superstructures, with equal periods, the conductivity is practically independent on the adsorption type, especially at the low electron densities (Fig. 36, *f*): $\sigma^H_{\text{ord}} \approx \sigma^B_{\text{ord}} \approx \sigma^T_{\text{ord}}$.

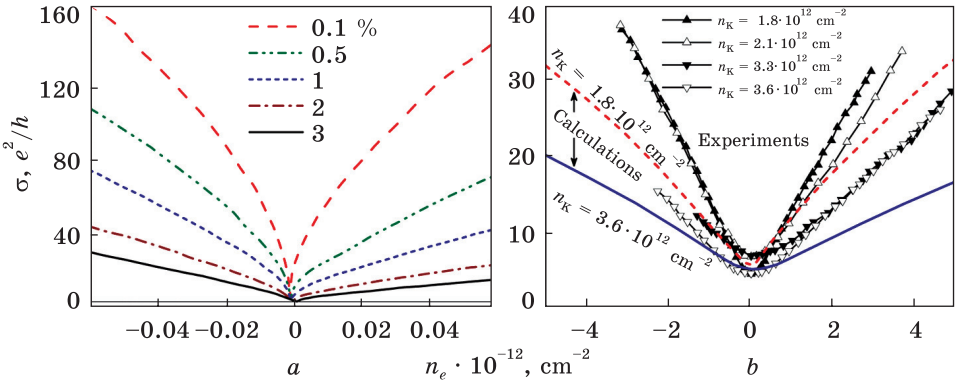

Fig. 38. (*a*) Calculated conductivity [112] as a function of charge carrier density at various concentrations of potassium adatoms, $0.1\% \le n_K \le 3\%$, which are randomly distributed over the random adsorption sites of graphene lattice. (*b*) Experimental [137, 191] and calculated [112] conductivities *vs.* the realistic electron density for different contents of potassium impurities in graphene typically observed in experiments. Experimental data ▲ [191], Δ [137], ▼ [137], ∇ [191] correspond to $n_K = 0.047\%, 0.055\%, 0.086\%, 0.094\%$, respectively. Calculated dashed and solid curves (*b*) relate to $n_K = 0.047\%$ and 0.094%, respectively

In our model, the higher (lower) adatomic elevation over the graphene surface corresponds to the weaker (stronger) scattering-potential amplitude. It means physically that more weak (or strong) regime of electron scattering on the charged impurity adatoms. Though the values of adsorption height, h, reported in the literature for potassium, do not disagree as much as for the adsorption energy (see Table 1 in [112]), for the model and calculation completeness, h varies in a wide range (up to $h = 3.6$ Å), including exotic case of $h = 0$, when impurity atoms act as strictly interstitial ones. The calculated curves representing the charge-carrier-density-dependent conductivity for (random, correlated, and ordered) adatoms resided on (the most favourable for potassium) hollow sites and elevated on different h are depicted in Fig. 37. Here, we do not consider the cases of bridge and top sites — less favourable for potassium atoms occupation — since it leads to qualitatively the same results. As follows from Fig. 37, *a* and *b*, at least for hole densities ($-n_e > 0$), two (three) time increase or decrease in adsorption height h for randomly- or correlatively-distributed potassium adatoms results to approximately two (three) time enhancement or reduction in σ (respectively). Thus the conductivity approximately linearly scales with adsorption height of random or correlated adatoms, $\sigma(h) \propto h$, or, more precisely, $\sigma(h) = \sigma(0) + O(h)$, where $O(h)$ is a big O notation. However, for ordered potassium adatoms, the σ remains practically unchanged with varying of h in the realistic range of adsorption heights (see Table 1 in Ref. [112]) and even in all range at issue ($0 \le h \le 3.6$ Å) for hole densities (Fig. 37, *c*). We

attribute this to the dominance of short-range scatterers in case of their ordered state (as it was mentioned above). Indeed, the Gaussian fitting for the scattering potential in Fig. 29, *a* yields the effective potential radius $\xi = 2.21a$, which is commensurable with quantities of adsorption heights h at issue (and even less than $h = 3.6$ Å).

Let us compare obtained numerical results with available other (experimental and theoretical) findings. Results in Figs. 36 and 37 agree with experimentally observed features of $\sigma = \sigma(n_e)$ for potassium-doped graphene [191, 137]:

- on K-doping, conductivity decreases and its dependence on charge carrier density (controlled by gate voltage $V_g \propto n_e$ [192]) is linear (sublinear) at higher (lower) K-concentration;
- conductivity curve is an asymmetric one for electrons versus holes for the asymmetric (*i.e.*, sign-constant) scattering potential; however, the electron-hole asymmetry is absent for symmetric (*i.e.*, alternating in sign) potential [156];
- the minimal conductivity $\sigma_{\min} \approx 4e^2/h$ (h is the Planck constant) shifts from a charge neutrality point to the side of positive energies E corresponding in our notations to the n-type charge carries, *i.e.*, negative gate voltage (see Fig. 38, *a*);
- electron-density-dependent conductivity becomes more sublinear and enhances as the correlation degree for adatoms increases.

The above mentioned four features do not depend on types (H, B, or T) of adsorption sites and therefore become apparent also for a random arrangement of adatoms at a random type of adsorption sites as it is shown in Fig. 38, *a*.

Note that this subsection deals with numerical calculations, in which the relative electron densities within the range of $n_e \leq 6 \cdot 10^{-2}$ atom^{-1} (*i.e.*, $n_e \leq 2.3 \cdot 10^{14}$ cm^{-2}) are used. Such n_e values are larger in comparison with those commonly used in the relevant experiments, $n_e^{\exp} \leq 1.8 \cdot 10^{-3}$ atom^{-1} $n_e^{\exp} \leq 7 \cdot 10^{12}$ cm^{-2}) [137, 191]. The larger electron density interval is used in order to model electron transport for impurity densities $n_{\text{imp}} \leq 3.125\%$ ($n_{\text{imp}} \leq 1.19 \cdot 10^{14}$ cm^{-2}), which are larger than densities in typical experimental samples, $n_{\text{imp}}^{\exp} \leq 0.14\%$ ($n_{\text{imp}}^{\exp} \leq$ $\leq 5.4 \cdot 10^{12}$ cm^{-2}) [137, 191]. To achieve the stable diffusive transport regime for experimentally typical impurity concentrations, it is necessary to perform calculations on graphene sheets with much more number of atoms, which requires much more computation time and capabilities. Therefore, to compare calculable conductivity with experimental one for potassium-doped graphene, the size of computational domain was increased up to ten millions of atoms, which corresponds to $\approx 500 \times 500$ nm^2, although even this size is not quite enough to reach the long-time stability of diffusive regime at very small impurity content. Experimental and calculated conductivities for typical densities

of electrons and impurity potassium adatoms in graphene are presented in Fig. 38, *b*. Both experimental and calculated conductivities (in Fig. 38, *b*) exhibit a linear (or a quasi-linear) behaviour. However, quantitative agreement is less good. This can be attributed to the contribution of quasi-localization effects due to the insufficiently large graphene sheet for the stable long-term diffusive regime to be reached at the wave packet propagation.

A significant sublinear behaviour of electron-density-dependent conductivity and its saturation for very high electron densities at the spatial correlations among the charged impurities in contrast to the strictly linear-in-density graphene conductivity for uncorrelated random charged impurities (Figs. 36, *a*–*e*, and 37, *a*–*b*) is also in agreement with theoretical findings in [185, 186]. Increase in conductivity as the increasing adatomic correlation is also sustained theoretically [185, 186] within the standard semi-classical Boltzmann approach in the Born approximation.

At first sight, it may seem that the last statement in the last paragraph contradict to the results and conclusions in Ref. [156], where the authors reported that correlation in the spatial distribution for the strong short-range scatterers and for the long-range Gaussian potential does not lead to any enhancement of the conductivity in comparison to the uncorrelated case. However, there is no any disagreement. Results in Ref. [156] are obtained for alternation (positive–negative) Gaussian scattering potential (53) with potential height U uniformly distributed within the symmetric range $[-\Delta, \Delta]$ (Δ is a maximal potential height). Such a potential is commonly used in the literature as a model potential without specification type (kind) of impurity (ad)atoms. While here, and in Ref. [112], the potential is a constant-sign (negative) being adopted from independent *ab initio* calculations [184] strictly for potassium adatoms in graphene (see Fig. 29, *a*). Really, 'symmetric' Gaussian potential (with $U \in [-\Delta, \Delta]$) does not give rise in conductivity (as shown in Ref. [156]), while the 'asymmetric' Gaussian potential (with $U < \Delta$ or $U > \Delta$) or any other (Gaussian or non-Gaussian) only positive or only negative potential (like that in Fig. 29) enhances the conductivity.

4.3.3. The Strain-Dependent Band-Gap Patterns

To construct the strain-dependent band-gap diagrams (maps) for monolayer graphene subjected to different types of deformations, — stretching (Fig. 27, *b* and *c*), shearing (Fig. 39, *a* and *b*), or their combination (Fig. 39, *c*), — we calculated a large number of corresponding DOS curves and determine the corresponding band gaps (if any is opened at all by the applied strains). The $14 \times 14 = 196$ DOS curves (like those in Fig. 30), calculated for different relative values of uniaxial zigzag and

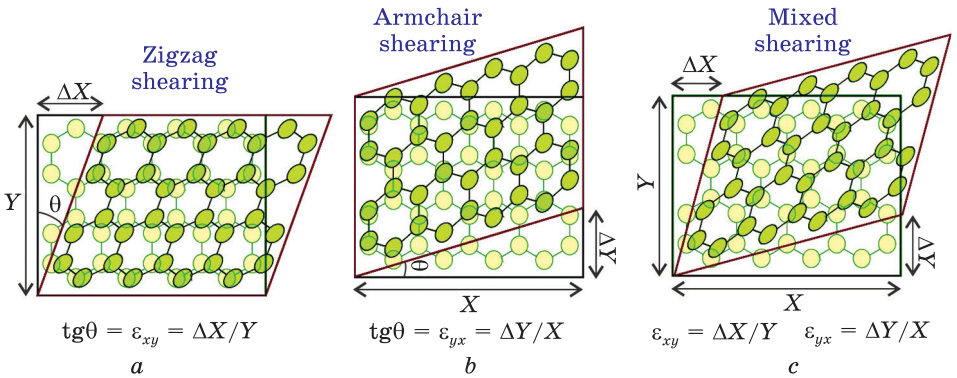

Fig. 39. Graphene lattice subjected to shearing along zigzag (*a*), armchair (*b*), or both (*c*) directions (the balls denoting atoms remain nonstretched in experiment) [15, 16]. See also stretched lattice in Fig. 27, *b* and *c*

armchair deformations $\varepsilon \in [0, 26\%]$ (with a strain step $\Delta\varepsilon \approx 2\%$) result in the band gap diagrams [15] shown Fig. 40. As Figure 40, *b* demonstrates, the shear strain also induces, similar to the uniaxial tensile deformation, a band gap opening only above a certain threshold deformation value. However, in contrast to the tensile strain, although the band gap emergence is strongly sensitive to direction of the stretching, reaching a critical threshold shearing along both (armchair and zigzag) edges (directions) is needed for the gap opening: $\varepsilon_{xy}^{\min} = \varepsilon_{yx}^{\min} \approx 17\%$, see Fig. 40, *b*. The shearing along both edges (so-called mixed shear strain as shown in Fig. 39, *c*) can be associated with the diagonal values on the band-gap pattern in Fig. 40, *b*, where shears along both armchair and zigzag directions are equal. Figure 40, *b* shows that the band gap reaches values ≈4 eV at large strains up to 26%, close to the graphene failure limit.

As it becomes apparent from Fig. 40, *c*–*h*, the combination of different uniaxial tensile and shear stresses affect differently the band gap. Armchair stretching enlarges the gap induced by shear strain (Fig. 40, *c*–*e*) up to ≈6 eV (Fig. 40, *e*) for extremely high values of the stretching combined with mixed shear. On the contrary, zigzag stretching causes degradation of the band gap induced by any of the three types of shear strains (Fig. 40, *f*–*h*). Uniaxial armchair strain combined with mixed shearing deceases the minimally required threshold strain $\varepsilon^{\min}$ necessary for band-gap opening. In particular, $\varepsilon^{\min}$ drops to $\varepsilon_{xy}^{\min} = \varepsilon_{yx}^{\min} \approx 12\%$ when mixed shearing is accompanied with $\varepsilon_{yy}^{\min} \approx 12\%$ of armchair stretching (Fig. 40, *e*).

The main features that can be extracted from Fig. 40 are the threshold strain needed for band gap opening (if any) and the maximal band-gap value, which can be reached by the non-destructive deformations. These values are summarized in Ref. [15] (see Table 1 therein) for different types of strains. The comparison of the numerical results [15]

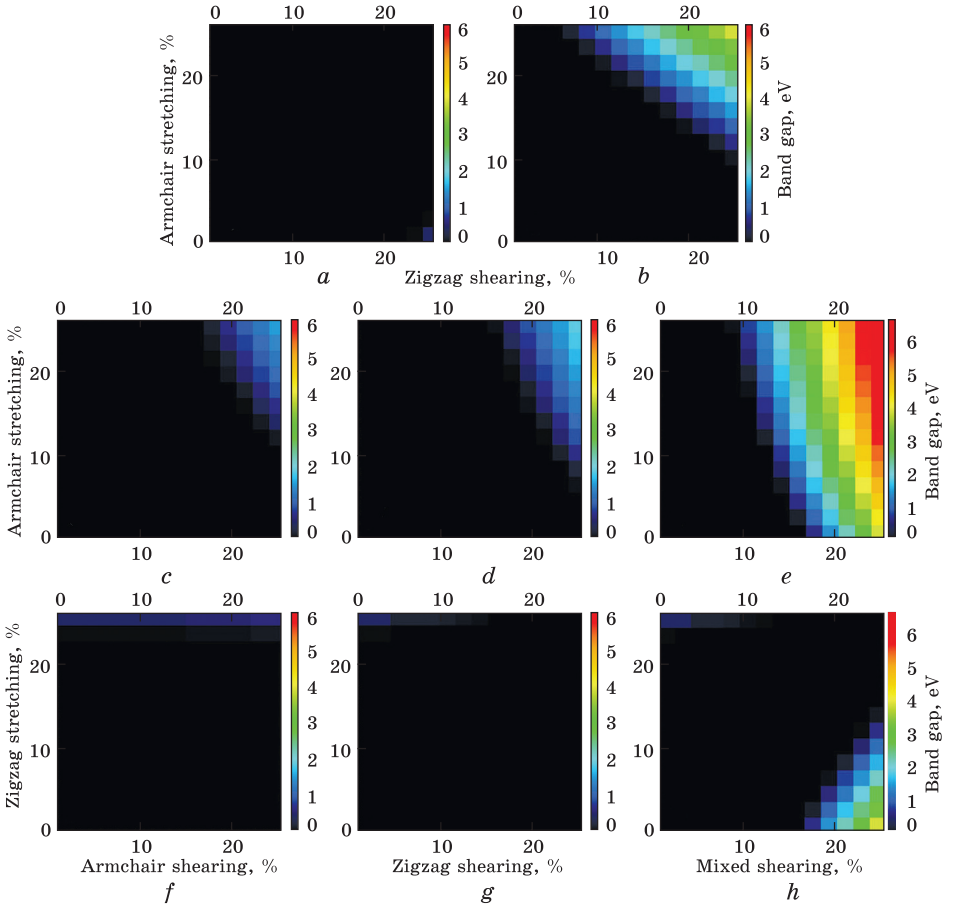

Fig. 40. Strain-dependent band-gap patterns (diagrams) for graphene under tensile or/and shear deformations (up to 26%): (*a*) uniaxial tensile strain along zigzag or/and armchair direction as shown in Fig. 27, *b* and *c*; (*b*) shear strain along armchair or/and zigzag directions (Fig. 39, *a*–*c*); uniaxial tensile strain along (*c*–*e*) armchair or (*f*–*h*) zigzag direction combined with shear strain along (*c*, *f*) armchair, (*d*, *g*) zigzag, or (*e*, *h*) both directions with equal shear-strain tensor parameters ε_{xy} and ε_{yx} denoted in the previous figure [15]

with other available theoretical data in the literature indicates good qualitative and quantitative agreement between the critical strain values for the uniaxial zigzag, shear, and combined deformations obtained either analytically or also numerically in Refs. [87, 91, 193].

Figure 40 and summarized data in the table of Ref. [15] clearly demonstrate that different types of strains and their combination can sensitively affect the band gap. Despite the fact that pure uniaxial armchair stress is ineffective in the creation of a band gap, this type of stress strongly enlarge the shear-induced gap, increasing the gap far

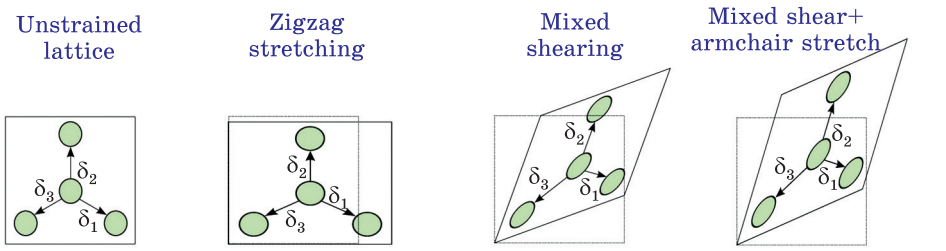

a	*b*	*c*	*d*
$\frac{\lvert\delta_1\rvert}{a_0}=1\ \frac{u_1}{u_0}=1$	$\frac{\lvert\delta_1\rvert}{a_0}=1.19\ \frac{u_1}{u_0}=0.52$	$\frac{\lvert\delta_1\rvert}{a_0}=0.85\ \frac{u_1}{u_0}=1.66$	$\frac{\lvert\delta_1\rvert}{a_0}=0.87\ \frac{u_1}{u_0}=1.59$
$\frac{\lvert\delta_2\rvert}{a_0}=1\ \frac{u_2}{u_0}=1$	$\frac{\lvert\delta_2\rvert}{a_0}=0.96\ \frac{u_2}{u_0}=1.14$	$\frac{\lvert\delta_2\rvert}{a_0}=1.05\ \frac{u_2}{u_0}=0.95$	$\frac{\lvert\delta_2\rvert}{a_0}=1.20\ \frac{u_2}{u_0}=0.51$
$\frac{\lvert\delta_3\rvert}{a_0}=1\ \frac{u_3}{u_0}=1$	$\frac{\lvert\delta_3\rvert}{a_0}=1.19\ \frac{u_3}{u_0}=0.52$	$\frac{\lvert\delta_3\rvert}{a_0}=1.16\ \frac{u_3}{u_0}=0.58$	$\frac{\lvert\delta_3\rvert}{a_0}=1.20\ \frac{u_3}{u_0}=0.51$

Fig. 41. Modified nearest neighbour bond lengths (δ_1, δ_2, δ_3) and renormalized hopping integrals (u_1, u_2, u_3) in graphene lattice (*a*) under different types of strain [15]. Here, *b* — 26% of uniaxial tensile strain along zigzag edge, *c* — 18% of shear strain along both armchair and zigzag directions, *d* — 18% of mixed shearing combined with 18% of uniaxial tensile strain along armchair direction. The balls denoting atoms remain nonstretched in the experiments

beyond the silicon's value, which is enough for creation of a transistor. Such an enhancement happens with all types of shear strains, hence, the only thing required to control is the armchair direction of the uniaxial stretching. Desired values of the band-gap for graphene applications in nanoelectronic devices such as transistors may be achieved in a wide range of band-gap values and through different types of deformations including their combination.

Figure 41 illustrates the modification of the three nearest-neighbour bond lengths (δ_1, δ_2, δ_3) and hence of the hopping parameters (u_1, u_2, u_3) when applying uniaxial and shear tensions as well as their combination. Whereas the unstrained bonds (in Fig. 41, *a*) provide a zero energy gap, according to Fig. 40, a non-zero gap emerges for all other three cases (see Fig. 41, *b*–*d*). The 26%-stretching along zigzag direction (in Fig. 41, *b*) results in the ≈0.5 eV energy gap (Fig. 40, *a*). The 8%-shearing along both armchair and zigzag directions (in Fig. 41, *c*) provides a gap of ≈0.66 eV (Fig. 40, *b*). The combination of 18% of mixed shear with armchair tensions (in Fig. 41, *d*) results in a gap of ≈3.02 eV (Fig. 40, *e*). The hopping integrals (in units of u_0) denoted in Fig. 41, *b*–*d* violate the triangular inequalities [87, 194],

$$\left|\left|\frac{u_1}{u_2}\right|-1\right|\le\left|\frac{u_3}{u_2}\right|\le\left|\left|\frac{u_1}{u_2}\right|+1\right|, \qquad (57)$$

which act as a general condition (firstly derived in Ref. [194]) for the gapless spectrum of tight-binding electrons on the honeycomb lattice (the inequalities (57) can also be rewritten in a more complicated form in terms of the bond lengths entering into the expression of the bond-length-dependent hopping (50)). Such an agreement indicates compliance between the numerically calculated strain-dependent band-gap maps in Fig. 14 and the analytically obtained hopping-dependent condition (57) for the gapless energy spectrum of the honeycomb lattice.

The stability of the strain-induced band gaps in polycrystalline graphene produced through chemical vapour deposition on a substrate, as one of the most prevalent and mature techniques of graphene growth, is an additional important question, since the majority of graphene films necessary for industrial applications are typically polycrystalline [195]. The polycrystalline structure of graphene manifests itself as a main problem in the band-gap engineering, since it is composed of monocrystalline grains that response differently to the strain, due to their varying spatial orientation. For the most stable and controllable energy gap, graphene samples should be monocrystalline or consist of single-crystalline domains with identical lattice orientations. The presence of a huge amount of grain boundaries, acting as extended line defects in polycrystalline graphene, induces midgap electron states thereby impedes the emergence of a gap. This could be one of the reasons why the attempts to observe a tensile- or shear-strain-induced spectral gap in the polycrystalline graphene samples (CVD-grown on a copper substrate) [89, 90] were not crowned with success. In addition to that, the gap might not be observable due to several other reasons. Although tensile strain of polycrystalline graphene was large, 22.5% [89], it was not sufficient for band (and hence transport) gap opening as long as the zigzag stretching was not in excess of 23%. Moreover, the directional sensitivity becomes pointless (or even impossible) in case of different grain orientations. Applied shear strain up to 16.7% [90] is sufficient for gap opening according to the calculations in Ref. [91], while predictions in Refs. [15, 193] report on rather higher threshold values of the shear strain along both armchair and zigzag directions (Fig. 39, *c*).

4.3.4. Numerically Calculated as Compared with Experimentally Measured Conductivity

Analysing the transfer characteristics of CVD graphene sample loaded to the tensile and shear strains [89, 90], authors of Ref. [16] tried to tailor the electron transport properties of graphene layer involved in our computational domain. Thereto, they [16] varied the types of defects and their contents such to reach as more as a possible similarity

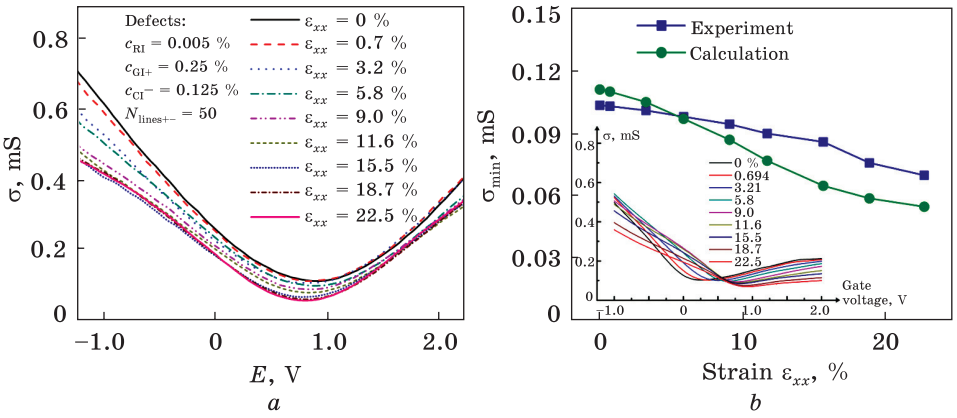

Fig. 42. (*a*) Calculated conductivity σ = σ(*E*) for different values of tensile strain along zigzag direction (Fig. 27, *c*) in graphene containing 0.005% of resonant impurities (51) with $V_0 \equiv V^{RI}$), 0.25% of long-range acting positive and negative Gaussian impurities (53), 0.15% of positive Coulomb impurities (54), 0.125% of negative Coulomb impurities (54), and 50 positive–negative line defects (56). (*b*) Calculated [16] and experimental [89] σ in the Dirac points (σ_{min}) at different strain values, where experimental points are extracted from experimental graphs in the inset [89]

between the numerically calculated and experimentally obtained curves σ = σ(*E*). As a result, the calculated curves in Fig. 42, *a* for zigzag tensile strain (Fig. 27, *c*) exhibit several features observed in experiment [89] (the inset in Fig. 42, *b*). They are: the Dirac points σ_{min} occupy position on the side of positive energy (gate voltage), which implies hole doping; the σ undergoes a downshift in the Dirac points; the slopes of the curves decrease on both sides from the Dirac points, *i.e.* the $\sigma(E_{fixed})$ decreases as the ε increases. The apparent shift of the Dirac points extracted from Fig. 42, *a*) is plotted in Fig. 42, *b*). In contrast to the experiment, there is no a pronounced and relatively slowly decrease of σ min under little tension, but faster decrease at larger strains; we attribute it to the lack of the wrinkle (ripple) releasing (relaxation) effect in our model. The linear decrease of mobility ($\mu = \sigma/(en_e)$) of electrons (holes) with increasing stretching also occurred (see supplementary material) in accordance with the experiment [89].

In contrast to the zigzag stretching, the zigzag and armchair shears (Fig. 39, *a*, *b*) enhance the $\sigma(E_{fixed})$ (Fig. 43, *a*, *b*). However, the conductivity of the Dirac points (σ_{min}) remains practically unchanged (see also Fig. 43, *d*): cases $\varepsilon_{xy} \neq 0$ and $\varepsilon_{yx} \neq 0$). Interestingly, for the mixed shear (Fig. 43, *f*), the conductivity $\sigma(E_{fixed})$, including σ_{min}, exhibits nonmonotonic behaviour as a function of ε: see Fig. 43, *c*, *d*). The nonmonotony of the $\sigma(E_{fixed})$ as a function of shear strain (case $\varepsilon_{xy} = \varepsilon_{yx} \neq 0$ in Fig. 43, *d*) has also been revealed numerically in Ref. [193] and experimentally

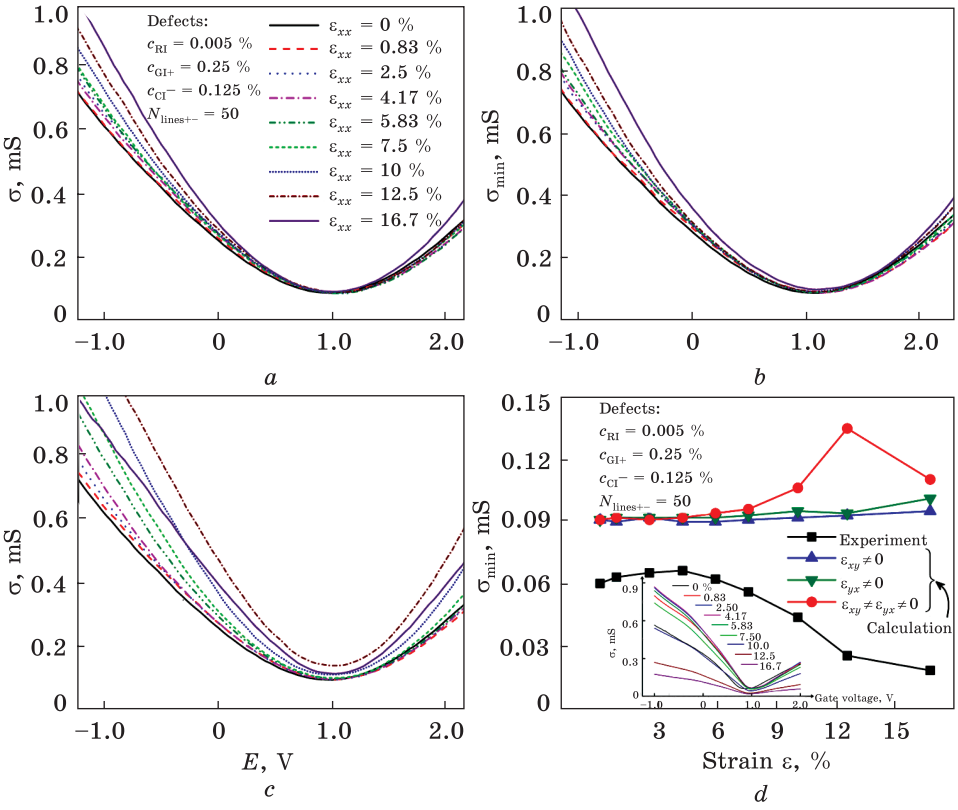

Fig. 43. (*a*)–(*c*) The same as in the previous figure, *a*, but for the shearing (Fig. 13, *a*–*c*) and for 0.005% of resonant impurities (51), 0.25% of long-range positive–negative Gaussian impurities (53), 0.25% of positive–negative Coulomb impurities (54), 0.03% of positive Coulomb impurities (54), and 50 positive–negative line defects (56). (*d*) Calculated [16] and experimental [90] σ_{min}, where experimental points are extracted from experimental graphs in the inset [90]

in Ref. [90]. However, the behaviour of the nonmonotony curves $\sigma_{min} = \sigma(\varepsilon)$ is different. Numerical findings [193] and our calculated results in Fig. 43, *d*) predict an increase of σ and followed decrease when the mixed shear approaches the values close to the threshold one at which the band gap starts to open. The band gap was not observed in the experiment [90]. This is not only because of the significant effect of grain boundaries, as authors [90] mentioned. Another reason for the band gap absent [90] may be attributed to the shearing along either zigzag or armchair graphene-lattice edge (as Fig. 1, *b* in Ref. [90] demonstrates). In contrast, the band gap opens only at the simultaneous shearing along both (zigzag + armchair) directions (mixed shear in Fig. 39, *c*) as reported in Refs. [15, 193].

5. Magnetic-Field-Driven Electronic Properties of Graphene: Effect of Strain and Defects

Among known and currently in use different ways for inducing goal-directed effects in electronic and transport properties of graphene, the application of a magnetic field is extremely useful for addressing its fundamental properties as it provides an external and adjustable parameter which drastically modifies graphene's electronic band structure [196, 197]. Whereas even large parallel magnetic field does not affect the transport properties of graphene [198], perpendicular magnetic field results to formation of non-equidistant Landau levels (LLs) in the energy spectrum, including zero-energy Landau level (LL) at the Dirac point, which caused some unique physical properties, for instance the anomalous integer quantum Hall effect and a finite conductivity at the Dirac point [199, 200].

This section deals with numerical study of responses of uniaxial tensile strain and point or line defects in magnetoelectronic properties of graphene exposed to the perpendicular magnetic field, particularly in the LLs spectrum observed in the calculated densities of electronic states. Such a study is also motivated by the restricted information in the literature about computational details and parameters used in modelling of graphene electronic properties [163, 201]. These computational parameters can play an important role during the computation procedure, especially if they implicitly defined in commonly used different computational packages, like Quantum Espresso, as in Ref. [201].

5.1. Analytical vs. Numerical Findings for Perfect Monolayer

In the presence of an external vector potential **A** applied to the graphene layer, the hopping integrals undergo replacement in accordance with a standard Peierls substitution method [149, 163, 202, 203]:

$$u_{j,j'} = u_0 \exp\left(ie \int_j^{j'} \mathbf{A} d\mathbf{l} \right) = u_0 \exp\left(i \frac{2\pi}{\Phi_0} \int_j^{j'} \mathbf{A} d\mathbf{l} \right); \qquad (58)$$

here, i is an imaginary unit, $\int_j^{j'} \mathbf{A} d\mathbf{l}$ is a line integral of the vector potential from j to j' nearest-neighbouring sites, and magnetic flux quantum $\Phi_0 = h/e$ is a combination of the fundamental physical constants. In the Landau gauge condition for a perpendicular magnetic field $\mathbf{B} = (0, 0, B)$ as shown in Fig. 44, *a*, where x and y Cartesian axes are specified along the zigzag and armchair edges, respectively (see also Fig. 27, *b*, *c*), the vector potential reads as $\mathbf{A} = (-By, 0, 0)$. Then, applying the fundamental theorem of calculus (Newton–Leibniz formula), the hopping parameters for nearest-neighbouring j and j' sites become

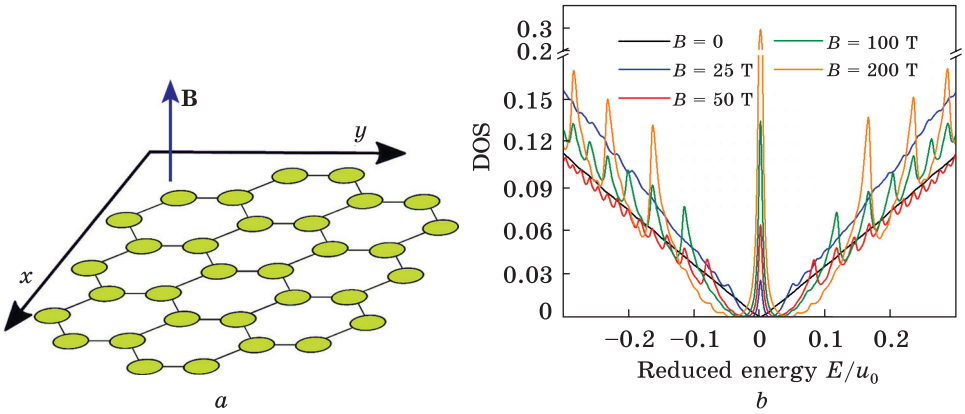

Fig. 44. Graphene lattice in the perpendicular magnetic field **B** (*a*) resulting in the Landau levels on the DOS (in units of reciprocal hopping integral $1/u_0$) as a function of energy E (in units of u_0) for different values of the uniform field $B \in [0, 200]$ T (*b*) [212]

$$u_{j,j'} = u_0 \exp\left(\frac{e}{\hbar} i\phi_{j,j'}\right) = u_0 \exp\left\{\frac{e}{\hbar} i\left[\pm\frac{\sqrt{3}}{2} B\left(y_j a \pm \frac{a^2}{4}\right)\right]\right\}, \qquad (59)$$

where sign '+' or '–' depends on whether m and n, — numbers of j and j' sites along x and y directions designated in Figs. 44, *a* and 27, *b*, *c*, — are even or odd. It is convenient to express y in Eq. (59) in units of the lattice parameter a.

It is known from the theoretical quantum-mechanical predictions that magnetic field, applied perpendicularly to the graphene plane, results to the quantization of electron energy into LLs with an electron–hole energy spectrum that reads as [64, 149, 204–207]

$$E_n = E_0 \pm \hbar\omega_c \sqrt{|n|} \equiv E_0 + \mathrm{sgn}(n)\sqrt{2e\hbar\upsilon_F^2 B\,|\,n\,|} \qquad (60)$$

Table 15. **Analytically obtained and numerically calculated electron energy spectrum, E_n (n = 0, ±1, ±2, ±3), at different values of magnetic field, $B \in$ [25, 200] T, perpendicular to graphene plane [212]. Analytical E_n are extracted from Eq. (60)**

B, T	Method	$E_{n=0}$	E_n = ±1, eV	E_n = ±2, eV	E_n = ±3, eV
25	analytical	0	0.18	0.26	0.31
	numerical	0	0.14	0.22	0.26
50	analytical	0	0.26	0.36	0.44
	numerical	0	0.23	0.32	0.40
100	analytical	0	0.36	0.51	0.62
	numerical	0	0.33	0.46	0.60
200	analytical	0	0.51	0.72	0.88
	numerical	0	0.46	0.66	0.81

with a field-independent energy E_0 in the Dirac point, cyclotron frequency $\omega_c = \upsilon_F\sqrt{2eB/\hbar}$, the Fermi (electron) velocity $\upsilon_F \approx 10^6$ m/s [64], and the quantum number $n = 0, \pm 1, \pm 2, \ldots$ represents an integer LL index being positive ($n > 0$) for electrons and negative ($n < 0$) for holes. The non-equal ($\propto \sqrt{B}$) distances between LLs in graphite were reported in the middle of the last century [208] (see also Ref. [209]). The non-equidistant LLs spectrum (60) for zero-mass carriers in graphene grown on silicon carbide was firstly experimentally observed in Ref. [210] *via* the scanning tunnelling spectroscopy. The sublinear ($\propto \sqrt{B}$) dependence (60) for graphene differs from the typical linear dependence of the LLs energy on both quantization integer n and magnetic field B for an ordinary conductors (normal metals and $2D$ electron gases): $E_n \propto$ $\propto (n + 1/2)B$ [211].

Before proceed to graphene with disorders, in order to validate numerical model, it is reasonably initially consider pristine (*i.e.*, defectless and unstrained) graphene monolayer subjected to the perpendicular magnetic field [212]. Observed Landau levels on the numerically calculated DOS curves in Fig. 44, *b* [212] confirm nonuniform (non-equidistant) distribution of the LLs (the non-equidistance is due to the fact that charge carriers behave themselves in graphene as massless particles and their velocity does not depend on their energy). Electron energy spectrum (E_n) values for different magnitudes of perpendicular magnetic field (25 T $\le B \le$ 200 T) are contained in Table 15. Numerically calculated values of E_n adequately agree with those obtained analytically from Eq. (60).

For clarity's sake, we pay attention to importance of some computational parameters, which usually are hidden from readers but strongly affect DOS curves including positions and width of LLs. Since thickness of the LLs is extremely small, unusually narrow energy step is needed for LLs to be observed on the curves. The size of computational domain, *i.e.*, honeycomb lattice, causes not only significant modification of the DOS, but also plays a crucial role in the observation of LLs in a computer experiment at hand. In case of a relatively small size of the lattice, *e.g.*, smaller than half of million of sites (atoms), the LLs are found to be not clearly observed even for magnetic fields up to 50 T, which are close to those maximal attainable in experiment [213]. LLs tend to be more distinguished and pronounced with the larger lattice size as compared with smaller one. In case of the restricted computational efforts for providing calculations on the honeycomb samples containing several millions of atoms, the higher magnetic fields have to be applied for LLs to be clearly observed on the DOS curves like those in Fig. 44, *b*. Therefore, having sufficient (for adequate modelling) computational domain (1700×1000 lattice sites), but not quite enough for LLs be clearly ob-

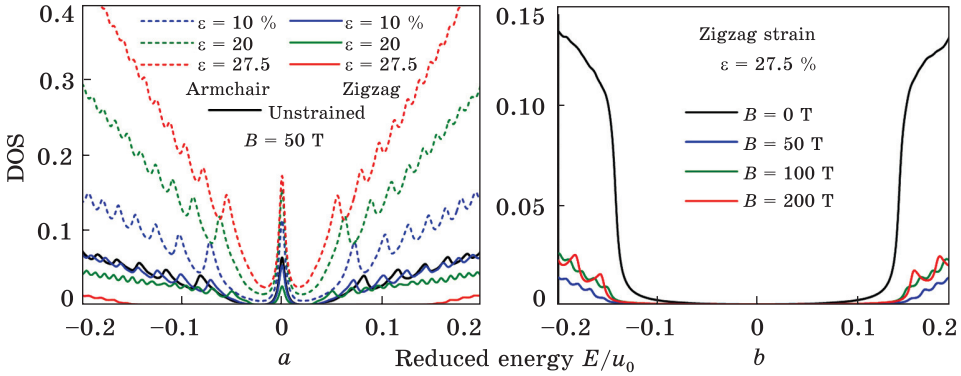

Fig. 45. Mutual action of mechanical and magnetic fields on the DOS of graphene, where *a* — the fixed magnetic field $B = 50$ T with different armchair or zigzag tensile strains ($0 \le \varepsilon \le 27.5\%$), *b* — the fixed zigzag strain $\varepsilon = 27.5\%$ with different values of magnetic field ($0 \le B \le 200$ T) [212]

served at the small magnetic fields, we enhanced maximal value for B up to 200 T, which is nevertheless two times lower as compared with magnetic fields considered in other numerical simulations [214] for much smaller samples.

Another important computational parameter is so-called smoothing coefficient ς, which enters into the master expression for the total density of states (in detail, see appendix in Ref. [156]): $\rho(E) = \sum_i^N \rho_i(E) = -(1/\pi)\sum_i^N \mathrm{Im}\, G_{ii}(E + i\varsigma)$, where $\rho_i(E)$ is a local DOS (at the i-th site), G_{ii} denotes diagonal elements of the Green's function, the summation is carried over all honeycomb-lattice sites N. Typical value of this coefficient in the calculations without an external magnetic field presen-ce (see, *e.g.*, Refs. [79, 112, 156, 179, 180]) was selected as $\varsigma = 0.05$. However, in case of an external magnetic field impact, ς should be several times smaller ($\varsigma \le 0.01$) so that the LLs be pronouncedly observed on the DOS curves. Therefore DOS curves in Ref. [212] were calculated for smoothing coefficient $\varsigma = 0.01$.

5.2. Shifting of Landau Levels due to Tensile Deformation

Densities of electronic states in (defect-free) graphene simultaneously subjected to the perpendicular magnetic field **B** and uniaxial tensile strain ε are presented in Fig. 45, where B (ε) is fixed (varied) in the figure left (*a*) and varied (fixed) in the figure right (*b*). To detect the uniaxial strain effect, Fig. 45, *a* contains calculated DOS curves in a wide range of relative uniaxial tension $\varepsilon \in [10\%, 27.5\%]$ along both armchair- and zigzag-edge directions in comparison with DOS for unstrained graphene ($\varepsilon = 0$) under the same magnetic field $B = 50$ T. As seen from Fig. 45, *a*, the energy spectrum remains sensitive to the direction of the

stretching as it was revealed in the absence of an external magnetic field [86–88, 96, 97, 100, 104]. The strain along armchair direction causes enhancement in the density of states, while zigzag-type strain results to decrease in DOS. If zigzag strain reaches threshold values of $\varepsilon > 20\%$, the band gap opens and remains more pronounced and even wider than it was revealed in Ref. [104] in the absence of magnetic field **B**. Importantly to stress that this effect (of the band-gap intensification) manifests itself as stronger as the value of B is higher: Fig. 45, *b*.

In Figure 45, *a*, one can see the displacement of all (except $n = 0$ LL) LLs with respect to their positions for the unstrained graphene under the same magnetic field. Independently on direction of the uniaxial tension, the LLs get shifting towards the Dirac point and thus the distance between them decreases. Such a contraction of the LLs was also revealed (within the framework of a geometrical approach) in [201] for uniaxial strains in the smaller range of $\varepsilon \leq 20\%$, where authors explain the LLs spacing reduction by the strain-affected Fermi velocity $\upsilon_F \approx 10^6$ m/s, which is isotropic for the pristine (unstrained) graphene, while becomes anisotropic for the strained one. Such a statement agrees with numerical findings in [188], where the anisotropy of electron mobility and transport was detected in the uniaxially strained doped graphene. Stain-induced contraction of the LLs spectrum indicates decrease of the quantized electron energy E_n. This can be understandable from the following considerations [201]. The uniaxial tension affects a mean radius of the circular electron motion in magnetic field, making the radius and therefore period larger and hence cyclotron frequency ω_c smaller, which results to decrease of the cyclotron orbit energies $E_n \propto \omega_c$ according to Eq. 60. From this point of view, in case of compression of graphene, the displacement of the energy levels (LLs) positions away from the zero ($n = 0$) LL, *i.e.*, increase in the distance between them, is expected [201].

5.3. Smearing and Suppression of Energy Levels by the Point and Line Defects

In case of the δ-like (51) and Gaussian-shaped (53) scattering potentials, their total distributions in Fig. 46, *a*, *b* actually visualize distributions of randomly positioned impurities (scattering centres), while their positions are expectedly smeared for both the alternating-sign ($V \gtrless 0$) and the constant-sign ($V > 0$) long-range (Coulomb) potentials (54) as shown in Fig. 47, *a*, *b*. Our numerical calculations reproduce the LLs positions for pure graphene: see solid curves in Figs. 46, *c* and 47, *d*. Such curves can be also obtained from Eq. (60) appropriable for defect-free graphene.

The presence of different sources (kinds) of disorders affects the LLs profiles: Figs. 46, *c*, *d* and 47, *c*, *d* indicate that increase in degree

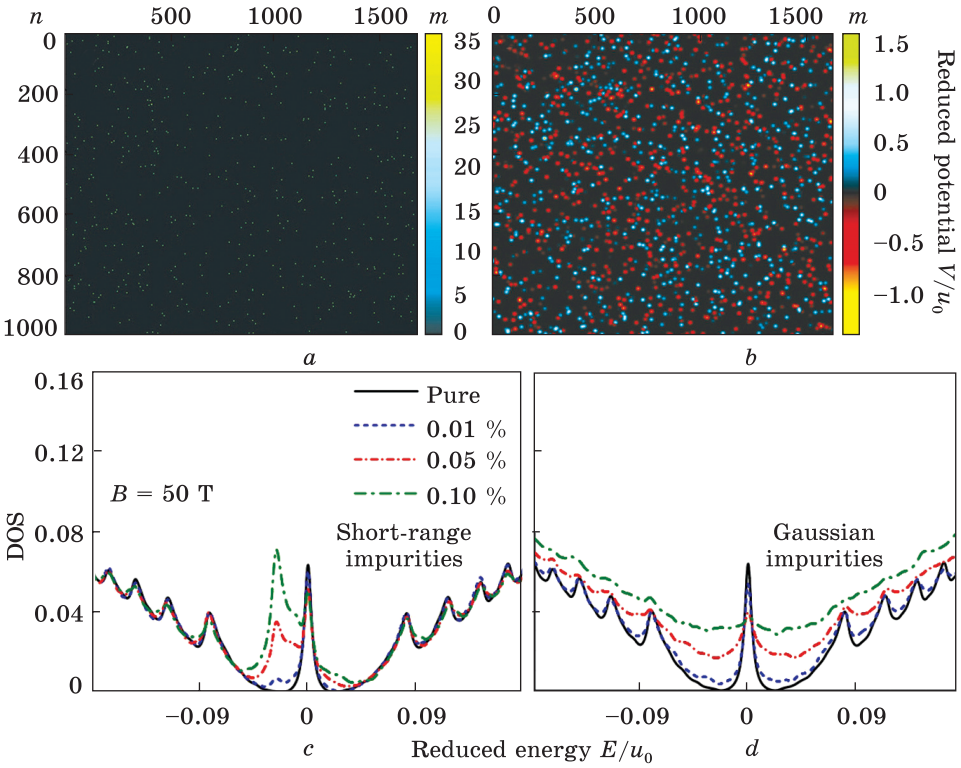

Fig. 46. (*a*, *b*) Scattering potential distributions (for representative impurity content of 0.1%) and (*c*, *d*) and DOS for different concentrations of the (*a*, *c*) strongly short-range (51) and (*b*, *d*) the Gaussian (53) scatterers in graphene under perpendicular magnetic field $B = 50$ T [212]

of disorder reduces the LLs peak amplitudes, makes peaks broader and thereby smears them. However, besides the obvious concentration dependence, such an effect depends on the amplitude (maximal potential height) of the scattering potential and especially on its effective range, *i.e.*, whether impurities manifest themselves as short- or long-range scatterers. Effects of the smearing and suppressing are stronger for the Gaussian scattering potential (with effective potential radius $\xi = 5a_0$) as compared with the on-site δ-like potential, and much more stronger for the Coulomb potential, which is much more long-range ($\propto 1/r$). Since the Coulomb potential (54) is the most long-range among those (51)–(56) we consider here, the DOS curves in Fig. 47, *d* are much more shifted from the neutrality (Dirac) point to the positive-energy (electron) side as compared with DOS in Fig. 46, *d*: *cf.* curves in these figures for the same (0.1%) concentration of positively charged Gaussian and Coulomb impurities. Such a shifting, however, to the negative-energy (hole) side, would appear for the negatively charged Coulomb impurities. That is

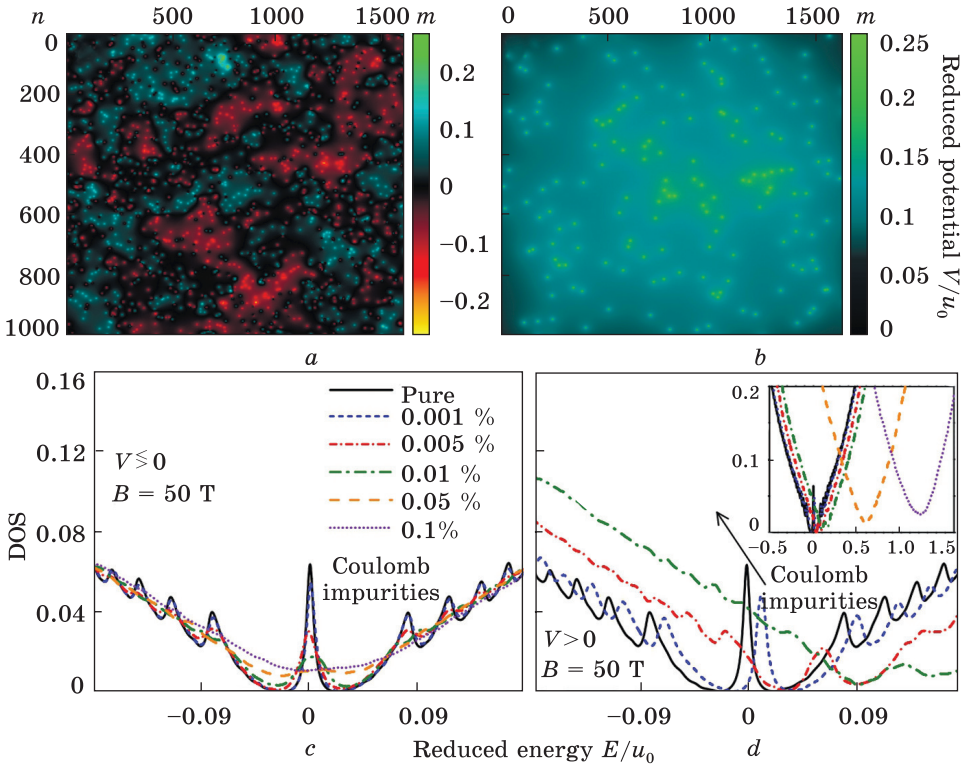

Fig. 47. (*a*, *b*) Scattering-potential distributions and (*c*, *d*) density of states for (*a*, *c*) alternating ($V \lesseqgtr 0$) or (*b*, *d*) strictly positive ($V > 0$) Coulomb potential (54) simulating point impurities (scatterers) in graphene under perpendicular magnetic field B = 50 T [212]. Scattering potential patterns (*a*, *b*) are represented for 0.1% (*a*) and 0.01% (*b*) of impurities

why, for better visualization of the curves, the Coulomb-impurity concentrations in Fig. 47, *c*, *d* are chosen to be smaller as compared to those in Fig. 46, *c*, *d*.

Though, in whole, the DOS curves in Fig. 46, *c* are comparatively lesser altered by defects, one can see the onset of the zero-energy LL splitting into two peaks at a certain concentration of the short-range impurities. Such a splitting was also numerically revealed for resonant (hydrogen) impurities [149], epoxy (O) defects [206], and some other model sources of disorder [214, 215]. The peak at the Dirac point is attributed to original n = 0-th LL, whereas another peak indicates formation of the impurity band: resonant impurities hybridize with C atoms and form their own midgap states [149]. The latter peak is shifted from the E = 0 point due to the positive on-site energy in Eq. (51). Similar peak is also attributable in case of vacancies with the difference that is not shifted but located at a neutrality point thereby contributes to the

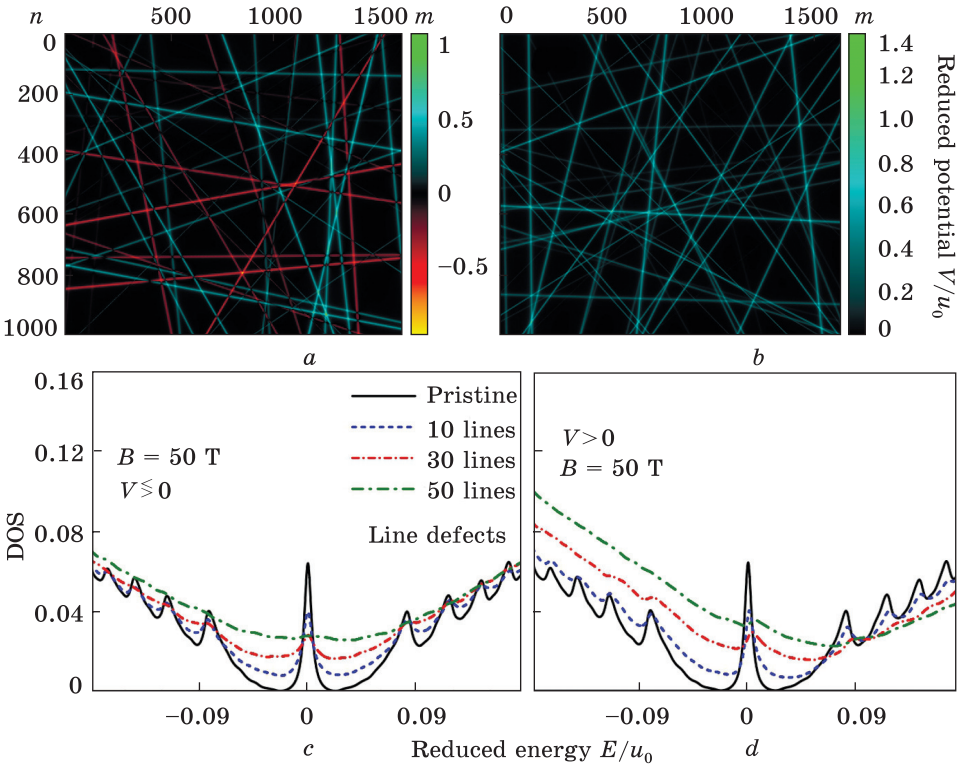

Fig. 48. The same as in the previous figure, but for the scattering potential (56) simulating the charged extended (linear-acting) defects (scatterers) [212]. The representative number of lines for both scattering potential maps (*a*, *b*) is 50

$n = 0$ LL such that the latter is robust with respect to the increasing of the vacancy concentration [149].

Among currently known results on the impact of different kinds of disorder on the LLs in graphene, until recently, there was no one dealing with the extended defects. Thus, the findings in Fig. 48 [212] could not be compared with any other ones (neither theoretical nor experimental results) due to their absence (at least until that time) in the physical literature.

Lorentzian function (56) is a long-range by definition; however, its effective range ($\propto 1/r^2$) is shorter as compared to that ($\propto 1/r$) for the Coulomb potential (11). Spatial distribution of alternation (positive–negative, $V \lesseqgtr 0$) or constant-sign (strictly positive, $V > 0$) scattering potential (56) actually reflects positions of the line defects, which are charged either positively and negatively (Fig. 48, *a*) or positively only (Fig. 48, *b*). As well as the point-like defects, the line ones do not change positions of LLs but also smear and suppress them independently on sign of the scattering potential (56) as Fig. 48, *c*, *d* clearly indicates.

The distinction between the point and line defects concerns only the positively charged Coulomb impurities and line defects: in case of the one-dimensional scatterers, there no such a shifting of the Fermi level and reduced zero-energy LL as for the Coulomb impurities; *cf*. Fig. 47, *d* with Fig. 48, *d*.

In conclusion of this section note that a renewed theory of the electron gas in a magnetic field was relatively recently suggested in Ref. [216], where the author insistently believes that the LLs spectrum (as a result of mathematical mistake) contradicts to the mathematical theorems on the eigenvalues of the Schrödinger equation with a zero boundary condition.

6. Summary and Conclusions

I. As follows from the reviewed literature and the authors' research experience, the problem of computational studying the factors affecting the electronic properties of 2*D* materials turns into a number of tasks have to be solved to achieve the assigned goals. Adequate atomic models are required, within the framework of which the scenarios of a computational experiment have to be developed for providing the relevant data array to determine the functional effects. The method of electron density functional and pseudo-potential from the first principles act as a powerful tool in this respect, as indicate both the independent literature data and own findings of the authors. The analysis of the exhibited (in sections 2 and 3) results made it possible to conclude the following.

• The combination of non-functionalized and functionalized areas of graphene according to a pre-planned pattern in one structure gives controlled changes in electronic properties.

• There is a redistribution of electric charge in the plane of the combined C/CH and C/CF graphene-like structures as well as in the black phosphorene monolayer functionalized with carbamide molecules with the formation of regions of different sign.

• The fluorination process as a functionalization effect causes redistribution of electric charge between certain sections of the combined C/CFH structures with different concentrations of fluorine atoms.

• The impact of static pressure on the combined C/CH structure leads to the rearrangement of the electron density in the direction of the covalent C–H bonds, which causes a change of the electron band gap width. The bending deformation as a functionalization effect leads to an increase of the charge difference in the combined bent C/CH, C/CF, C/CCl structures and to an increase in the width of the band gap as compared to the undeformed ones.

• The band gap of the black phosphorene monolayer depends non-monotonically on the adsorption distance of carbamide molecules, which

affects its conductivity that can be tuned through controlling the localization of adsorbed molecules.

II. Among a series of numerical methods reported in the literature on the studying the electronic and transport properties of single- and multi-layer graphene the time-dependent real-space Kubo–Greenwood formalism is reasonably efficient whereas effortful for the implementation. Such a numerical experiment has a linear dependence of computational capabilities on the size of a system, therefore has an advantage over some other methods on investigation of realistically large graphene sheets containing millions of atoms. The uniform elastic tensile and shear deformations as well as perpendicular magnetic field are introduced by means of the corresponding modifications of hopping terms in the Hamiltonian matrix due to the strain-induced changes in the bond lengths and presence of an external vector potential generating the magnetic field. Different point and line defects are included *via* various on-site scattering potentials appropriate for modelling (un)charged impurity (ad)atoms and extended defects in epitaxial or polycrystalline graphene. Summarizing results interpreted (in sections 4 and 5) within the framework of such a developed methodology, we can conclude as bellow.

• Density of electronic states in the defect-free graphene is sensitive to the strain axis: the stretching along armchair- or zigzag-edge directions result to enhancement or reduction of density of states, respectively, which can be used to affect the competing phenomena associated with a tensile strain and its direction specifically. The band gap opening depends on direction of tensile strain. The presence of randomly distributed point defects does not avoid the minimum threshold zigzag deformations needed for the band-gap formation. Increase in point-defect concentrations acts against the band-gap opening for all defects considered herein, but their impact is different. However, spatially ordered impurities contribute to the band gap manifestation and can reopen the gap that is normally suppressed by the randomly positioned dopants. Band gap varies non-monotonically with strain when zigzag deformation and impurity ordering act simultaneously.

• For random adatomic distribution on hollow (*H*), bridge (*B*), or top (*T*) sites, the conductivity σ depends on their type; if adatoms are correlated, σ is dependent on whether they act as interstitial or substitutional atoms; and finally if adatoms form ordered superlattices with equal periods, σ is practically independent on the adsorption type: $\sigma^H_{\rm rnd} > \sigma^B_{\rm rnd} > \sigma^T_{\rm rnd}$, $\sigma^H_{\rm cor} \approx \sigma^B_{\rm cor} > \sigma^T_{\rm cor}$, and $\sigma^H_{\rm ord} \approx \sigma^B_{\rm ord} \approx \sigma^T_{\rm ord}$, respectively. The conductivity for correlated and ordered adatoms is found to be enhanced in dozens of times as compared to the cases of their random positions. Effect of correlation or ordering becomes more apparent for

adsorbed atoms, which act as substitutional atoms, and weaker for those act as interstitial atoms.

• The calculation of a large set of electronic densities of states (consisting of assemblage of hundreds of DOS curves) enabled to extract information on the bulk spectral gap (if any) and to construct the strain-dependent band-gap maps in a wide range of the deformation tensor parameters (up to 26%, *i.e.* close to the predicted graphene failure limit). Among the obtained results, there are those agree with other theoretical ones for the fixed values of the tensor parameters. However, major part of the calculated results is obtained for the first time, and therefore even cannot be compared with other ones due to their unavailability in the literature. Constructed band-gap maps, covering all possible ranges of the most efficient types of deformations, act as a road map for the strain-induced band gap in graphene, thereby make this work stand out and novel.

• The emergence of a band-gap depends not only on the stress type and rate, but also on the direction of the applied strain. A directional sensitivity is found to be characteristic for both tensile and shear strains as well as for their combination. Besides directional sensitivity, another fingerprint of the strains examined here is its criticality: the gap opening requires a threshold deformation independently of its type (stretching or shearing). Shear deformation along both armchair and zigzag directions, which we referred as a mixed shear strain, can induce a band gap of up to ≈4 eV. Combinations of the uniaxial strain along a preferred (armchair) direction with mixed shear deformation is found to be the most effective for obtaining extra-large gap values: up to ≈6 eV. Both values for strained graphene exceed those of silicon — the most used semi-conductor for devices and integrated circuits.

• The presence of defects can 'transform' the transport (band) gap into the quasi-gap. Strong sensitivity of the strain effects to the direction and ratio of the deformation requires both the strict values and direction of the shear or tensile strain to be kept in an experiment in order to observe the predicted band gap opening. Revised and analysed findings suggest a promising strategy of the combined effect of strains and defects for tailoring electronic and transport properties of graphene and beyond 2*D* materials.

• If a perpendicular magnetic field is applied uniformly to graphene layer, the non-equidistant Landau levels are observed in its energy spectrum. The energy Landau levels are not sensitive to the stretching direction: they undergo the displacement towards the non-shiftable zero-energy level. Therefore, the Landau levels get contraction as the uniaxial strain is applied for any of two considered here orthogonally related directions: along armchair and zigzag honeycomb-lattice edges. Concurrent impacts of the perpendicular magnetic field and zigzag

strain in graphene contribute to the band gap in its energy spectrum: the gap becomes more pronounced and even wider in comparison to that appears due to the zigzag deformation only when there is no any external magnetic field. Both point and extended defects reduces peaks of the Landau levels, broadens, smears and can even suppress the levels depending on a degree of disorders, their strength, and especially effective ranges. The splitting of a zero-energy Landau level for some sources of disorder in graphene is observable in the numerical findings for the strongly short-range-acting defects. One peak at a neutrality point is attributed to the original zero-energy Landau level, whereas another one indicates formation of the impurity band due to the hybridization of resonant impurities with carbon atoms.

Acknowledgements. The first author acknowledges Presidium of the N.A.S. of Ukraine for support within the framework of the program of post-doctoral research in the National Academy of Sciences of Ukraine. Target program for the fundamental research of the N.A.S. of Ukraine 'Prospective fundamental research and innovative development of nanomaterials for the needs of industry, health care, and agriculture' for 2020–2024 is acknowledged. The third and fourth authors obliged for support through the project 'Complex diagnostics of sensitive to strains and defects structural and electronic properties of metallic nanomaterials' (State Reg. No. 0120U102265) within this target program. The first, third, and fourth authors express their gratitude to the National Research Foundation of Ukraine for the grant support (in 2021) within the project Ф81/41600 'Straintronics of imperfect quasi-two-dimensional materials: coplanar *vs* lamellar heterostructures' (State Reg. No. 0121U112812). All authors are grateful to Ihor Sahalianov and Rafael Gutierrez for assistance in numerical calculations and fruitful discussions.

REFERENCES

1. R.W. Siegel, Nanostructured materials -mind over matter-, *Nanostructured Mater.*, **3**, Nos. 1–6: 1 (1993); https://doi.org/10.1016/0965-9773(93)90058-J
2. L.E. Murr, Classifications and structures of nanomaterials, *Handbook of Materials Structures, Properties, Processing and Performance* (Cham: Springer: 2015), p. 719; https://doi.org/10.1007/978-3-319-01815-7_45
3. J.N. Tiwari, R.N. Tiwari, and K.S.Kim, Zero-dimensional, one-dimensional, two-dimensional and three-dimensional nanostructured materials for advanced electrochemical energy devices, *Prog. Mater. Sci.*, **57**, No. 4: 724 (2012); https://doi.org/10.1016/j.pmatsci.2011.08.003
4. J. He, L. Tao, H. Zhang, B. Zhou, and J. Li, Emerging 2D materials beyond graphene for ultrashort pulse generation in fiber lasers, *Nanoscale*, **11**, No. 6: 2577 (2019); https://doi.org/10.1039/C8NR09368G

5. U. Alli, S.J. Hettiarachchi, and S. Kellici, Chemical functionalisation of 2D materials by batch and continuous hydrothermal flow synthesis, *Chem. Eur. J.*, **26**, 29: 6447 (2020);
https://doi.org/10.1002/chem.202000383
6. K.S. Novoselov, A.K. Geim, S.V. Morozov, D. Jiang, Y. Zhang, S.V. Dubonos, I.V. Grigorieva, and A.A. Firsov, Electric field effect in atomically thin carbon films, *Science*, **306**: 666 (2004);
https://doi.org/10.1126/science.1102896
7. N.R. Glavin, R. Rao, V. Varshney, E. Bianco, A. Apte, A. Roy, E. Ringe, and P.M. Ajayan, Emerging applications of elemental 2D materials, *Adv. Mater.*, **32**, No. 7: 1904302 (2020);
https://doi.org/10.1002/adma.201904302
8. R.M. Balabai, A.V. Zdeschyts, and A.G. Lubenets, Spectral and barrier properties of heterocomposites based on poly (para-phenylene) disposed between the silicon films, *Molecular Crystals and Liquid Crystals*, **639**, No. 1: 39 (2016);
https://doi.org/10.1080/15421406.2016.1254513
9. R.M. Balabai and A.G. Lubenets, Lateral junctions based on graphene with different doping regions, *J. Nano- Electron. Phys.*, **9**, No. 5: 05017 (2017);
https://doi.org/10.21272/jnep.9(5).05017
10. R.M. Balabai, O.A. Konoval, and A.G. Solomenko, Photonic and electronic properties of lateral heterostructures based on functionalized graphene under action of static pressure, *Sensor Electron. Microsystem Technol.*, **15**, No. 3: 58 (2018);
https://doi.org/10.18524/1815-7459.2018.3.140397
11. R. Balabai, A. Solomenko, and D. Kravtsova, Electronic and photonic properties of lateral heterostructures based on functionalized graphene depending on the degree of fluorination, *Mol. Cryst. Liquid Cryst.*, **673**, No. 1: 125 (2018);
https://doi.org/10.1080/15421406.2019.1578502
12. R. Balabai and A. Solomenko, Flexible 2D layered material junctions, *Appl. Nanosci.*, **9**: 1011 (2019);
https://doi.org/10.1007/s13204-018-0709-9
13. R.M. Balabai and A.G. Solomenko, Use of the adsorbed organic molecules as dopants for creation of the built-in lateral p-n junctions in a sheet of black phosphorene, *J. Nano- Electron. Phys.*, **11**, No. 5: 05033 (2019);
https://doi.org/10.21272/jnep.11(5).05033
14. T.M. Radchenko, V.A. Tatarenko, and G. Cuniberti, Effects of external mechanical or magnetic fields and defects on electronic and transport properties of graphene, *Mater. Today: Proc.*, **35**, Pt. 4: 523 (2021);
https://doi.org/10.1016/j.matpr.2019.10.014
15. I.Yu. Sahalianov, T.M. Radchenko, V.A. Tatarenko, G. Cuniberti, and Yu.I. Prylutskyy, Straintronics in graphene: extra large electronic band gap induced by tensile and shear strains, *J. Appl. Phys.*, **126**, No. 5: 054302 (2019);
https://doi.org/10.1063/1.5095600
16. I.Yu. Sahalianov, T.M. Radchenko, V.A. Tatarenko, and G. Cuniberti, Sensitivity to strains and defects for manipulating the conductivity of graphene, *EPL*, **132**, No. 4: 48002 (2020);
https://doi.org/10.1209/0295-5075/132/48002
17. W.A. Harrison, *Solid State Theory* (New York: Dover Publications Inc.: 1980).
18. *Theory of the Inhomogeneous Electron Gas* (Eds. S. Lundqvist and N.H. March (New York: Springer Science + Business Media, LLC: 1983).
19. P. Hohenberg and W. Kohn, Inhomogeneous electron gas, *Phys. Rev. B*, **136**: 864 (1964);
https://doi.org/10.1103/PhysRev.136.B864

20. W. Kohn and L.J. Sham, Self-consistent equations including exchange and correlation effects, *Phys. Rev.*, **140**: A1133 (1965);
https://doi.org/10.1103/PhysRev.140.A1133
21. L.Y. Yastrebov and A.A. Katsnelson, *Osnovy Odnoehlektronnoy Teorii Tverdogo Tela* [Fundamentals of the Single-Electron Theory of Solids] (Moscow: Nauka: 1981) (in Russian).
22. N.W. Ashcroft and N.D. Mermin, *Solid State Physics: Revised Edition* (Cengage Learning: 2016).
23. D.R. Hamann, M. Schlьter, and C. Chiang, Norm-conserving pseudopotential, *Phys. Rev. Lett.*, **43**, No. 20: 1494 (1979);
https://doi.org/10.1103/PhysRevLett.43.1494
24. G.B. Bachelet, D.R. Hamann, and M. Schlьter, Pseudopotentials that work: from H to Pu, *Phys. Rev. B*, **26**, No. 8: 4199 (1982);
https://doi.org/10.1103/PhysRevB.26.4199
25. M.V. Ryzhkov, *Novyi Metod Vychisleniya Ehffektivnykh Zaryadov na Atomakh v Molekulakh, Klasterakh i Tverdykh Telakh* [A New Method for Calculating Effective Charges on Atoms in Molecules, Clusters, and Solids] *Zhurnal Strukturnoy Khimii*, **39**, No. 6: 1134 (1998) (in Russian).
26. Y.S. Dmitriev and S.H. Semenov, *Kvantovaya Khimiya — Yeyo Proshloe i Nastoiashchee* [Quantum Chemistry — Its Past and Present] (Moscow: Atomyzdat: 1980) (in Russian).
27. R.M. Aminova, *Osnovy Sovremennoy Kvantovoy Khimii* [Fundamentals of Modern Quantum Chemistry] (Kazan: KazGU: 2004) (in Russian).
28. J. Ihm, A. Zunger, and M.L. Cohen, Momentum-space formalism for the total energy of solids, *J. Phys. C: Solid State Phys.*, **12**, No. 21: 4409 (1979);
https://doi.org/10.1088/0022-3719/12/21/009
29. M.C. Payne, M.P. Teter, D.C. Allan, T.A. Arias, and J.D. Joannopoulos, Iterative minimization techniques for ab initio total-energy calculations: molecular dynamics and conjugate gradients, *Rev. Mod. Phys.*, **64**, No. 4: 1045 (1992);
https://doi.org/10.1103/RevModPhys.64.1045
30. G. Makov, R. Shah, and M.C. Payne, Periodic boundary conditions in ab initio calculations. II. Brillouin-zone sampling for aperiodic systems, *Phys. Rev. B*, **53**, No. 23: 15513 (1996);
https://doi.org/10.1103/PhysRevB.53.15513
31. D.J. Chadi and M.L. Cohen, Special points in the Brillouin zone, *Phys. Rev. B*, **8**, No. 12: 5747 (1973);
https://doi.org/10.1103/PhysRevB.8.5747
32. J.D. Joannopoulos and M.L. Cohen, Electronic properties of complex crystalline and amorphous phases of Ge and Si. I. Density of states and band structures, *Phys. Rev. B*, **7**, No. 6: 2644 (1973);
https://doi.org/10.1103/PhysRevB.7.2644
33. H.J. Monkhorst and J.D. Pack, Special points for Brillouin-zone integrations, *Phys. Rev. B*, **13**, No. 12: 5188 (1976);
https://doi.org/10.1103/PhysRevB.13.5188
34. R.A. Evarestov and V.P. Smirnov, Special points of the Brillouin zone and their use in the solid state theory, *Phys. Status Solidi B*, **119**, No. 1: 9 (1983);
https://doi.org/10.1002/pssb.2221190102
35. D.H. Knorre, L.F. Krylova, and V.S. Muzykantov, *Fizicheskaya Khimiya* [Physical Chemistry] (Moscow: Vysshaya Shkola: 1990) (in Russian).
36. H. Sahin, O. Leenaerts, S.K. Singh, and F.M. Peeters, GraphAne: from synthesis to applications (2015);

https://doi.org/10.48550/arXiv.1502.05804
37. C. Zhou, J. Lou, J. Wang, Q. Yang, C. Liu, D. Huang, and T. Zhu, Graphene's cousin: the present and future of graphane, *Nanoscale Res. Lett.*, **9**: 26 (2014); https://doi.org/10.1186/1556-276X-9-26
38. J.J. Rosas, R.E. Escobedo-Morales, and E. C. Anota, First principles calculations of the electronic and chemical properties of graphene, graphane, and graphene oxide, *J. Mol. Model.*, **17**: 1133 (2011); https://doi.org/10.1007/s00894-010-0818-1
39. F. Karlicky and M. Otyepka, Band gaps and optical spectra of chlorographene, fluorographene and graphane from G_0W_0, GW_0 and GW calculations on top of PBE and HSE06 orbitals, *J. Chem. Theory Comp.*, **9**, No. 9: 4155 (2013); https://doi.org/10.1021/ct400476r
40. D.K. Samarakoon, Z. Chen, C. Nicolas, and X.Q. Wang, Structural and electronic properties of fluorographene, *Small*, **7**, No. 7: 965 (2011); https://doi.org/10.1002/smll.201002058
41. O. Leenaerts, H. Peelaers, A.D. Hernandez-Nieves, B. Partoens, and F.M. Peeters, First-principles investigation of graphene fluoride and graphene, *Phys. Rev. B*, **82**: 195436 (2010); https://doi.org/10.1103/PhysRevB.82.195436
42. H. Sahin, M. Topsakal, and S. Ciraci, Structures of fluorinated graphene and their signatures, *Phys. Rev. B*, **83**: 115432 (2011); https://doi.org/10.1103/PhysRevB.83.115432
43. H. Sahin and S. Ciraci, Chlorine adsorption on graphene: chlorographene, *J. Phys. Chem.*, **116**: 24075 (2012); https://doi.org/10.1021/jp307006c
44. B. Li, L. Zhou, D. Wu, H. Peng, K. Yan, Y. Zhou, and Z. Liu, Photochemical chlorination of graphene, *ACS Nano*, **5**, No. 7: 5957 (2011); https://doi.org/10.1021/nn201731t
45. J.T. Robinson, J.S. Burgess, C.E. Junkermeier, S.C. Badescu, T.L. Reinecke, F.K. Perkins, M.K. Zalalutdniov, J.W. Baldwin, J.C. Culbertson, P.E. Sheehan, and E.S. Snow, Properties of fluorinated graphene films, *Nano Lett.*, **10**: 3001 (2010); https://doi.org/10.1021/nl101437p
46. M.Y. Li, C-H. Chen, Y. Shi, and L-J. Li, Heterostructures based on two-dimensional layered materials and their potential applications, *Mater. Today*, **19**, No. 6: 322 (2015); https://doi.org/10.1016/j.mattod.2015.11.003
47. R. Balog, B. Jшrgensen, L. Nilsson, M. Andersen, E. Rienks, M. Bianchi, M. Fanetti, E. Lжgsgaard, A. Baraldi, S. Lizzit, Z. Sljivancanin, F. Besenbacher, B. Hammer, T.G. Pedersen, P. Hofmann, and L. Hornekжr, Bandgap opening in graphene induced by patterned hydrogen adsorption, *Nature Mater.*, **9**: 315 (2010); https://doi.org/10.1038/nmat2710
48. Ab initio calculation: http://sites.google.com/a/kdpu.edu.ua/calculationphysics
49. S. Das, R. Gulotty, A. Sumant, and A. Roelofs, All two-dimensional, flexible, transparent, and thinnest thin film transistor, *Nano Lett.*, **14**, No. 5: 2861 (2014); https://doi.org/10.1021/nl5009037
50. T. Das and J-H. Ahn, Development of electronic devices based on two-dimensional materials, *Flat Chem.*, **3**: 43 (2017); https://doi.org/10.1016/j.flatc.2017.05.001
51. D. Akinwande, N. Petrone, and J. Hone, Two-dimensional flexible nanoelectronics, *Nat. Commun.*, **5**: 5678 (2014); https://doi.org/10.1038/ncomms6678

52. I. Papadakis, Z. Bouza, and S. Couris, Hydrogenated fluorographene: a 2D counterpart of graphane with enhanced nonlinear optical properties, *J. Phys. Chem.*, **121**: 22567 (2017);
https://doi.org/10.1021/acs.jpcc.7b08470
53. X. Yu, Sh. Zhang, H. Zeng, and Q.J. Wang, Lateral black phosphorene p–n junctions formed via chemical doping for high performance near-infrared photodetector, *Nano Energy*, **25**: 34 (2016);
https://doi.org/10.1016/j.nanoen.2016.04.030
54. R. Frisenda, A.J. Molina-Mendoza, T. Mueller, A. Castellanos-Gomez, and S.J. Herre van der Zant, Atomically thin p–n junctions based on two-dimensional materials, *Chem. Soc. Rev.*, **47**: 3339 (2018);
https://doi.org/10.1039/C7CS00880E
55. J.-H. Yang and B.I. Yakobson, Dimensionality-suppressed chemical doping in 2D semiconductors: the cases of phosphorene, MoS_2, and ReS_2 from first-principles (2017);
https://doi.org/10.48550/arXiv.1711.05094
56. G. Qu, W. Liu, Y. Zhao, J. Gao, T. Xia, J. Shi, L. Hu, W. Zhou, J. Gao, H. Wang, Q. Luo, Q. Zhou, S. Liu, X.F. Yu, and G. Jiang, Improved biocompatibility of black phosphorus nanosheets by chemical modification, *Angew. Chem. Int. Ed.*, **56**: 14488 (2017);
https://doi.org/10.1002%2Fanie.201706228
57. W. Lei, G. Liu, J. Zhang, and M. Liu, Black phosphorus nanostructures: recent advances in hybridization, doping and functionalization, *Chem. Soc. Rev.*, **46**: 3492 (2017);
https://doi.org/10.1039/C7CS00021A
58. S. Feng, Z. Lin, X. Gan, R. Lv, and M. Terrones, Doping two-dimensional materials: ultra-sensitive sensors, band gap tuning and ferromagnetic monolayers, *Nanoscale Horiz.*, **2**: 72 (2017);
https://doi.org/10.1039/C6NH00192K
59. X. Han, C. Liu, J. Sun, A.D. Sendek, and W. Yang, Density functional theory calculations for evaluation of phosphorene as a potential anode material for magnesium batteries, *RSC Adv.*, **8**: 7196 (2018);
https://doi.org/10.1039/C7RA12400G
60. Y. Yi, X.-F. Yu, W. Zhou, J. Wang, and P.K. Chu, Two-dimensional black phosphorus: synthesis, modification, properties, and applications, *Mater. Sci. Eng. R*, **120**: 1 (2017);
https://doi.org/10.1016/j.mser.2017.08.001
61. D.W. Boukhvalov, A.N. Rudenko, D.A. Prishchenko, V.G. Mazurenko, and M.I. Katsnelson, Chemical modifications and stability of phosphorene with impurities: a First principles study, *Phys. Chem. Chem. Phys.*, **17**: 15209 (2015);
https://doi.org/10.1039/C5CP01901J
62. H. Liu, A.T. Neal, Z. Zhu, Z. Luo, X. Xu, D. Tomanek, and P.D. Ye, Phosphorene: an unexplored 2D semiconductor with a high hole mobility, *ACS Nano*, **8**, No. 4: 4033 (2014);
https://doi.org/10.1021/nn501226z
63. K.S. Novoselov, Z. Jiang, Y. Zhang, S.V. Morozov, H.L. Stormer, U. Zeitler, J.C. Maan, G.S. Boebinger, P. Kim, and A.K. Geim, Room-temperature quantum Hall effect in graphene, *Science*, **315**: 1379 (2007);
https://doi.org/10.1126/science.1137201
64. A.H. Castro Neto, F. Guinea, N.M.R. Peres, K.S. Novoselov, and A.K. Geim, The electronic properties of graphene, *Rev. Mod. Phys.*, **81**: 109 (2009);
https://doi.org/10.1103/RevModPhys.81.109

65. R.G. Bai, N. Ninan, K. Muthoosamy, and S. Manickam, Graphene: a versatile platform for nanotheranostics and tissue engineering, *Prog. Mat. Sci.*, **91**: 24 (2018);
https://doi.org/10.1016/j.pmatsci.2017.08.004
66. M. Han, B. Ozyilmaz, Y. Zhang, and Ph. Kim, Energy band-gap engineering of graphene nanoribbons, *Phys. Rev. Lett.*, **98**: 206805 (2007);
https://doi.org/10.1103/PhysRevLett.98.206805
67. J. Bai, X. Zhong, S. Jiang, Yu. Huang, and X. Duan, Graphene nanomesh, *Nature Nanotechnol.*, **5**: 190 (2010);
https://doi.org/10.1038/nnano.2010.8
68. E.V. Castro, K.S. Novoselov, S.V. Morozov, N.M.R. Peres, J.M.B. Lopes dos Santos, J. Nilsson, F. Guinea, A.K. Geim, and A.H. Castro Neto, Biased bilayer graphene: semiconductor with a gap tunable by the electric field effect, *Phys. Rev. Lett.*, **99**: 216802 (2007);
https://doi.org/10.1103/PhysRevLett.99.216802
69. D. Elias, R.R. Nair, T.M.G. Mohiuddin, S.V. Morozov, P. Blake, M.P. Halsall, A.C. Ferrari, D.W. Boukhvalov, M.I. Katsnelson, A.K. Geim, and K.S. Novoselov, Control of graphene's properties by reversible hydrogenation: evidence for graphane, *Science*, **323**: 610 (2009);
https://doi.org/10.1126/science.1167130
70. F. Ouyang, S. Peng, Z. Liu, Z. Liu, and Z. Liu, Bandgap opening in graphene antidot lattices: the missing half, *ACS Nano*, **5**: 4023 (2011);
https://doi.org/10.1021/nn200580w
71. S.Y. Zhou, G.-H. Gweon, A.V. Fedorov, P.N. First, W.A. de Heer, D.-H. Lee, F. Guinea, A.H. Castro Neto, and A. Lanzara, Substrate-induced bandgap opening in epitaxial graphene, *Nature Mater.*, **6**: 770 (2007);
https://doi.org/10.1038/nmat2003
72. G. Giovannetti, P.A. Khomyakov, G. Brocks, P.J. Kelly, and J. van den Brink, Substrate-induced band gap in graphene on hexagonal boron nitride: ab initio density functional calculations, *Phys. Rev. B*, **76**: 079902 (2007);
https://doi.org/10.1103/PhysRevB.76.073103
73. T.M. Radchenko and V.A. Tatarenko, Statistical thermodynamics and kinetics of long-range order in metal-doped graphene, *Solid State Phenom.*, **150**: 43 (2009);
https://doi.org/10.4028/www.scientific.net/SSP.150.43
74. I.Yu. Sagalyanov, I.Yu. Prylutskyy, T.M. Radchenko, and V.A. Tatarenko, Graphene systems: methods of fabrication and treatment, structure formation, and functional properties, *Usp. Fiz. Met.*, **11**, No. 1: 95 (2010);
https://doi.org/10.15407/ufm.11.01.095
75. T.M. Radchenko and V.A. Tatarenko, A statistical-thermodynamic analysis of stably ordered substitutional structures in graphene, *Physica E: Low-Dimensional Systems and Nanostructures*, **42**, No. 8: 2047 (2010);
https://doi.org/10.1016/j.physe.2010.03.024
76. T.M. Radchenko and V.A. Tatarenko, Kinetics of atomic ordering in metal-doped graphene, *Solid State Sci.*, **12**, No. 2: 204 (2010);
https://doi.org/10.1016/j.solidstatesciences.2009.05.027
77. T.M. Radchenko and V.A. Tatarenko, Stable superstructures in a binary honeycomb-lattice gas, *Int. J. Hydrogen Energy*, **36**, No. 1: 1338 (2011);
https://doi.org/10.1016/j.ijhydene.2010.06.112
78. T.M. Radchenko and V.A. Tatarenko, Ordering kinetics of dopant atoms in graphene lattice with stoichiometric compositions of 1/3 and 1/6, *Materialwiss.*

Werkstofftech., **44**, Nos. 2–3: 231 (2013);
https://doi.org/10.1002/mawe.201300094
79. T.M. Radchenko, V.A. Tatarenko, I.Yu. Sagalianov, and Yu.I. Prylutskyy, Effects of nitrogen-doping configurations with vacancies on conductivity in graphene, *Phys. Lett. A*, **378**, Nos. 30–31: 2270 (2014);
https://doi.org/10.1016/j.physleta.2014.05.022
80. I.Yu. Sagalianov, Yu.I. Prylutskyy, T.M. Radchenko, and V.A. Tatarenko, Energies of graphene-based substitutional structures with impurities of nitrogen or boron atoms, *Metallofiz. Noveishie Tekhnol.*, **33**, No. 12: 1569 (2011).
81. I.Y. Sagalianov, Y.I. Prylutskyy, V.A. Tatarenko, T.M. Radchenko, O.O. Sudakov, U. Ritter, P. Scharff, and F. Le Normand, Influence of impurity defects on vibrational and electronic structure of graphene, *Materialwiss. Werkstofftech.*, **44**, Nos. 2–3: 183 (2013);
https://doi.org/10.1002/mawe.201300086
82. S.P. Repetsky, I.G. Vyshyvana, S.P. Kruchinin, and S. Bellucci, Influence of the ordering of impurities on the appearance of an energy gap and on the electrical conductance of graphene, *Sci. Rep.*, **8**, No. 1: 9123 (2018);
https://doi.org/10.1038/s41598-018-26925-0
83. S.P. Repetsky, I.G. Vyshyvana, S.P. Kruchinin, B. Vlahovic, and S. Bellucci, Effects of impurities ordering in the electron spectrum and conductivity ofgraphene, *Phys. Lett. A*, **384**, No. 19: 126401 (2020);
https://doi.org/10.1016/j.physleta.2020.126401
84. Z.H. Ni, T. Yu, Y.H. Lu, Y.Y. Wang, Y.P. Feng, and Z.X. Shen, Uniaxial strain on graphene: raman spectroscopy study and band-gap opening, *ACS Nano*, **2**: 2301 (2008);
https://doi.org/10.1021/nn800459e
85. Z.H. Ni, T. Yu, Y.H. Lu, Y.Y. Wang, Y.P. Feng, and Z.X. Shen, Uniaxial strain on graphene: Raman spectroscopy study and band-gap opening, *ACS Nano*, **3**: 483 (2009);
https://doi.org/10.1021/nn8008323
86. R.M. Ribeiro, V.M. Pereira, N.M.R. Peres, P.R. Briddon, and A.H. Castro Neto, Strained graphene: tight-binding and density functional calculations, *New J. Phys.*, **11**: 115002 (2009);
https://doi.org/10.1088/1367-2630/11/11/115002
87. V.M. Pereira, A.H. Castro Neto, and N.M.R. Peres, Tight-binding approach to uniaxial strain in graphene, *Phys. Rev. B*, **80**: 045401 (2009);
https://doi.org/10.1103/PhysRevB.80.045401
88. V.M. Pereira and A.H. Castro Neto, Strain engineering of graphene's electronic structure, *Phys. Rev. Lett.*, **103**: 046801 (2009);
https://doi.org/10.1103/PhysRevLett.103.046801
89. X. He, L. Gao, N. Tang, J. Duan, F. Mei, Hu Meng, F. Lu, F. Xu, X. Wang, X. Yang, W. Ge, and Bo Shen, Electronic properties of polycrystalline graphene under large local strain. *Appl. Phys. Lett.*, **104**: 243108 (2014);
https://doi.org/10.1063/1.4883866
90. X. He, L. Gao, N. Tang, J. Duan, F. Xu, X. Wang, X. Yang, W. Ge, and B. Shen, Shear strain induced modulation to the transport properties of graphene, *Appl. Phys. Lett.*: **105**: 083108 (2014);
https://doi.org/10.1063/1.4894082
91. G. Cocco, E. Cadelano, and L. Colombo, Gap opening in graphene by shear strain, *Phys. Rev. B*, **81**: 241412 (2010);
https://doi.org/10.1103/PhysRevB.81.241412

92. C. Lee, X. Wei, J.W. Kysar, and J. Hone, Measurement of the elastic properties and intrinsic strength of monolayer graphene, *Science*, **321**: 385 (2008); https://doi.org/10.1126/science.1157996
93. G. Lopez-Polin, C. Gomez-Navarro, V. Parente, F. Guinea, M. I. Katsnelson, F. Perez-Murano, and J. Gomez-Herrero, Increasing the elastic modulus of graphene by controlled defect creation, *Nature Phys.*, **11**: 26 (2015); https://doi.org/10.1038/nphys3183
94. F. Liu, P. Ming, and J. Li, Ab initio calculation of ideal strength and phonon instability of graphene under tension, *Phys. Rev. B*, **76**: 064120 (2007); https://doi.org/10.1103/PhysRevB.76.064120
95. E. Cadelano, P.L. Palla, S. Giordano, and L. Colombo, Nonlinear elasticity of monolayer graphene, *Phys. Rev. Lett.*, **102**: 235502 (2009); https://doi.org/10.1103/PhysRevLett.102.235502
96. B. Amorim, A. Cortijo, F. de Juan, A.G. Grushin, F. Guinea, A. Gutierrez-Rubio, H. Ochoa, V. Parente, R. Roldan, P. San-Jose, J. Schiefele, M. Sturla, and M.A.H. Vozmediano, Novel effects of strains in graphene and other two dimensional materials, *Phys. Rep.*, **617**: 1 (2016); https://doi.org/10.1016/j.physrep.2015.12.006
97. C. Si, Z. Sun, and F. Liu, Strain engineering of graphene: a review, *Nanoscale*, **8**: 3207 (2016); https://doi.org/10.1039/C5NR07755A
98. K.S. Novoselov and A.H. Castro Neto, Two-dimensional crystals-based heterostructures: materials with tailored properties, *Phys. Scr.*, **146**: 014006 (2012); https://doi.org/10.1088/0031-8949/2012/T146/014006
99. G. Gui, J. Li, and J. Zhong, Band structure engineering of graphene by strain: first-principles calculations, *Phys. Rev. B*, **78**: 075435 (2008); https://doi.org/10.1103/PhysRevB.78.075435
100. I.I. Naumov and A.M. Bratkovsky, Gap opening in graphene by simple periodic inhomogeneous strain, *Phys. Rev. B*, **84**: 245444 (2011); https://doi.org/10.1103/PhysRevB.84.245444
101. N. Kerszberg and P. Suryanarayana, Ab initio strain engineering of graphene: opening bandgaps up to 1 eV, *RSC Adv.*, **5**: 43810 (2015); https://doi.org/10.1039/C5RA03422A
102. F. Guinea, M.I. Katsnelson, and A.K. Geim, *Nature Phys.*, **6**: 30 (2010); https://doi.org/10.1038/nphys1420
103. T. Low, F. Guinea, and M.I. Katsnelson, Energy gaps and a zero-field quantum Hall effect in graphene by strain engineering, *Phys. Rev. B*, **83**: 195436 (2011); https://doi.org/10.1103/PhysRevB.83.195436
104. I.Yu. Sagalianov, T.M. Radchenko, Yu.I. Prylutskyy, V.A. Tatarenko, and P. Szroeder, Mutual influence of uniaxial tensile strain and point defect pattern on electronic states in graphene, *Eur. Phys. J. B*, **90**, No. 6: 112 (2017); https://doi.org/10.1140/epjb/e2017-80091-x
105. T.M. Radchenko, I.Yu. Sahalianov, V.A. Tatarenko, Yu.I. Prylutskyy, P. Szroeder, M. Kempiński, and W. Kempiński, Strain- and adsorption-dependent electronic states and transport or localization in graphene, *Springer Proceedings in Physics: Nanooptics, Nanophotonics, Nanostructures, and Their Applications* (Eds. O. Fesenko and L. Yatsenko) (Cham, Switzerland: Springer: 2018), Vol. **210**, Ch. 3, p. 25; https://doi.org/10.1007/978-3-319-91083-3_3
106. T.M. Radchenko, V.A. Tatarenko, V.V. Lizunov, V.B. Molodkin, I.E. Golentus, I.Yu. Sahalianov, and Yu.I. Prylutskyy, Defect-pattern-induced fingerprints in

the electron density of states of strained graphene layers: diffraction and simulation methods, *Phys. Status Solidi B*, **256**, No. 5: 1800406 (2019); https://doi.org/10.1002/pssb.201800406
107. A. Lugo-Solis and I. Vasiliev, Ab initio study of K adsorption on graphene and carbon nanotubes: role of long-range ionic forces, *Phys. Rev. B*, **76**: 235431 (2007); https://doi.org/10.1103/PhysRevB.76.235431
108. K.T. Chan, J.B. Neaton, and M.L. Cohen, First-principles study of metal adatom adsorption on graphene, *Phys. Rev. B*, **77**: 235430 (2008); https://doi.org/10.1103/PhysRevB.77.235430
109. M. Wu, E.-Z. Liu, M.Y. Ge, and J.Z. Jiang, Stability, electronic, and magnetic behaviors of Cu adsorbed graphene: a first-principles study, *Appl. Phys. Lett.*, **94**: 102505 (2009); https://doi.org/10.1063/1.3097013
110. C. Cao, M. Wu, K. Jiang, and H.-P. Cheng, Transition metal adatom and dimer adsorbed on graphene: Induced magnetization and electronic structures, *Phys. Rev. B*, **81**: 205424 (2010); https://doi.org/10.1103/PhysRevB.81.205424
111. K. Nakada and A. Ishii, Migration of adatom adsorption on graphene using DFT calculation, *Solid State Commun.*, **151**, No. 1: 13 (2010); https://doi.org/10.1016/j.ssc.2010.10.036
112. T.M. Radchenko, V.A. Tatarenko, I.Yu. Sagalianov, Yu.I. Prylutskyy, P. Szroeder, and S. Biniak, On adatomic-configuration-mediated correlation between electrotransport and electrochemical properties of graphene, *Carbon*, **101**: 37 (2016); https://doi.org/10.1016/j.carbon.2016.01.067
113. T.M. Radchenko, I.Yu. Sahalianov, V.A. Tatarenko, Yu.I. Prylutskyy, P. Szroeder, M. Kempiński, and W. Kempiński, The impact of uniaxial strain and defect pattern on magnetoelectronic and transport properties of graphene, *Handbook of Graphene: Growth, Synthesis, and Functionalization* (Eds. E. Celasco and A. Chaika) (Beverly, MA: Scrivener Publishing LLC: 2019), Vol. **1**, Ch. 14, p. 451; https://doi.org/10.1002/9781119468455.ch14
114. F. Banhart, J. Kotakoski, and A.V. Krasheninnikov, Structural defects in graphene, *ACS Nano*, **5**: 26 (2011); https://doi.org/10.1021/nn102598m
115. N. Blanc, F. Jean, A.V. Krasheninnikov, G. Renaud, and J. Coraux, Strains induced by point defects in graphene on a metal, *Phys. Rev. Lett.*, **111**: 085501 (2013); https://doi.org/10.1103/PhysRevLett.111.085501
116. Y. Ren and G. Cao, Effect of geometrical defects on the tensile properties of graphene, *Carbon*, **103**: 125 (2016); https://doi.org/10.1016/j.carbon.2016.03.017
117. X. He, Q.S. Bai, and J.X. Bai, Molecular dynamics study of the tensile mechanical properties of polycrystalline graphene, *Acta Phys. Sinica*, **65**, No. 11: 116101 (2016); https://doi.org/10.7498/aps.65.116101
118. M.A.H. Vozmediano, M.I. Katsnelson, and F. Guinea, Gauge fields in graphene, *Phys. Rep.*, **496**, Nos: 4–5: 109 (2010); https://doi.org/10.1016/j.physrep.2010.07.003
119. D.O. Rybalka, E.V. Gorbar, and V.P. Gusynin, Gap generation and phase diagram in strained graphene in a magnetic field, *Phys. Rev. B*, **91**: 115132 (2015); https://doi.org/10.1103/PhysRevB.91.115132

120. V.O. Shubnyi and S.G. Sharapov, Density of states of Dirac–Landau levels in a gapped graphene monolayer under strain gradient, *Low Temp. Phys.*, **43**: 1202 (2017); https://doi.org/10.1063/1.5008413
121. Y.V. Skrypnyk and V.M. Loktev, Electronic properties of graphene with point defects, *Low Temp. Phys.*, **44**, No. 11: 1112 (2018); https://doi.org/10.1063/1.5060964
122. Y.V. Skrypnyk and V.M. Loktev, Electronic properties of graphene with point defects (review article), *Low Temp. Phys.*, **45**, No. 12: 1310 (2019); https://doi.org/10.1063/10.0000565
123. S. Bellucci, S. Kruchinin, S.P. Repetsky, I.G. Vyshyvana, and R. Melnyk, Behaviour of the energy spectrum and electric conduction of doped graphene, *Materials*, **13**, No. 7: 1718 (2020); https://doi.org/10.3390/ma13071718
124. S.P. Repetsky, I.G. Vyshyvana, S.P. Kruchinin, R.M. Melnyk, and A.P. Polishchuk, The energy spectrum and the electrical conductivity of graphene with substitution impurity, *Condens. Matter Phys.*, **23**, No. 1: 13704 (2020); https://doi.org/10.5488/CMP.23.13704
125. S.P. Repetsky, I.G. Vyshyvana, S.P. Kruchinin, V.B. Molodkin, and V.V. Lizunov, Influence of the adsorbed atoms of potassium on an energy spectrum of graphene, *Metallofiz. Noveishie Tekhnol.*, **39**, No. 8: 1017 (2017); https://doi.org/10.15407/mfint.39.08.1017
126. A. Mishra and V.A. Singh, Universal features of point defect spectrum in graphene, *Phys. Let. A*, **430**: 127971 (2022); https://doi.org/10.1016/j.physleta.2022.127971
127. M.V. Kondrin, Y.B. Leded, and V.V. Brazhkin, Extended defects in graphene and their contribution to the excess specific heat at high temperatures *Phys. Rev. Lett.*, **126**: 165501 (2021); https://doi.org/10.1103/PhysRevLett.126.165501
128. J. Lahiri, Y. Lin, P. Bozkurt, I.I. Oleynik, and M. Batzill, An extended defect in graphene as a metallic wire, *Nature Nanotechnol.*, **5**: 326 (2010); https://doi.org/10.1038/NNANO.2010.53
129. L.A. Jauregui, H. Cao, W. Wu, Q. Yu, Y.P. Chen, Electronic properties of grains and grain boundaries in graphene grown by chemical vapor deposition, *Solid State Commun.*, **151**: 1100 (2011); https://doi.org/10.1016/j.ssc.2011.05.023
130. A.W. Tsen, L. Brown, M.P. Levendorf, F. Ghahari, P.Y. Huang, R.W. Havener, C.S. Ruiz-Vargas, D.A. Muller, P. Kim, and J. Park, Tailoring electrical transport across grain boundaries in polycrystalline graphene, *Science*, **336**: 1143 (2012); https://doi.org/10.1126/science.1220527
131. T.M. Radchenko, V.A. Tatarenko, I.Yu. Sagalianov, and Yu.I. Prylutskyy, Configurations of structural defects in graphene and their effects on its transport properties, *Graphene: Mechanical Properties, Potential Applications and Electrochemical Performance* (Ed. B.T. Edwards) (New York: Nova Science Publishers: 2014), Ch. 7, p. 219; https://novapublishers.com/shop/graphene-mechanical-properties-potential-applications-and-electrochemical-performance
132. M.I. Katsnelson, *Graphene: Carbon in Two Dimensions* (New York: Cambridge University Press: 2012); https://doi.org/10.1017/CBO9781139031080
133. P. Szroeder, I.Yu. Sagalianov, T.M. Radchenko, V.A. Tatarenko, Yu.I. Prylutskyy, and W. Strupiński, Effect of uniaxial stress on the electrochemical properties

of graphene with point defects, *Appl. Surf. Sci.*, **442**: 185 (2018); https://doi.org/10.1016/j.apsusc.2018.02.150
134. P. Szroeder, I. Sahalianov, T. Radchenko, V. Tatarenko, and Yu. Prylutskyy, The strain- and impurity-dependent electron states and catalytic activity of graphene in a static magnetic field, *Optical Mater.*, **96**: 109284 (2019); https://doi.org/10.1016/j.optmat.2019.109284
135. P. Szroeder, I. Sahalianov, and T. Radchenko, Tuning the electron band structure of graphene for optoelectronics, *IEEE 2019 Int. Conf. on Transparent Optical Networks (ICTON-2019)*, p. 8840470; https://doi.org/10.1109/ICTON.2019.8840470
136. A.H. Castro Neto, V.N. Kotov, J. Nilsson, V.M. Pereira, N.M.R. Peres, and B. Uchoa, Adatoms in graphene, *Solid State Commun.*, **149**, Nos. 27–28: 1094 (2009); https://doi.org/10.1016/j.ssc.2009.02.040
137. J. Yan and M.S. Fuhrer, Correlated charged impurity scattering in graphene, *Phys. Rev. Lett.*, **107**: 206601 (2011); https://doi.org/10.1103/PhysRevLett.107.206601
138. V.V. Cheianov, O. Syljuesen, B.L. Altshuler, and V.I. Fal'ko, Sublattice ordering in a dilute ensemble of monovalent adatoms on graphene, *EPL*, **89**, No. 5: 56003 (2010); https://doi.org/10.1209/0295-5075/89/56003
139. V.V. Cheianov, O. Syljuasen, B.L. Altshuler, and V.I. Fal'ko, Ordered states of adatoms on graphene, *Phys. Rev. B*, **80**: 233409 (2009); https://doi.org/10.1103/PhysRevB.80.233409
140. V.V. Cheianov, V.I. Fal'ko, O. Syljuasen, and B.L. Altshuler, Hidden Kekulé ordering of adatoms on graphene, *Solid State Commun.*, **149**, Nos. 37–38: 1499 (2009); https://doi.org/10.1016/j.ssc.2009.07.008
141. C.A. Howard, M.P. M. Dean, and F. Withers, Phonons in potassium-doped graphene: the effects of electron-phonon interactions, dimensionality, and adatom ordering, *Phys. Rev. B*, **84**: 241404 (2011); https://doi.org/10.1103/PhysRevB.84.241404
142. C.-L. Song, B. Sun, Y.-L. Wang, Y.-P. Jiang, L. Wang, K. He, X. Chen, P. Zhang, X.-C. Ma, and Q.-K. Xue, Charge-transfer-induced cesium superlattices on graphene, *Phys. Rev. Lett.*, **108**: 156803 (2012); https://doi.org/10.1103/PhysRevLett.108.156803
143. D.M. Eigler and E.K. Schweizer, Positioning single atoms with a scanning tunnelling microscope, *Nature*, **344**: 524 (1990); https://doi.org/10.1038/344524a0
144. J.C. Meyer, C.O. Girit, M.F. Crommie, and A. Zettl, Imaging and dynamics of light atoms and molecules on graphene, *Nature*, **454**: 319 (2008); https://doi.org/10.1038/nature07094
145. C. Lin, Y. Feng, Y. Xiao, M. Dürr, X. Huang, X. Xu, R. Zhao, E. Wang, X.-Z. Li, and Z. Hu, Direct observation of ordered configurations of hydrogen adatoms on graphene, *Nano Lett.*, **15**: 903 (2015); https://doi.org/10.1021/nl503635x
146. O. Madelung, *Introduction to Solid-State Theory* (Derlin: Springer: 1996).
147. S. Roche, N. Leconte, F. Ortmann, A. Lherbier, D. Soriano, and J.-Ch. Charlier, Quantum transport in disordered graphene: a theoretical perspective, *Solid State Commun.*, **153**, No. 15: 1404 (2012); https://doi.org/10.1016/j.ssc.2012.04.030

148. A.R. Botello-Méndez, A. Lherbier, and J.-C. Charlier, Modeling electronic properties and quantum transport in doped and defective graphene, *Solid State Commun.*, **175–176**: 90 (2013); https://doi.org/10.1016/j.ssc.2013.08.029
149. S. Yuan, H. De Raedt, and M.I. Katsnelson, Modeling electronic structure and transport properties of graphene with resonant scattering centers, *Phys. Rev. B*, **82**: 115448 (2010); https://doi.org/10.1103/PhysRevB.82.115448
150. S. Yuan, H. De Raedt, and M.I. Katsnelson, Electronic transport in disordered bilayer and trilayer graphene, *Phys. Rev. B*, **82**: 235409 (2010); https://doi.org/10.1103/PhysRevB.82.235409
151. M.S. Dresselhaus and G. Dresselhaus, Intercalation compounds of graphite, *Adv. Phys.*, **30**, No. 2: 139 (1981); https://doi.org/10.1080/00018738100101367
152. J.W. McClure, Band structure of graphite and de Haas-van Alphen effect, *Phys. Rev.*, **108**: 612 (1957); https://doi.org/10.1103/PhysRev.108.612
153. J.C. Slonczewski and P.R. Weiss, Band structure of graphite, *Phys. Rev.*, **109**: 272 (1958); https://doi.org/10.1103/PhysRev.109.272
154. N. Leconte, A. Lherbier, F. Varchon, P. Ordejon, S. Roche, and J.-C. Charlier, Quantum transport in chemically modified two-dimensional graphene: from minimal conductivity to Anderson localization, *Phys. Rev. B*, **84**: 235420 (2011); https://doi.org/10.1103/PhysRevB.84.235420
155. A. Lherbier, Simon M.-M. Dubois, X. Declerck, Y.-M. Niquet, S. Roche, and J.-Ch. Charlier, Transport properties of graphene containing structural defects, *Phys. Rev. B*, **86**: 075402 (2012); https://doi.org/10.1103/PhysRevB.86.075402
156. T.M. Radchenko, A.A. Shylau, and I.V. Zozoulenko, Influence of correlated impurities on conductivity of graphene sheets: time-dependent real-space Kubo approach, *Phys. Rev. B*, **86**, No. 3: 035418 (2012); https://doi.org/10.1103/PhysRevB.86.035418
157. B. Burgos, J. Warnes, L.R.F. Leandro Lima, and C. Lewenkopf, Effects of a random gauge field on the conductivity of graphene sheets with disordered ripples, *Phys. Rev. B*, **91**: 115403 (2015); https://doi.org/10.1103/PhysRevB.91.115403
158. N. Leconte, A. Ferreira, and J. Jung, Efficient multiscale lattice simulations of strained and disordered graphene, *Semiconduct. Semimet.*, **95**: 35 (2015); https://doi.org/10.1016/bs.semsem.2016.04.002
159. A.H. Castro Neto and F. Guinea, Electron-phonon coupling and Raman spectroscopy in graphene, *Phys. Rev. B*, **75**: 045404 (2007); https://doi.org/10.1103/PhysRevB.75.045404
160. L. Blakslee, D.G. Proctor, E.J. Seldin, G.B. Stence, and T. Wen, Elastic constants of compression-annealed pyrolytic graphite, *J. Appl. Phys.*, **41**,No. 8: 3373 (1970); https://doi.org/10.1063/1.1659428
161. M. Farjam and H. Rafii-Tabar, Comments on 'Band structure engineering of graphene by strain: first-principle calculations', *Phys. Rev. B*, **80**: 167401 (2009); https://doi.org/10.1103/PhysRevB.80.167401
162. L.M. Sandonas, R. Gutierrez, A. Pecchia, A. Dianat, and G. Cuniberti, Thermoelectric properties of functionalized graphene grain boundaries, *J. Self-Assembly Molecular Electron.*, **3**: 1 (2015); https://doi.org/10.13052/jsame2245-4551.2015007

163. P.-L. Zhao, S. Yuan, M.I. Katsnelson, and H. De Raedt, Fingerprints of disorder source in graphene, *Phys. Rev. B*, **92**: 045437 (2015); https://doi.org/10.1103/PhysRevB.92.045437
164. J.P. Robinson, H. Schomerus, L. Oroszlány, and V.I. Fal'ko, Adsorbate-limited conductivity of graphene, *Phys. Rev. Lett.*, **101**: 196803 (2008); https://doi.org/10.1103/PhysRevLett.101.196803
165. T.O. Wehling, S. Yuan, A.I. Lichtenstein, A.K. Geim, and M.I. Katsnelson, Resonant scattering by realistic impurities in graphene, *Phys. Rev. Lett.*, **105**: 056802 (2010); https://doi.org/10.1103/PhysRevLett.105.056802
166. S. Ihnatsenka and G. Kirczenow, Nonlinear conductance quantization in graphene ribbons, *Phys. Rev. B*, **83**: 245442 (2011); https://doi.org/10.1103/PhysRevB.83.245431
167. A. Ferreira, J. Viana-Gomes, J. Nilsson, E.R. Mucciolo, N.M.R. Peres, and A.H. Castro Neto, Unified description of the dc conductivity of monolayer and bilayer graphene at a finite densities based on resonant scatterers, *Phys. Rev. B*, **83**: 165402 (2011); https://doi.org/10.1103/PhysRevB.83.165402
168. N.M.R. Peres, A.H. Castro Neto, and F. Guinea, Conductance quantization in mesoscopic graphene, *Phys. Rev. B*, **73**: 195411 (2006); https://doi.org/10.1103/PhysRevB.73.195411
169. X.F. Fan, W.T. Zheng, V. Chihaia, Z.X. Shen, and J.-L. Kuo, Interaction between graphene and the surface of SiO_2, *J. Phys.: Condens. Matter.*, **24**, No. 30: 305004 (2002); https://doi.org/10.1088/0953-8984/24/30/305004
170. A. Dianat, Z. Liao, M. Gall, T. Zhang, R. Gutierrez, E. Zschech, and G. Cuniberti, Doping of graphene induced by boron/silicon substrate, *Nanotechnology*, **28**, No. 21: 215701 (2017); https://doi.org/10.1088/1361-6528/aa6ce9
171. H. Kuramochi, S. Odaka, K. Morita, S. Tanaka, H. Miyazaki, M.V. Lee, S.-L. Li, H. Hiura, and K. Tsukagoshi, Role of atomic terraces and steps in the electron transport properties of epitaxial graphene grown on SiC, *AIP Adv.*, **2**: 012115 (2012); https://doi.org/10.1063/1.3679400
172. S. Günther, S. Dänhardt, B. Wang, M.-L. Bocquet, S. Schmitt, and J. Wintterlin, Single terrace growth of graphene on a metal surface, *Nano Lett.*, **11**: 1895 (2011); https://doi.org/10.1021/nl103947x
173. F. Gargiulo and O.V. Yazyev, Topological aspects of charge-carrier transmission across grain boundaries in graphene, *Nano Lett.*, **14**: 250 (2014); https://doi.org/10.1021/nl403852a
174. H. Zhang, G. Lee, C. Gong, L. Colombo, and K. Cho, Grain boundary effect on electrical transport properties of graphene, *J. Phys. Chem. C*, **118**: 2338 (2014); https://doi.org/10.1021/jp411464w
175. O.V. Yazyev and S.G. Louie, Electronic transport in polycrystalline graphene, *Nat. Mater.*, **9**: 806 (2010); https://doi.org/10.1038/nmat2830
176. G.-X. Ni, Y. Zheng, S. Bae, H.R. Kim, A. Pachoud, Y.S. Kim, Ch.-L. Tan, D. Im, J.-H. Ahn, B.H. Hong, and B. Özyilmaz, Quasi-periodic nanoripples in graphene grown by chemical vapor deposition and its impact on charge transport, *ACS Nano*, **6**: 1158 (2012); https://doi.org/10.1021/nn203775x

177. D. Zhang, Z. Jin, J. Shi, P. Ma, S. Peng, X. Liu, and T. Ye, The anisotropy of field effect mobility of CVD graphene grown on copper foil, *Small*, **10**: 1761 (2014);
https://doi.org/10.1002/smll.201303195
178. A. Ferreira, X. Xu, C.-L. Tan, S.-K. Bae, N.M.R. Peres, B.-H. Hong, B. Ozyilmaz, and A.H. Castro, Transport properties of graphene with one-dimensional charge defects, *EPL*, **94**, No. 2: 28003 (2011);
https://doi.org/10.1209/0295-5075/94/28003
179. T.M. Radchenko, A.A. Shylau, I.V. Zozoulenko, and A. Ferreira, Effect of charged line defects on conductivity in graphene: numerical Kubo and analytical Boltzmann approaches, *Phys. Rev. B*, **87**, No. 19: 195448 (2013);
https://doi.org/10.1103/PhysRevB.87.195448
180. T.M. Radchenko, A.A. Shylau, and I.V. Zozoulenko, Conductivity of epitaxial and CVD graphene with correlated line defects, *Solid State Commun.*, **195**: 88 (2014);
https://doi.org/10.1016/j.ssc.2014.07.012
181. Ch. Held, T. Seyller, and R. Bennewitz, Quantitative multichannel NC-AFM data analysis of graphene growth on SiC(0001), *Beilstein J. Nanotechnol.*, **3**: 179 (2012);
https://doi.org/10.3762/bjnano.3.19
182. S.-H. Ji, J.B. Hannon, R.M. Tromp, V. Perebeinos, J. Tersoff, and F.M. Ross, Atomic-scale transport in epitaxial graphene, *Nature Mater.*, **11**: 114 (2012);
https://doi.org/10.1038/nmat3170
183. W. Wang, K. Munakata, M. Rozler, and M.R. Beasley, Local transport measurements at mesoscopic length scales using scanning tunneling potentiometry, *Phys. Rev. Lett.*, **110**: 236802 (2013);
https://doi.org/10.1103/PhysRevLett.110.236802
184. Ch. Adessi, S. Roche, and X. Blase, Reduced backscattering in potassium-doped nanotubes: ab initio and semiempirical simulations, *Phys. Rev. B*, **73**: 125414 (2006);
https://doi.org/10.1103/PhysRevB.73.125414
185. Q. Li, E.H. Hwang, E. Rossi, and S. Das Sarma, Theory of 2D transport in graphene for correlated disorder, *Phys. Rev. Lett.*, **107**, No. 15: 156601 (2011);
https://doi.org/10.1103/PhysRevLett.107.156601
186. Q. Li, E.H. Hwang, and E. Rossi, Theory of 2D transport in graphene for correlated disorder, *Solid State Commun.*, **152**: 1390 (2012);
https://doi.org/10.1016/j.ssc.2012.04.053
187. G. Gui, D. Morgan, J. Booske, J. Zhong, and Z. Ma, Local strain effect on the band gap engineering of graphene by a first-principles study, *Appl. Phys. Lett.*, **106**: 053113 (2015);
https://doi.org/10.1063/1.4907410
188. I.Yu. Sagalianov, Yu.I. Prylutskyy, T.M. Radchenko, and V.A. Tatarenko, Effect of weak impurities on conductivity of uniaxially strained graphene, *IEEE 2017 Int. Young Scientists Forum on Applied Physics and Engineering (YSF-2017)*, p. 8126607-151;
https://doi.org/10.1109/YSF.2017.8126607
189. A. Lherbier, A.R. Botello-Mendez, and J.C. Charlier, Electronic and transport properties of unbalanced sublattice N-doping in graphene, *Nano Lett.*, **13**: 1446 (2013);
https://doi.org/10.1021/nl304351z
190. D.M.A. Mackenzie, M. Galbiati, X.D. de Cerio, I.Y. Sahalianov, T.M. Radchenko, J. Sun, D. Peña, L. Gammelgaard, B.S. Jessen, J.D. Thomsen, P. Bøggild,

A. Garcia-Lekue, L. Camilli, and J.M. Caridad, Unraveling the electronic properties of graphene with substitutional oxygen, *2D Mater.*, **8**, No. 4: 045035 (2021);
https://doi.org/10.1088/2053-1583/ac28ab

191. J.-H. Chen, C. Jang, S. Adam, M.S. Fuhrer, E.D. Williams, and M. Ishigami, Charged-impurity scattering in graphene, *Nature Phys.*, **4**: 377 (2008);
https://doi.org/10.1038/nphys935
192. N.M.R. Peres, The transport properties of graphene: an introduction, *Rev. Mod. Phys.*, **82**: 2673 (2010);
https://doi.org/10.1103/RevModPhys.82.2673
193. S. Souma, Y. Ohmi, and M. Ogawa, Effect of lateral strain on gate induced control of electrical conduction in single layer graphene device, *J. Comput. Electron.*, **12**: 170 (2013);
https://doi.org/10.1007/s10825-013-0451-1
194. Y. Hasegawa, R. Konno, H. Nakano, and M. Kohmoto, Zero modes of tight-binding electrons on the honeycomb lattice, *Phys. Rev. B*, **74**: 033413 (2006);
https://doi.org/10.1103/PhysRevB.74.033413
195. O.V. Yazyev and Y.P. Chen, Polycrystalline graphene and other two-dimensional materials, *Nature Nanotechnol.*, **9**: 755 (2014);
https://doi.org/10.1038/nnano.2014.166
196. D.S.L. Abergel, V. Apalkov, J. Berashevich, K. Ziegler, and T. Chakraborty, Properties of graphene: a theoretical perspective, *Adv. Phys.*, **59**: 261 (2010);
https://doi.org/10.1080/00018732.2010.487978
197. M. Orlita, W. Escoffier, P. Plochocka, B. Raquet, and U. Zeitler, Graphene in high magnetic fields, *C. R. Physique*, **14**: 78 (2013);
https://doi.org/10.1016/j.crhy.2012.11.003
198. F. Chiappini, S. Wiedmann, M. Titov, A.K. Geim, R.V. Gorbachev, E. Khestanova, A. Mishchenko, K.S. Novoselov, J.C. Maan, and U. Zeitler, Magnetotransport in single-layer graphene in a large parallel magnetic field, *Phys. Rev. B*, **94**: 085302 (2016);
https://doi.org/10.1103/PhysRevB.94.085302
199. K.S. Novoselov, A.K. Geim, S.V. Morozov, D. Jiang, M.I. Katsnelson, I.V. Grigorieva, S.V. Dubonos, and A.A. Firsov, Two-dimensional gas of massless Dirac fermions in graphene, *Nature*, **438**: 197 (2005);
https://doi.org/10.1038/nature04233
200. Y. Zhang, Y.-W. Tan, H.L. Stormer, and P. Kim, Experimental observation of the quantum Hall effect and Berry's phase in graphene, *Nature*, **438**: 201 (2005);
https://doi.org/10.1038/nature04235
201. Y. Betancur-Ocampo, M.E. Cifuentes-Quintal, G. Cordourier-Maruri, and R. de Coss, Landau levels in uniaxially strained graphene: a geometrical approach, *Ann. Phys.*, **359**: 243 (2015);
https://doi.org/10.1016/j.aop.2015.04.026
202. S.V. Vonsovsky and M.I. Katsnelson, *Quantum Solid State Physics* (Berlin: Springer: 1989);
https://doi.org/10.1007/978-3-642-50164-7
203. M.O. Goerbig, Electronic properties of graphene in a strong magnetic field, *Rev. Mod. Phys.*, **83**: 1193 (2011);
https://doi.org/10.1103/RevModPhys.83.1193
204. V.P. Gusynin and S.G. Sharapov, Magnetic oscillations in planar systems with the Dirac-like spectrum of quasiparticle excitations. II. Transport properties,

Phys. Rev. B, **71**: 125124 (2005);
https://doi.org/10.1103/PhysRevB.71.125124
205. M.I. Katsnelson, Graphene: carbon in two dimensions, *Mater. Today*, **10**: 20 (2007);
https://doi.org/10.1016/S1369-7021(06)71788-6
206. N. Leconte, F. Ortmann, A. Cresti, J.-Ch. Charlier, and S. Roche, *2D Mater.*, **1**: 021001 (2014);
https://doi.org/10.1088/2053-1583/1/2/021001
207. L.-J. Yin, K.-K. Bai, W.-X. Wang, Y. Zhang, and L. He, Landau quantization of Dirac fermions in graphene and its multilayers, *Front. Phys.*, **12**: 127208 (2017);
https://doi.org/10.1007/s11467-017-0655-0
208. J.W. McClure, Diamagnetism of graphite, *Phys. Rev.*, **104**: 666 (1956);
https://doi.org/10.1103/PhysRev.104.666
209. J.W. McClure, Theory of diamagnetism of graphite, *Phys. Rev.*, **119**: 606 (1960);
https://doi.org/10.1103/PhysRev.119.606
210. D.L. Miller, K.D. Kubista, G.M. Rutter, M. Ruan, W.A. de Heer, Ph.N. First, and J.A. Stroscio, Observing the quantization of zero mass carriers in graphene, *Science*, **324**: 924 (2009);
https://doi.org/10.1126/science.1171810
211. L.D. Landau and E.M. Lifschitz, *Quantum Mechanics: Non-Relativistic Theory* (London: Pergamon Press: 1977).
212. I.Yu. Sahalianov, T.M. Radchenko, V.A. Tatarenko, and Yu.I. Prylutskyy, Magnetic field-, strain-, and disorder-induced responses in an energy spectrum of graphene, *Ann. Phys.*, **398**: 80 (2018);
https://doi.org/10.1016/j.aop.2018.09.004
213. Y. Zhang, Z. Jiang, J.P. Small, M.S. Purewal, Y.-W. Tan, M. Fazlollahi, J.D. Chudow, J.A. Jaszczak, H.L. Stormer, and P. Kim, Landau-level splitting in graphene in high magnetic fields, *Phys. Rev. Lett.*, **96**: 136806 (2006);
https://doi.org/10.1103/PhysRevLett.96.136806
214. A.L.C. Pereira and P.A. Schulz, Additional levels between Landau bands due to vacancies in graphene: Towards defect engineering, *Phys. Rev. B*, **78**: 125402 (2008);
https://doi.org/10.1103/PhysRevB.78.125402
215. L. Schweitzer and P. Markos, Disorder-driven splitting of the conductance peak at the Dirac point in graphene, *Phys. Rev. B*, **78**, No. 20: 205419 (2008);
https://doi.org/10.1103/PhysRevB.78.205419
216. I.M. Dubrovskyi, The new theory of electron gas in a magnetic field and tasks for theory and experiment, *Usp. Fiz. Met.*, **17**, No. 1: 53 (2016);
https://doi.org/10.15407/ufm.17.01.053

Received 02.02.2022;
in final version, 29.04.2022

А.Г. Соломенко[1], Р.М. Балабай[2], Т.М. Радченко[1], В.А. Татаренко[1]
[1] Інститут металофізики ім. Г.В. Курдюмова НАН України,
бульв. Акад. Вернадського, 36, 03142 Київ, Україна
[2] Криворізький державний педагогічний університет,
просп. Гагаріна, 54, 50086 Кривий Ріг, Україна

ФУНКЦІОНАЛІЗАЦІЯ КВАЗИДВОВИМІРНИХ МАТЕРІАЛІВ: ХІМІЧНЕ ТА СПРИЧИНЕНЕ ДЕФОРМАЦІЯМИ МОДИФІКУВАННЯ

Серед сімейства наразі відомих перспективних квазидвовимірних (2*D*) матеріалів автори огляду зосереджуються на питанні функціоналізації структур на графеновій і фосфореновій основах. У більшості випадків модифікування їхніх властивостей відбувається через ковалентну або нековалентну функціоналізацію поверхонь і механічні впливи. Аналізуються атомарні структури та деякі фізико-хімічні особливості 2*D*-матеріалів, які мають новітні властивості порівняно зі своїми об'ємними аналогами. Серед їхніх переваг основними є: товщина в один або кілька атомів, відсутність обірваних поверхневих зв'язків, висока рухливість носіїв заряду, гнучкість, здатність штучного поєднання у компланарні (латеральні) чи то ламелярні гетероструктури, а також можливість широкого маніпулювання забороненою зоною, змінюючи за потреби стан від напівпровідникового аж до напівметалічного (чи навпаки). Задля виявлення нових чинників впливу на електронні та транспортні властивості 2*D*-матеріалів шляхом обчислювального експерименту з використанням авторського (власноруч створеного) програмного коду було проведено низку досліджень — розраховано просторові розподіли густини валентних електронів, густини електронних станів, ширини заборонених зон, Кулонові потенціали уздовж обраних напрямків, значення зарядів у областях різного розміру матеріалу, діелектричні матриці, макроскопічні відносні проникності та спектри поглинання. Оглядається серія нещодавніх досліджень, які автори провели, моделюючи електронні та транспортні властивості одно- та багатошарових графенових плівок, що містять різного типу (точкові та/чи то лінійні) дефекти, під впливом деформаційних або/і магнітних полів. На підґрунті аналізу одержаних результатів і виявлених ефектів стверджується, що одновісні деформації розтягу чи то зсуву та їхні комбінації, а також структурні недосконалості (головним чином, взаємно конфіґуровані дефекти) можуть бути корисними для досягнення нового рівня функціоналізації графенових матеріалів, а саме, для модифікування їхніх електротранспортних властивостей реґулюванням ширини забороненої зони в такому інтервалі, щоб уможливити перетворення графенового напівметалічного стану з нульовою забороненою зоною у графеновий напівпровідниковий стан і навіть сягнути значень енергетичної щілини, які б істотно перевищували її значення для деяких матеріалів (включаючи силіцій), що наразі широко використовуються у наноелектронних пристроях. Спричинені деформаціями та дефектами електронно-діркова асиметрія й анізотропія провідності та її немонотонність як функції деформації вселяють певність у перспективі маніпулювання електротранспортними властивостями графеноподібних та інших квази-2*D*-матеріалів через різноманіття як деформацій, так і конфіґурацій різного типу дефектів. Використання оглянутих і проаналізованих результатів слугуватиме помітним кроком у поліпшенні властивостей розглядуваних матеріалів задля реалізації багатофункціональних застосувань їх у найближчій перспективі.

Ключові слова: двовимірні матеріали, точкові та лінійні дефекти, графен, фосфорен, електронна структура, електротранспортні властивості, теорія функціоналу густини, псевдопотенціал із перших принципів, стрейнтроніка, заборонена зона.